Johannes Gutenberg–Universität

Mainz

Institut für Kernphysik

Measurement of the Helicity Dependence of Deuteron Photodisintegration for Photon Energies below 450 MeV

Dissertation
zur Erlangung des Grades
„Doktor
der Naturwissenschaften“
am Fachbereich Physik
der Johannes Gutenberg-Universität
in Mainz

Oliver Jahn

geb. in Bad Kreuznach

Mainz, den 24. Oktober 2005

Tag der mündlichen Prüfung: 12. Oktober 2005

Contents

— Abstract —

In 1998 a pilot experiment was carried out to study the helicity dependence of photoreaction cross sections using circularly polarized real photons on longitudinally polarized deuterons in a deuterated butanol target. The knowledge of these cross sections is required to test the validity of the Gerasimov-Drell-Hearn sum rule on the deuteron and the neutron. The focus of this thesis is on the results for the differential and total cross sections for the photodisintegration reaction for various photon energies in the range from 200 to 450 MeV using data taken with the detector system DAPHNE. The current understanding of the NN interaction as represented by the calculations by M. Schwamb could be confirmed within the given uncertainties. In addition, the detector DAPHNE has been prepared for the main experiment in 2003. The according work is presented together with results of the quality-test measurements of the renewed detector components.

— Zusammenfassung —

Im Jahre 1998 wurde ein Pilot-Experiment zur Untersuchung der Helizitätsabhängigkeit von Photoreaktionswirkungsquerschnitten mit zirkular polarisierten reellen Photonen an einem longitudinal polarisierten Deuterontarget mit deuteriertem Butanol als Targetmaterial durchgeführt. Die Kenntnis dieser Wirkungsquerschnitte ist notwendig um die Gültigkeit der Gerasimov-Drell-Hearn Summenregel für das Deuteron respektive das Neutron zu überprüfen. Das Hauptaugenmerk dieser Arbeit liegt bei den Resultaten für die differentiellen und totalen Wirkungsquerschnitte für die Photodesintegrationsreaktion bei verschiedenen Photonenergien im Bereich zwischen 200 und 450 MeV. Dazu wurden Daten analysiert, die mit dem Detektorsystem DAPHNE aufgenommen worden waren. Innerhalb der experimentellen Unsicherheiten konnte das zur Zeit bestehende Verständnis der NN-Wechselwirkung wie es durch Rechnungen von M. Schwamb repräsentiert wird bestätigt werden. Zusätzlich wurde der Detektor auf die Messungen für das Hauptexperiment im Jahre 2003 vorbereitet. Die dazu notwendigen Arbeiten werden zusammen mit den Ergebnissen der Qualitätstests der erneuerten Komponenten vorgestellt.

Chapter 1

Introduction and Physics Background

IT HAS been one of the fundamental aims of this work to gain doubly polarized photodisintegration cross section information from the deuteron. Since the deuteron is the simplest possible composite nucleus, it provides an ideal testing ground for theoretical models and therefore for our present understanding of nuclear dynamics. As will be explained in the following, this information is of special interest for the experimental test of the Gerasimov-Drell-Hearn (GDH) sum rule which relates the anomalous magnetic moment of a particle, κ, to an energy-weighted integral—denoted by I^{GDH}—over its total inclusive photo-absorption cross sections, σ_p and σ_a. For a particle of mass M, charge eQ, and spin S that is aligned parallel (p) or antiparallel (a) to the spin or helicity of the impinging circularly polarized photons of energy ν it reads

$$\frac{4\pi^2 e^2 \kappa^2}{M^2} S = \int_0^\infty \frac{\mathrm{d}\nu}{\nu} (\sigma_p(\nu) - \sigma_a(\nu)) \equiv I^{\mathrm{GDH}}. \tag{1.1}$$

The anomalous magnetic moment is defined by the total magnetic moment operator of the particle $\vec{\mathcal{M}} = (Q + \kappa)\frac{e}{M}\vec{\mathcal{S}}$ with $\vec{\mathcal{S}}$ denoting the spin operator of the particle. This sum rule has first been derived for the proton by Gerasimov [Gerasimov66], and by Drell and Hearn [Drell66] shortly after, as well as by Hosada and Yamamoto [Hosada66], and has later been generalized to particles of arbitrary spin [Friar77, Saito69]. Hosada and Yamamoto used current algebra relations while the others based the derivation on two ingredients which follow from the general principles of Lorentz and gauge invariance, unitarity, crossing symmetry and causality of the Compton scattering amplitude for a particle. These ingredients are 1) the low energy theorem for the Compton scattering amplitude and 2) the assumption of an unsubtracted dispersion relation for the difference of the elastic forward scattering amplitudes for circularly polarized photons and a completely polarized target with spin parallel and antiparallel to the photon spin. While the first ingredient is quite general and has a very solid theoretical basis, the validity of the sum rule presumably depends on the second assumption. Albeit latest experimental results [Dutz04] indicate the validity of the GDH sum rule for the proton, the situation for the neutron

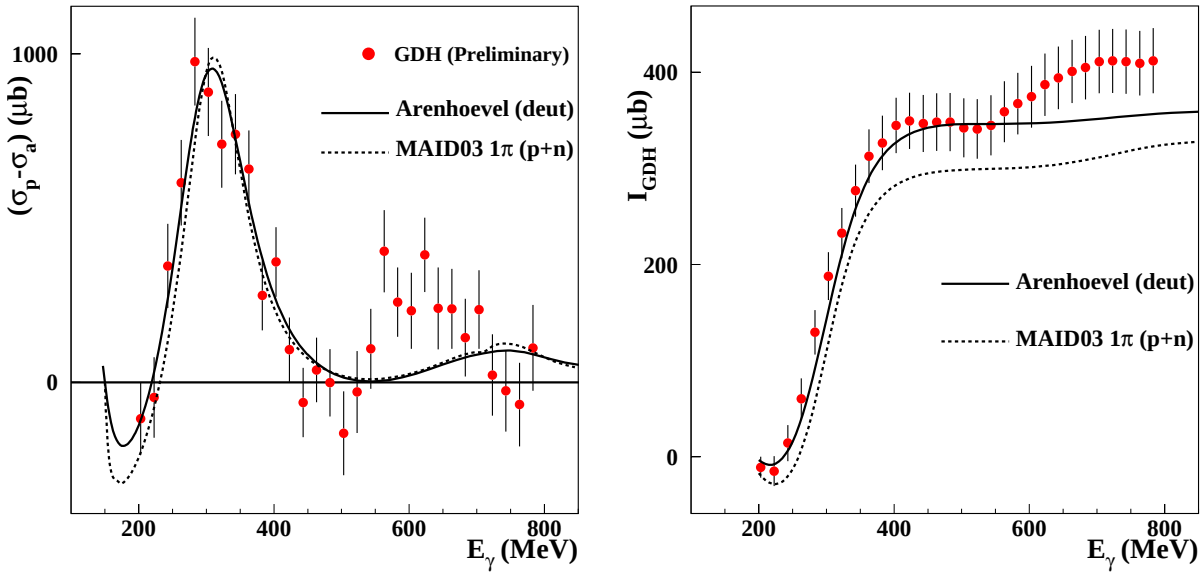

Figure 1.1. Preliminary results of the 1998 GDH measurement for the total spin asymmetry (left) and the GDH integral function (right) on the deuteron in the photon lab energy range between 200 and 800 MeV confronted with calculations using the Arenhövel model (full line) and the MAID2003 sum for free proton and free neutron (dashed line). The lower integration limit for the GDH integral function is 200 MeV for both data and theory. Figures courtesy of T. Rostomyan [Rostomyan].

is much less clear at this time. The problems arise basically from the lack of free neutron targets and from the complex nature of the nuclei that have to be used instead, e. g. the deuteron, He3, etc. Theoretical understanding of the binding effects on the nucleons in a complex nucleus has not yet thriven to a point at which it would be unquestionable whether it is possible or not to separate these effects from the free neutron properties. Beyond dispute however is the necessity of improving the current knowledge of the nuclear structure-dependent effects to this end; and the deuteron—as the simplest compound system of proton and neutron—is a very suitable object to study these effects.

When applying the GDH sum rule to proton and neutron separately, one expects values of $I_p^{\mathrm{GDH}} = 204.8\ \mu$b for the proton and of $I_n^{\mathrm{GDH}} = 233.2\ \mu$b for the neutron because of their relatively large anomalous magnetic moments. Considering the possible absorption processes one finds that the incoherent pion production on the deuteron is dominated by the quasi-free production on the nucleons bound in the deuteron [Arenhövel97]. Hence it is not too naive to expect the GDH sum rule value of the deuteron originating from these processes to be basically the sum of the contributions of the proton and of the neutron, i. e. 438 μb. This large positive value is furthermore enhanced by the—positive as well—contribution by coherent neutral pion production on the deuteron [Arenhövel97]. In fact, recent preliminary results for the total inclusive spin asymmetry show that this simple picture is not too far from the truth. Figure 1.1 (left) shows the data (solid circles) for the inclusive spin asymmetry compared to calculations by Arenhövel et al. [Arenhövel97] (full line), and calculations from MAID2003 summing contributions on the free proton and the free neutron (dashed line). None of the two models can be contradicted by

the data. The failure of both models to describe the data in the second resonance region where double pion production becomes effective is due to the one-meson approximation that is used in both cases. Only when studying the GDH integral function

$$I^{\mathrm{GDH}}(E_\gamma) = \int_{200\ \mathrm{MeV}}^{E_\gamma} \frac{\sigma_\mathrm{p}(\nu) - \sigma_\mathrm{a}(\nu)}{\nu} \mathrm{d}\nu, \tag{1.2}$$

as depicted in Figure 1.1 (right), it becomes clearly visible that the sum of the two free nucleons is too crude an ansatz. But even in this case the rough MAID estimation is not too far off the data until 300 MeV photon energy, while the Arenhövel model is able to follow the data until the onset of the second resonance region. The Arenhövel model has been improved recently [Arenhövel04] extending its ability to describe the data far into the second resonance region. Since the resulting changes do not affect this discussion, the according calculations are not presented here.

On the other hand side, the GDH sum rule for the deuteron demands a very small value of $I_d^{\mathrm{GDH}} = 0.65\ \mu$b due to the small anomalous magnetic moment of the deuteron of $\kappa_d = -0.143$. The only possible channel to provide the necessary negative contribution is the photodisintegration reaction, especially at photon energies close to threshold. This negative contribution comes from the M1-transition to the resonant $^1S_0$ state, which can only be accessed when the spins of the photon and the deuteron are antiparallel and which is forbidden otherwise. Already from these very basic estimates it is clear that a very delicate cancelation of relatively large contributions is crucial to derive the GDH integral from microscopic models.

Before discussing any model, the basics of the formal theory for two-particle channels shall be recalled [Arenhövel91]. In this context it is sufficient to only consider two-nucleon final states and to neglect pion production at all energies. After will follow a short discussion of the Arenhövel model as described in [Schwamb99] with special focus on deuteron photodisintegration.

1.1 T-Matrix Formalism for Deuteron Photodisintegration

As mentioned before, this section will give a short reminder of the formal aspects of the theoretical approach. It follows the according chapter in [Arenhövel91] and can be found there in greater detail.

The initial state is given by the four-momenta of the incoming photon and the deuteron, p_γ and p_d, together with the density matrices for the polarization of the respective particle, ϱ^γ and ϱ^d. Analogously, the four-momenta and density matrices for the final state are p_p, ϱ^p and p_n, ϱ^n, cf. Figure 1.2, for the free proton and neutron respectively.

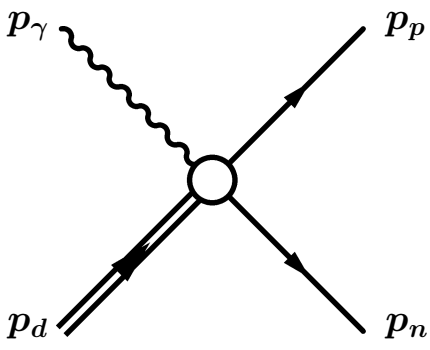

Figure 1.2. Diagram for deuteron photodisintegration with the definition of momenta.

The reference frame of preference will be the center-of-mass (cm) frame. All quantities without other specification will refer to the cm frame. For the definition of the variables and the kinematical relations between laboratory and cm frame please refer to Appendix A.

In general, the expression for the differential cross section of a two-body reaction like

$$p_1^i + p_2^i \longrightarrow p_1^f + p_2^f$$

reads

$$\mathrm{d}\sigma = \frac{(2\pi)^{10}}{4p_{10}^i p_{20}^i v_{12}} \sum\!\!\!\!\!\!\int_f \frac{\mathrm{d}^3 p_1^f}{2p_{10}^f} \frac{\mathrm{d}^3 p_2^f}{2p_{20}^f}\, \delta^{(4)}(P_f - P_i)\, |T_{fi}|^2\,, \tag{1.3}$$

with v_{12} the relative velocity in the incoming channel. The T-matrix and the scattering matrix S are related as follows:

$$S_{fi} = \langle\, f \mid\, i \,\rangle + i(2\pi)^4\, \delta^{(4)}(P_f - P_i)\, T_{fi}. \tag{1.4}$$

Focusing on deuteron photodisintegration and choosing the cm frame, Equation 1.3 becomes

$$\frac{\mathrm{d}\sigma}{\mathrm{d}\Omega} = \frac{(2\pi)^{10}}{(4W)^2}\, \frac{k}{\omega}\, |T_{fi}|^2 =: |T_{fi}^\gamma|^2. \tag{1.5}$$

In first-order perturbation theory, the T-matrix is given by

$$T_{fi}^\gamma = \frac{(2\pi)^4}{4W} \sqrt{\frac{2\alpha k}{\omega}}\; \langle\, p_f, W \mid\, J_\lambda(0)\, \mid p_d \,\rangle\,, \tag{1.6}$$

with

$$J_\lambda(0) = \varepsilon^\mu(\lambda) J_\mu(0), \tag{1.7}$$

where $J_\mu(0)$ is the current density operator, $\varepsilon^\mu(\lambda)$ the photon polarization vector, and $\alpha = e^2/4\pi$ the fine structure constant. p_f is the asymptotic relative momentum of the final state as defined by Equation A.10 on page 96, and $p_d = (E_d, -\vec{\omega})$ is the total initial deuteron momentum.

Taking into account the spin orientation of the deuteron and the nucleons in the final state as well as the photon polarization, one chooses an arbitrary quantization axis. A quite convenient axis for considering the initial deuteron orientation would be the direction of the incoming photon momentum $\vec{\omega}$. The spin projection of the initial deuteron state onto this quantization axis is then denoted by m_d. The natural quantization axis for the final state is the relative momentum $\vec{k}$, with the projection m_s of its total spin $s \in \{0, 1\}$. This situation is shown in Figure 1.3. The differential cross section for photodisintegration for arbitrary photon and deuteron polarization is then given by

$$\begin{aligned} \frac{\mathrm{d}\sigma^\gamma(\varrho_i)}{\mathrm{d}\Omega} &= \mathrm{Tr}\left(T^\gamma \varrho_i T^{\gamma\dagger}\right) \\ &= \sum_{s m_s \lambda \lambda' m_d m_d'} T^\gamma_{s m_s \lambda m_d} \varrho^\gamma_{\lambda\lambda'} \varrho^d_{m_d m_d'} T^{\gamma^*}_{s m_s \lambda' m_d'}. \end{aligned} \tag{1.8}$$

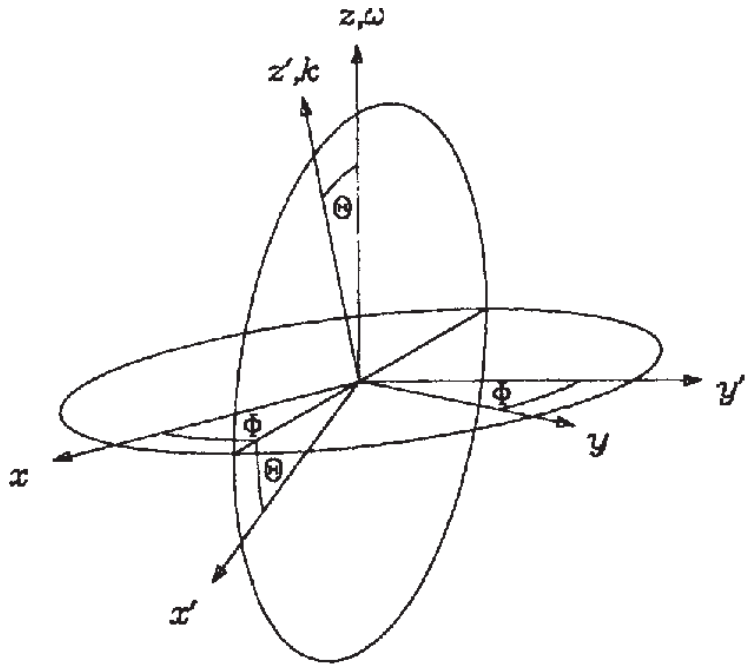

Figure 1.3. Definition of reference frames for deuteron photodisintegration in the cm system. The incoming photon momentum ω is along the z-axis and the relative p-n momentum $\vec{k}$ along the z'-axis. The transformation between the two coordinate systems is characterized by the rotation angles Θ and Φ.

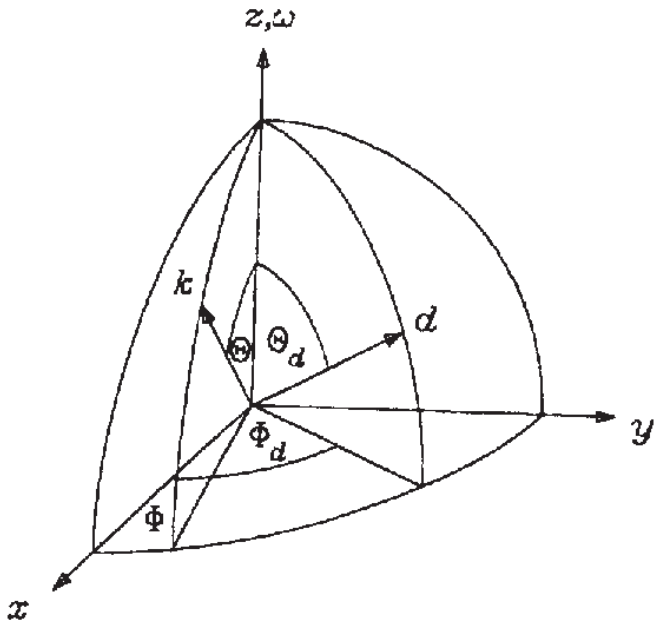

Figure 1.4. Definition of the deuteron orientation axis d as characterized by the angles of Θ_d and Φ_d. Θ and Φ are given as shown in Figure 1.3.

The polarization information is described by the density matrices for the photon ϱ^γ and the deuteron ϱ^d

$$\varrho^\gamma = \frac{1}{2}(1 + \vec{P}^\gamma \cdot \vec{\sigma}), \tag{1.9}$$

where $|\vec{P}^\gamma|$ is the total degree of photon polarization. $P_c^\gamma = P_z^\gamma$ is the difference of right to left circularly polarized photons, i. e. $|P_c^\gamma|$ gives the degree of circular polarization according to the sign of P_c^γ ($P_c^\gamma > 0$: right circular polarization, $P_c^\gamma < 0$: left circular polarization). The degree of linear polarization is given by $P_l^\gamma = \sqrt{(P_x^\gamma)^2 + (P_y^\gamma)^2}$. By choosing a suitable rotation it is always possible to have $P_y^\gamma = 0$.

Since the deuteron has spin one, the according density matrix

$$\varrho^d = \frac{1}{3}\sum_{I=0}^{2}\sum_{M}(-)^M \Omega^{[I]}_{-M} P^d_{IM} \tag{1.10}$$

can be decomposed into scalar, vector, and tensor operators $\Omega^{[I]}_M$ with $I = 0, 1, 2$ and with the corresponding orientation parameters P^d_{IM}. The operators are defined to have the following reduced matrix elements

$$\langle 1 \parallel \Omega^{[I]} \parallel 1\rangle = \sqrt{3}\,\hat{I}, \qquad \hat{I} = \sqrt{2I+1}. \tag{1.11}$$

With this and using the 3j-symbol as given by [Edmonds68] one has

$$\varrho^d_{m'm} = \langle 1m'|\varrho^d|1m\rangle = \frac{1}{\sqrt{3}}\sum_{IM}(-)^{1-m}\hat{I}\begin{pmatrix} 1 & 1 & I \\ m & -m' & -M \end{pmatrix} P^d_{IM}, \tag{1.12}$$

with $P^d_{00} = 1$. For the polarized deuteron targets that are available at this time the density matrix is diagonal with respect to a certain orientation axis $\hat{d}$ characterized by the angles Θ_d and Φ_d as shown in Figure 1.4. Hence

$$\varrho^d_{m'm} = p_m \delta_{m'm}, \tag{1.13}$$

with p_m the probability of finding a deuteron with spin projection m on axis $\hat{d}$. The only non-vanishing orientation parameters in this case are

$$P^d_1 \equiv P^d_{10} = \sqrt{\frac{3}{2}}\,(p_1 - p_{-1}), \tag{1.14}$$

$$P^d_2 \equiv P^d_{20} = \frac{1}{\sqrt{2}}\,(p_1 + p_{-1} - 2p_0) = \frac{1}{\sqrt{2}}(1 - 3p_0). \tag{1.15}$$

The last step in Equation 1.15 is valid because $p_1 + p_{-1} + p_0 = 1$, i. e. the total probability is normalized to unity.

Separating the photon and deuteron polarization parameters, Equation 1.8 can be denoted

$$\frac{\mathrm{d}\sigma^\gamma(\varrho_i)}{\mathrm{d}\Omega} = \frac{1}{2}\sum_{\lambda,IM}\left(A^\gamma_{\lambda\lambda IM}(1) - P_l^\gamma A^\gamma_{\lambda-\lambda IM}(1) + P_c^\gamma \lambda A^\gamma_{\lambda\lambda IM}(1)\right) P^{d*}_{IM}, \tag{1.16}$$

where for the photon density matrix the coordinate system has been chosen in which $P_y^\gamma = 0$ and P_x^γ has been set equal to $-P_l^\gamma$. For an arbitrary spin operator $\hat{\Omega}$ one has set

$$A^\gamma_{\lambda\lambda' IM}(\hat{\Omega}) = \frac{\hat{I}}{\sqrt{3}} \sum_{sm_s s' m'_s m_d m'_d} (-)^{1-m'_d} \begin{pmatrix} 1 & 1 & I \\ m'_d & -m_d & M \end{pmatrix} T^\gamma_{sm_s\lambda m_d} T^{\gamma^*}_{s'm'_s\lambda' m'_d} \langle s' m'_s \,|\, \hat{\Omega} \,|\, s m_s \rangle. \tag{1.17}$$

The aim of microscopic models is to determine the T-matrix element in Equation 1.16 by constructing realistic potentials and currents, and—if necessary—introduce reasonable approximations. One example of this is the model by Arenhövel which will be briefly described in the following section.

1.2 Model by Arenhövel et al.

To proceed farther in the calculation of the (differential) cross section, the T-matrix elements that contain all relevant information about the dynamical properties of the system need to be evaluated. The starting point would be the modeling of a potential and current that describe the N-N interaction in a realistic manner. There exists a variety of potentials which are surveyed in [Arenhövel91] using many kinds of approximations. Most of these make heavy use of the static limit for the meson propagator for the hadronic interaction and the electromagnetic two-body exchange current, i. e. the nucleon mass in the propagator is assumed infinite and thus the energy transfer in the meson exchange process is neglected. They all have in common that they are not able to describe the whole set of experimental data on differential cross sections and polarization observables for the complete Δ-resonance energy region. A recently developed model by Arenhövel and Schwamb was found to be quite successful in describing the hadronic interaction of two nucleons for electromagnetic and hadronic reactions, including deuteron photodisintegration, c. f. Chapter 5. It is applicable for excitation energies up to 500 MeV and reactions in which at most one pion is created or absorbed. Adapted from a model that had been developed by Sauer and collaborators (see the Refs. 23, 25, 26 in [Schwamb01] b), this model allows to explicitly study retardation in the two-body meson-exchange operators using an NN-$N\Delta$ coupled-channel approach and time-ordered perturbation theory. In retarded calculations the interaction's finite velocity of propagation is taken into account using an explicitly energy-dependent propagator. The problem of non-hermiticity of retarded interactions has been overcome by generating retarded one-boson-exchange mechanisms through the explicit consideration of meson-nucleon and $\pi N\Delta$ vertices. This requires the inclusion of additional mesonic degrees of freedom in the considered Hilbert space besides the baryons. In order to satisfy two- and three-body unitarity, the πd channel and intermediate pion-nucleon loops have been incorporated as well. Inconsistencies with respect to the latter mechanism have been avoided by distinguishing bare and physical nucleons. The realistic retarded potential model of Elster et al. [Elster88] has been used as input for the basic nucleon-nucleon interaction in pure nucleonic space. The free parameters in the model have been fixed by fitting πN scattering in the P_{33} channel and NN scattering in the ${}^1D_2$ channel.

The model's Hilbert space is made up of three orthogonal sub-spaces that correspond to the three different configurations with either n bare nucleons, $\mathcal{H}^{[n]}_{\bar{N}}$, or $n-1$ nucleons plus one Δ,

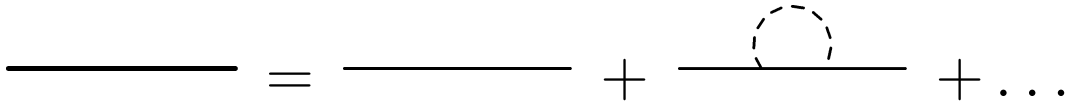

Figure 1.5. The "physical" nucleon as "bare" nucleon plus meson loop dressing.

$\mathcal{H}^{[n]}_{\Delta}$, or n nucleons plus one meson, $\mathcal{H}^{[n]}_{X}$, yielding

$$\mathcal{H}^{[n]} = \mathcal{H}^{[n]}_{\bar{N}} \oplus \mathcal{H}^{[n]}_{\Delta} \oplus \mathcal{H}^{[n]}_{X}. \tag{1.18}$$

$\bar{N}$ denotes a bare nucleon, i. e. a nucleon without the according meson cloud of the corresponding physical nucleon. The "physicality" of the real nucleon is achieved by dressing the bare nucleon with meson-nucleon loops, c. f. Figure 1.5. Since at most one-meson states are taken into account and the focus on the deuteron limits the number of nucleons to $n = 2$, the corresponding Hilbert space can be written as

$$\mathcal{H}^{[2]}_{X} = \bigoplus_{x\in\{\pi,\eta,\sigma,\delta,\omega,\rho\}} \mathcal{H}^{[2]}_{x}, \tag{1.19}$$

with π, η, σ, δ, ω, ρ the mesons considered in the model. With the projection operators

$$P_{\bar{N}}\mathcal{H}^{[2]} = \mathcal{H}^{[2]}_{\bar{N}}, \qquad P_{\Delta}\mathcal{H}^{[2]} = \mathcal{H}^{[2]}_{\Delta},$$
$$P_{X}\mathcal{H}^{[2]} = \mathcal{H}^{[2]}_{X}, \quad \text{and} \quad P = P_{\bar{N}} + P_{\Delta},$$

where P_X is the sum of six orthogonal projectors for each meson type

$$P_X = \sum_{x\in\{\pi,\eta,\sigma,\delta,\omega,\rho\}} P_x, \quad \text{with} \quad P_x\mathcal{H}^{[2]} = \mathcal{H}^{[2]}_{x} \quad \text{for } x \in \{\pi,\eta,\sigma,\delta,\omega,\rho\},$$

any operator acting in $\mathcal{H}^{[2]}$, and in particular the electromagnetic current density operator, $J^{\mu}(\vec{\omega})$, can be written as a symbolic 3×3 matrix

$$J^{\mu}(\vec{\omega}) = \begin{pmatrix} J^{\mu}_{\bar{N}\bar{N}}(\vec{\omega}) & J^{\mu}_{\bar{N}\Delta}(\vec{\omega}) & J^{\mu}_{\bar{N}X}(\vec{\omega}) \\ J^{\mu}_{\Delta\bar{N}}(\vec{\omega}) & J^{\mu}_{\Delta\Delta}(\vec{\omega}) & J^{\mu}_{\Delta X}(\vec{\omega}) \\ J^{\mu}_{X\bar{N}}(\vec{\omega}) & J^{\mu}_{X\Delta}(\vec{\omega}) & J^{\mu}_{XX}(\vec{\omega}) \end{pmatrix} \tag{1.20}$$

using the notation

$$J^{\mu}_{\alpha\beta}(\vec{\omega}) = P_{\alpha}J^{\mu}(\vec{\omega})P_{\beta}, \qquad \alpha,\beta \in \{\bar{N},\Delta,X\}. \tag{1.21}$$

For technical reasons it is useful to distinguish between purely baryonic currents and meson production/annihilation currents. The former are separated into one and two-particle contributions, so one gets

$$J^{\lambda}_{BB'} = \sum_{i,j=1,2}\sum_{i\neq j} j^{[1]\lambda}_{BB'}(i)\delta(j) + J^{[2]\lambda}_{BB'}, \qquad \text{with } B,\ B' \in \{\bar{N},\Delta\}. \tag{1.22}$$

The according diagrams are shown in Figure 1.6.

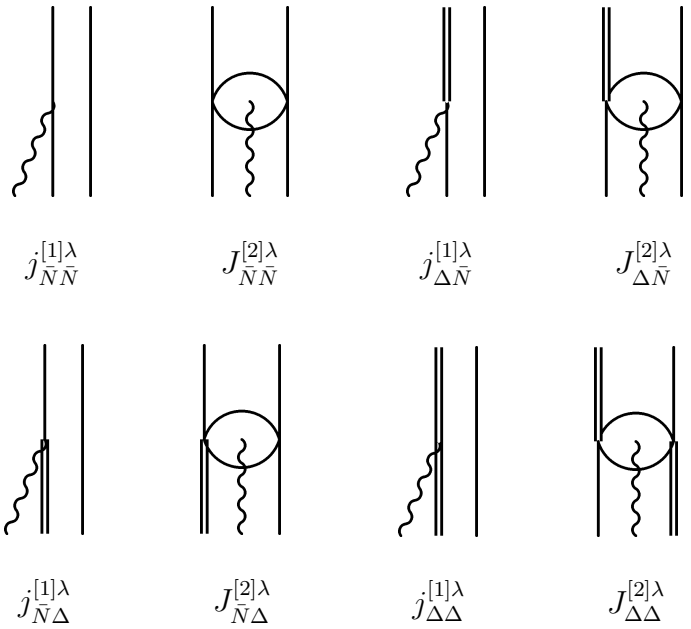

Figure 1.6. Diagrammatic representation of the baryonic currents. An open ellipse symbolizes a two-body exchange current.

The meson production/annihilation currents consist of the contributions $J^{\lambda}_{\bar{N}X}$ and $J^{\lambda}_{X\bar{N}}$ respectively whose one-particle fractions are accounted for only:

$$J^{\lambda}_{\bar{N}X} = \underbrace{j^{(0)\lambda}_{\bar{N}X}}_{A} + \sum_{i=1,2} \underbrace{j^{(1)\lambda}_{\bar{N}X}(i)}_{B} + \underbrace{j^{(1v)\lambda}_{\bar{N}X}(i)}_{C}. \tag{1.23}$$

These are presented in Figure 1.7. The terms $J^{\lambda}_{X\Delta}$ and $J^{\lambda}_{\Delta X}$ which also contribute have been neglected since they are already included approximatively in the static limit. The superscripts "(0)", "(1)", and "$(1v)$" denote the order in the meson-nucleon coupling constant; v stands for "vertex current". Term A in Equation 1.23 describes virtual annihilation of two mesons by the photon, Term B the contact interaction, and Term C an additional vertex current for non-pointlike baryons. More details on the evaluation of the individual current contributions can be found in [Schwamb99], Section 5.3 ff. Concerning deuteron photodisintegration it is of some importance to point out that the relativistic spin-orbit contribution cannot be neglected. Having fixed the individual contributions to the current operator, it is possible to construct the effective current operator for deuteron photodisintegration in two-nucleon space. It is defined by the following equation

$$\big\langle f \big| P J^{\lambda}_{\text{eff}}(z,\vec{\omega}) P \big| i \big\rangle := \big\langle f \big| J^{\lambda}(\vec{\omega}) \big| i \big\rangle, \qquad \text{with } z = W + i\varepsilon. \tag{1.24}$$

Explicitly, one ends up with

$$J^{\lambda}_{\text{eff}}(z,\vec{\omega}) = \underbrace{J^{N[1]\lambda}_{\text{eff}}(z,\vec{\omega}) + J^{N[2]\lambda}_{\text{eff}}(z,\vec{\omega})}_{\text{nucleonic part}} + \underbrace{J^{\Delta[1]\lambda}_{\text{eff}}(z,\vec{\omega}) + J^{\Delta[2]\lambda}_{\text{eff}}(z,\vec{\omega})}_{\text{resonant part}}, \tag{1.25}$$

i. e. with the sum of a nucleonic and a resonant part which themselves consist of one and two-body contributions. Note that $|i\rangle$, $|f\rangle$ have components in both $\mathcal{H}_{\bar{N}}$ and $\mathcal{H}_X$. The diagrammatic

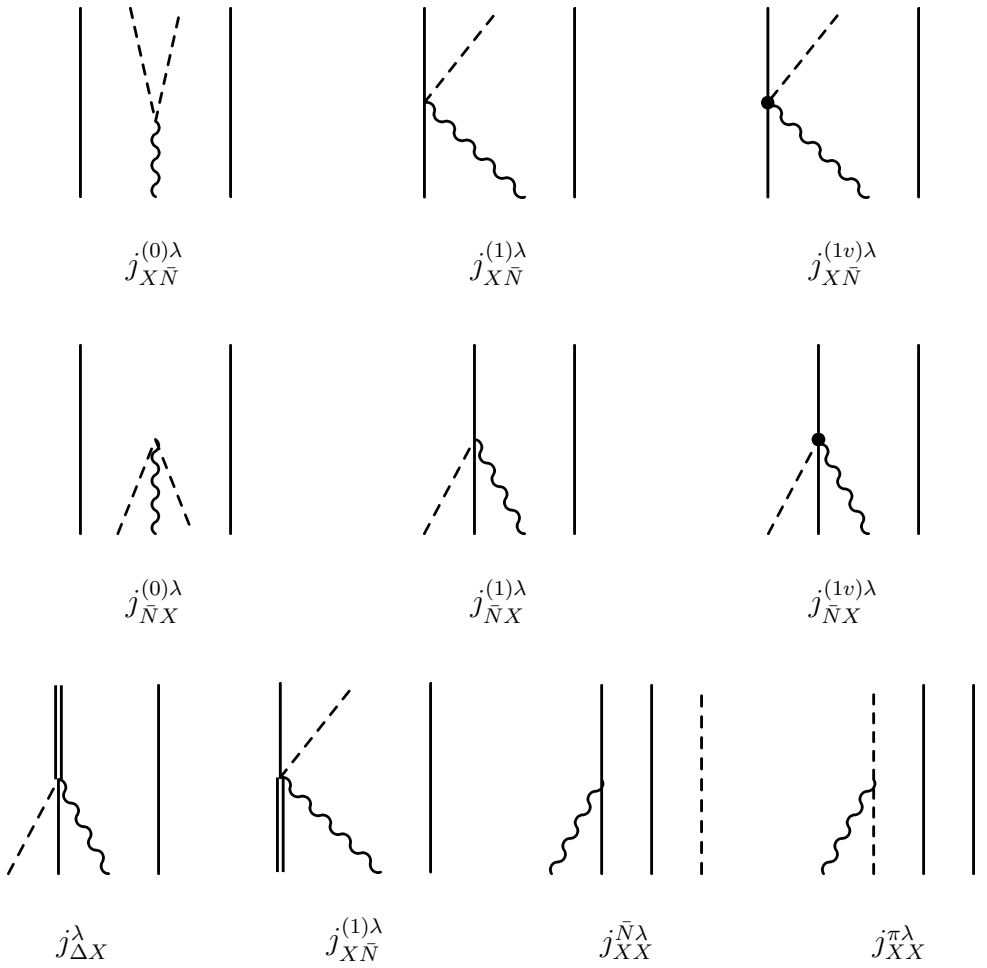

Figure 1.7. Diagrammatic representation of the meson production/annihilation currents $J^{\lambda}_{X\bar{N}}$ and $J^{\lambda}_{\bar{N}X}$ respectively as well as the diagonal current component J^{λ}_{XX}.

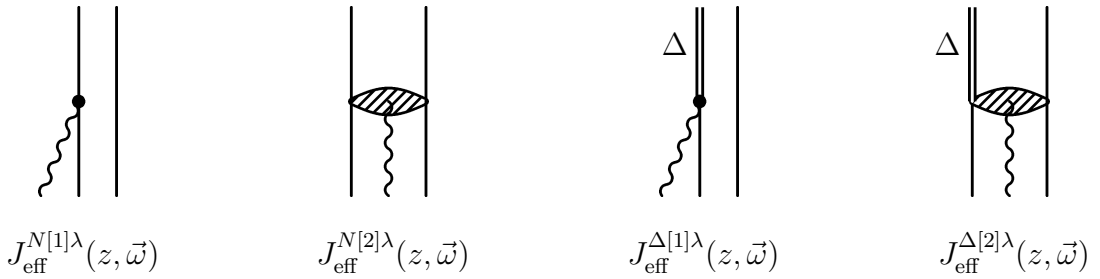

Figure 1.8. Diagrammatic representation of the contributions for the effective current operator $J^{\lambda}_{\text{eff}}(z,\vec{\omega})$ as given in Equation 1.25. The effective two-body part is represented by a hatched ellipse.

representation is given in Figure 1.8. With this one is ready to determine the T-matrix element in Equation 1.16 which is related to the effective current operator as follows

$$\delta(\vec{k}+\vec{n}_0-\vec{\omega}-\vec{d}\,)T_{sm_s\lambda m_d}(\omega_{\rm lab},\Theta,\Phi) = -\vec{\varepsilon}\big(\vec{\omega},\lambda\big)\cdot\big\langle pn(\vec{k}sm_s)^{(-)}\big|P\vec{J}_{\rm eff}(z,\vec{\omega})P\big|d(\vec{\omega}m_d)\big\rangle. \tag{1.26}$$

Θ and Φ are the spherical coordinates of the outgoing proton. As an example, one would get for the total unpolarized differential cross section

$$\frac{\mathrm{d}\sigma}{\mathrm{d}\Omega}(\Theta,\Phi) = \frac{1}{6}C'\sum_{sm_s\lambda m_d}|T_{sm_s\lambda m_d}(\omega_{\rm lab},\Theta,\Phi)|^2, \tag{1.27}$$

where C' is a kinematical constant.

1.3 Outline

The experimental setup for the 1998 GDH experiment that delivered the data which are analyzed in this thesis will be discussed in Chapter 2, followed by the presentation of the work that was done to improve and renew the DAPHNE detector for the 2003 nGDH experiment in Chapter 3. A description of the analysis procedure of the 1998 data is given in Chapter 4. The calculations from the model described before for the polarized cross sections for deuteron photodisintegration will be confronted with the data for deuteron photodisintegration from the 1998 GDH measurement in Chapter 5. A summary and an outlook will conclude the thesis.

Chapter 2

Experimental Setup

THIS thesis is based on the GDH experiment that was carried out in 1998 within the framework of the A2 Collaboration at the Institut für Kernphysik, Johannes Gutenberg-Universität, Mainz, making use of the 855 MeV electron accelerator facility Mainz Microtron (MAMI). Its polarized electron beam is converted in the real photon facility (tagger) into a beam of circularly polarized real photons by the bremsstrahlung process on a thin radiator. This photon beam irradiates a target of polarized deuterated butanol whose emerging reaction products are detected by DAPHNE, an acronym for *Détecteur à grande Acceptance pour la PHysique photo Nucléaire Expérimentale*—large acceptance detector for experimental photonuclear physics. Further detector components were added to improve the solid angular coverage of the setup, especially in the forward direction. The complete set of devices will be described in more detail in the following sections.

2.1 Electron Accelerator Mainz Microtron (MAMI)

The Mainz Microtron is the heart of the experimental facility at the Institut für Kernphysik in Mainz. It provides a continuous wave electron beam at 100 percent duty cycle by means of a 3.5 MeV linear accelerator (LINAC) which serves as an injector to the three cascaded race track microtrons (RTM 1–3). The floor plan of the accelerator facility is depicted in Figure 2.1, also showing the various experimental halls to which the electron beam can be directed (A1, A2, A4, X1). The LINAC is either fed with electrons from a 100 keV unpolarized thermionic source or with electrons originating from a strained layer $GaAs_{0.95}P_{0.5}$-crystal photo-cathode which is irradiated by circularly polarized 830 nm laser light from a Titanium-Sapphire laser. The circular polarization is provided by a Pockel cell. Via the photo-electric effect linearly polarized electrons are emitted from the crystal. With this material it is possible to obtain polarization degrees between 70 and 80 percent. Maximum electron currents are 100 μA with

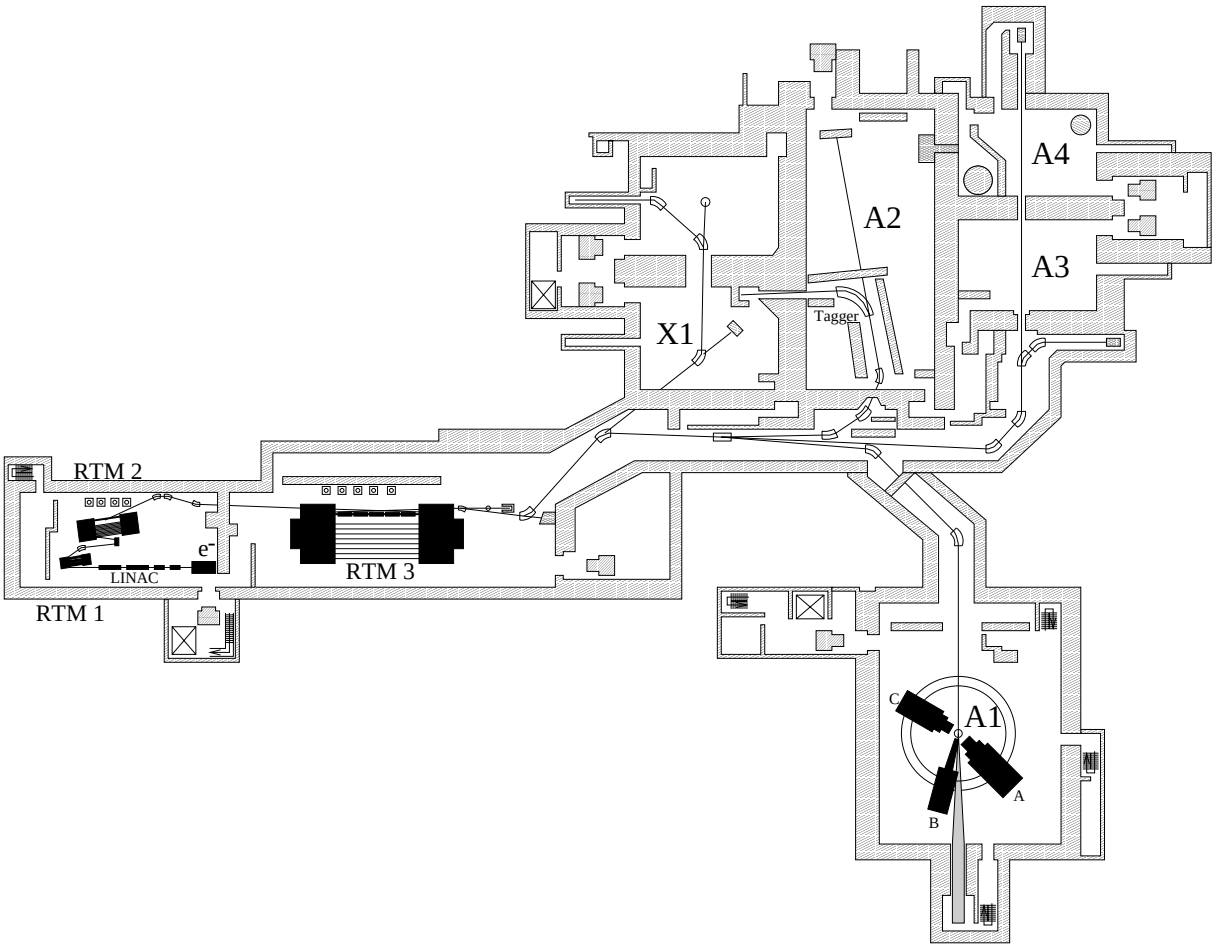

Figure 2.1. Floor plan of the Mainz Microtron electron accelerator facility and the experimental halls A1,A2, A4 and X1.

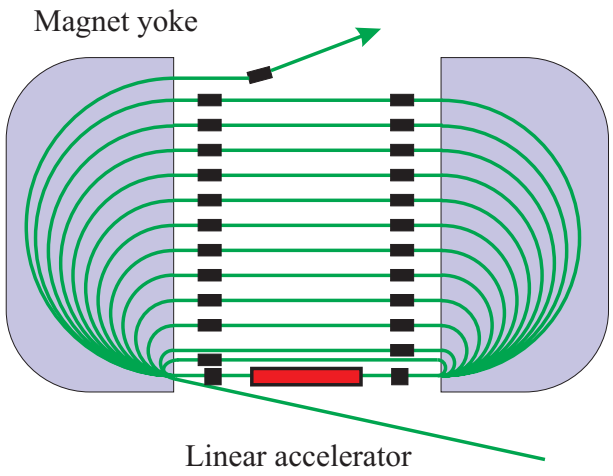

Figure 2.2. Race track microtron, schematic.

the unpolarized source and 30 μA using the polarized source. The slow initial electrons are then accelerated to 3.5 MeV kinetic energy by the LINAC and injected into the RTMs. Each of the RTMs consists of a LINAC section and two dipole magnets which deflect the electron paths by 180 degrees at each side of the RTM and redirect them into the LINAC section after each turn (Figure 2.2). Due to the homogeneous magnetic field of each dipole magnet, the electron trajectories follow semi-circles whose radii depend on the electron momenta. These radii increase by discrete amounts after each recirculation leading to a race-track-like beam path. RTM 1 increases the beam energy from 3.5 MeV to 14.4 MeV in 18 turns, RTM 2 provides a beam energy of 180 MeV in 51 turns, and RTM 3 boosts the energy to 855 MeV in 90 recirculations. Intermediate energies $E_n = (180 + 2n \cdot 7.5)$ MeV with $n \in \{1, \ldots, 45\}$ can be accessed by choosing a lower number of recirculations in RTM 3. After having left RTM 3, the beam is guided to the respective experiment hall.

2.2 Tagged Photon Facility and Photon Beam

In the A2 hall, the electron beam created by the MAMI accelerator is converted into a beam of energy-tagged real photons by means of the tagged photon facility (Glasgow-Mainz tagger), a bremsstrahlung tagging system consisting of a wide-range momentum-dispersing electron spectrometer and a multi-element focal plane detector, [Anthony91] and [Hall96]. Besides a good energy resolution, this technique provides photon fluxes up to 10^8 s^{-1} which make it superior to the common alternatives Compton laser backscattering and in-flight annihilation of positrons, normally delivering photon fluxes in the order of 10^5 s^{-1}. Figure 2.3 shows the setup schematically. An electron of initial energy E_0 striking a thin radiator of 10^{-5} to 10^{-4} radiation lengths creates a real bremsstrahlung photon of energy E_γ. By measuring the energy E_{e^-} of the scattered electron in the focal plane detector, the energy of the radiated photon is determined by the relation

$$E_\gamma = E_0 - E_{e^-}, \tag{2.1}$$

while the recoil energy of the radiator nucleus is negligible. The photon beam is collimated and illuminates the target of the experimental setup.

The electron spectrometer itself consists of a large dipole magnet that meets the requirements of a large momentum acceptance ($p_{\max} : p_{\min} \sim 16 : 1$, momentum range covered is $0.06E_0$–$0.95E_0$ for $E_0 = 840$ MeV, hence *wide-range*) and a good intrinsic energy resolution (approximately 120 keV for most of the energy range). Since the deflection radii of the electrons depend on their momenta, the focal plane detector (in A2 slang also referred to as *tagger ladder*) is made up of an array of 353 plastic detectors to allow a sufficient granularity in the focal plane to provide a photon energy resolution of 2 MeV at $E_0 = 855$ MeV over the entire covered photon energy range. A coincidence of two adjacent detectors is required to suppress random background. With this, 352 tagger channels are defined whose positions in the focal plane determine the momentum and thus the energy of the electrons that underwent bremsstrahlung scattering. The primary beam of unscattered electrons is absorbed in the Faraday cup which serves as electron beam dump. This allows monitoring the electron beam current at all times during the experiment. The resulting photon energy spectrum, as shown in Figure 2.5, complies with the integrated-over-angle bremsstrahlung energy-differential cross section, c. f.

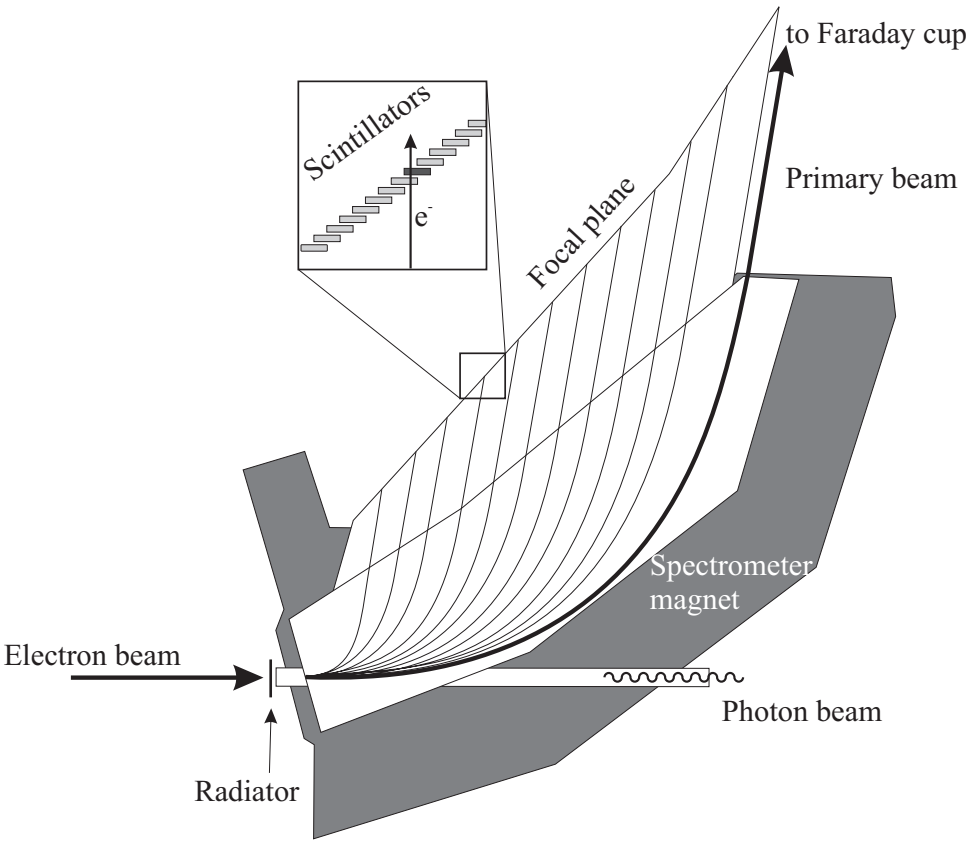

Figure 2.3. Schematic diagram of the tagged photon facility (Glasgow-Mainz tagger). The zoom shows a part of the focal plane detector array that is struck by an electron.

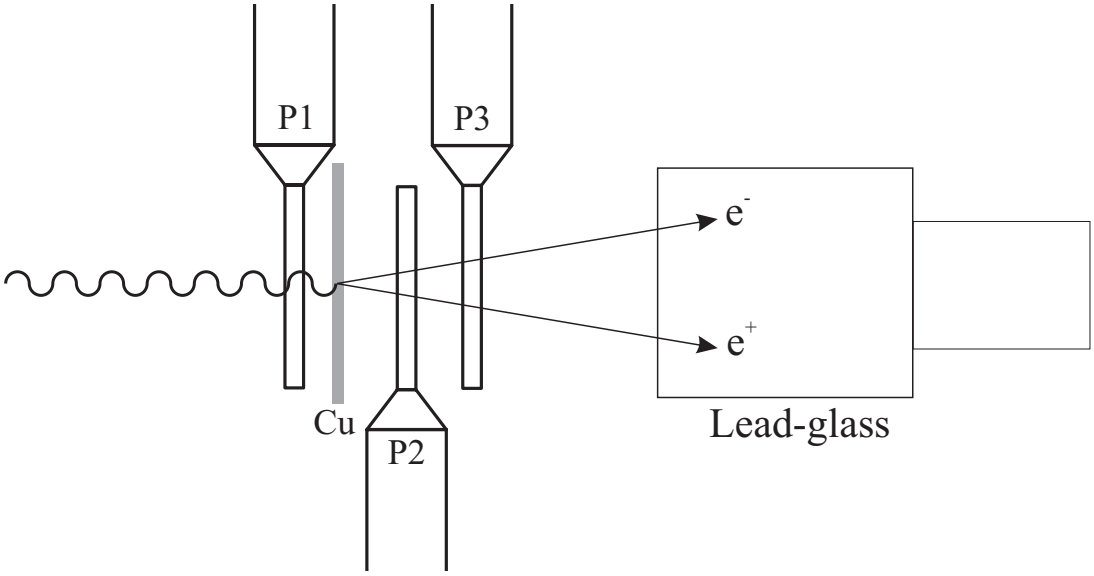

Figure 2.4. Schematic diagram of the pair and lead-glass detectors.

[Koch59] and [Matthews73],

$$\frac{\mathrm{d}\sigma}{\mathrm{d}E_\gamma} = \frac{\alpha r_0^2 Z^2}{E_\gamma}\Phi(Z, E_0, E_\gamma),$$

showing the typical $1/E_\gamma$ behavior. The fine-structure constant and the classical electron radius are $\alpha = e^2/\hbar c \approx 1/137$ and $r_0 = e^2/mc^2 = 2.82 \cdot 10^{-13}$ cm, respectively. Z is the radiator material's atomic number and $\Phi(Z, E_0, E_\gamma)$ is a correction that is discussed in detail in the above mentioned reference [Matthews73]. The channels in Figure 2.5 with a reduced number of entries compared to adjacent channels are due to defective elements of the focal plane detector. Below 200 MeV, photon energies were not tagged in this example. Only about 50 percent of the bremsstrahlung photons are emitted within the characteristic angle $\Theta_c = m_e c^2/E_0$. To obtain a well defined beam on the target cell, the photons are collimated at the tagger exit. Hence, the ratio of the number of photons reaching the target, $N_\gamma(E_\gamma)$, and the number of electrons detected in the tagger, $N_\mathrm{e}(E_\gamma)$, known as *tagging efficiency*

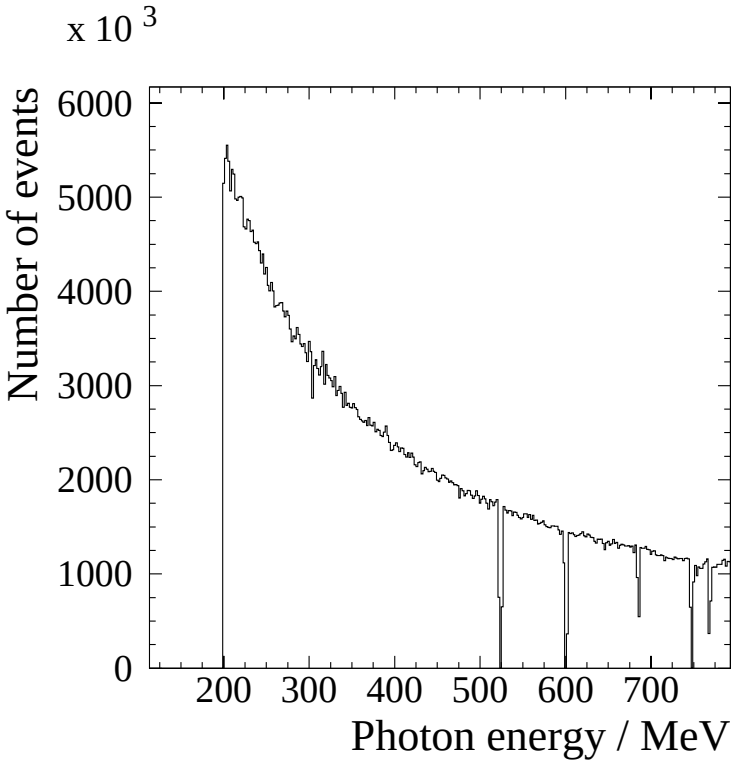

Figure 2.5. Typical bremsstrahlung energy spectrum as measured during the GDH-experiment in 1998.

$$\varepsilon_\mathrm{tagg}(E_\gamma) = \frac{N_\gamma(E_\gamma)}{N_\mathrm{e}(E_\gamma)}, \tag{2.2}$$

is always less than one. This ratio is furthermore diminished by Møller scattering in the radiator and, in general, by any background that increases the count rate in the tagger ladder but does not contribute to the photon beam (e.g. radiation backscattered from the electron beam dump, etc.) In addition, the tagging efficiency obviously not only depends strongly on the characteristic angle Θ_c and thus on the electron beam energy E_0, but also on the collimator geometry (radius, distance to the radiator) and on the position and direction of the electron beam on the radiator. The latter parameters are not constant in time, so a very careful and continuous determination of the tagging efficiency is of vital interest when obtaining accurate values for the photon fluxes needed to calculate cross section values.

Alternatively, the number of photons in the beam can be measured directly using a dedicated photon detector. In A2, a lead-glass Čerenkov detector placed at the very end of the hall, c. f. Figure 2.15 on Page 38 (labeled *Photon flux monitor*), is used for this purpose. It consists of a lead-glass cube of 25 cm edge-length in which the incident photons are converted into electron-positron pairs. These create Čerenkov light that is read out by one photomultiplier. Together with a photon detection efficiency close to 100 percent, c. f. [Jahn98], this limits the maximum

acceptable photon flux to about two orders of magnitude less than the photon fluxes needed during the GDH experiment runs. This precludes using the detector as an online monitor. Instead, an additional pair detector—with only a few percent detection efficiency—is used for this purpose while the lead-glass detector is removed from the photon beam. The pair detector, as depicted in Figure 2.4, consists of three plastic scintillators of 1 mm thickness each, labeled P1 through P3, and a copper foil between P1 and P2. P2 and P3 are operated in coincidence to detect Compton electrons and electron-positron pairs produced in the copper foil, while P1 works in anti-coincidence to prevent the detection of charged particles that were produced upstream. In dedicated runs with decreased photon flux that are carried out in regular time intervals, the lead-glass detector is placed behind the pair detector to determine both the tagging efficiency, $\varepsilon_{\mathrm{tagg}}$, and the pair detector's efficiency $\varepsilon_{\mathrm{pair}}(E_\gamma) = N_{\mathrm{pair}}(E_\gamma)/N_{\mathrm{lead-glass}}(E_\gamma)$, where N_i is the number of photons seen by the pair detector and the lead-glass detector, respectively. The energy behavior of this efficiency is fitted using the well known cross sections for electron Compton scattering and electron-positron pair production with the copper foil's thickness d_{eff} as the only free—since energy independent—parameter. With this efficiency, the number of photons

$$N_\gamma(E_\gamma) = \frac{N_{\mathrm{pair}}(E_\gamma)}{\varepsilon_{\mathrm{pair}}(E_\gamma)} \tag{2.3}$$

can be determined during normal GDH runs without the use of the lead-glass detector. The Figure 2.6 (a) shows typical tagging efficiency values versus photon energy E_γ for MAMI energies 525 and 855 MeV that were used for the GDH experiment. The lower tagging efficiency value for 525 MeV MAMI energy is due to the increase in the characteristic angle with decreasing primary energy and a hence reduced number of photons passing the collimation. Figure 2.6 (b) gives an example of the time evolution during approximately three days of beam time.

2.3 Møller Polarimetry

The circularly polarized photons for the GDH-experiment are created using the helicity transfer of longitudinally polarized electrons from MAMI in the bremsstrahlung process. For the investigation of helicity dependent cross sections, the knowledge of the photon beam polarization degree is imperative. This degree of circular polarization has been calculated by Olsen and Maximon, [Olsen59], and reads

$$P_\gamma = P_{\mathrm{e}} \frac{4\frac{E_\gamma}{E_0} - \left(\frac{E_\gamma}{E_0}\right)^2}{4 - 4\frac{E_\gamma}{E_0} + 3\left(\frac{E_\gamma}{E_0}\right)^2}. \tag{2.4}$$

The notation introduced in Section 2.2 is used. P_γ and P_{e} are the respective absolute photon and electron polarizations. The photon polarization only depends on the electron polarization once the photon energy has been determined by the tagger, while the initial electron energy is given by MAMI. Figure 2.7 shows the energy dependence of the helicity transfer for the two MAMI energy settings 525 and 855 MeV. For $E_\gamma = E_0$ the helicity transfer is maximum and decreases with energy until vanishing at zero energy.

During beam-time the orientation of the electron beam polarization is controlled by a random generator that either keeps the momentary setting or flips it in cycles of one second duration to reduce the systematic error of the measurement. The absolute value of the polarization is

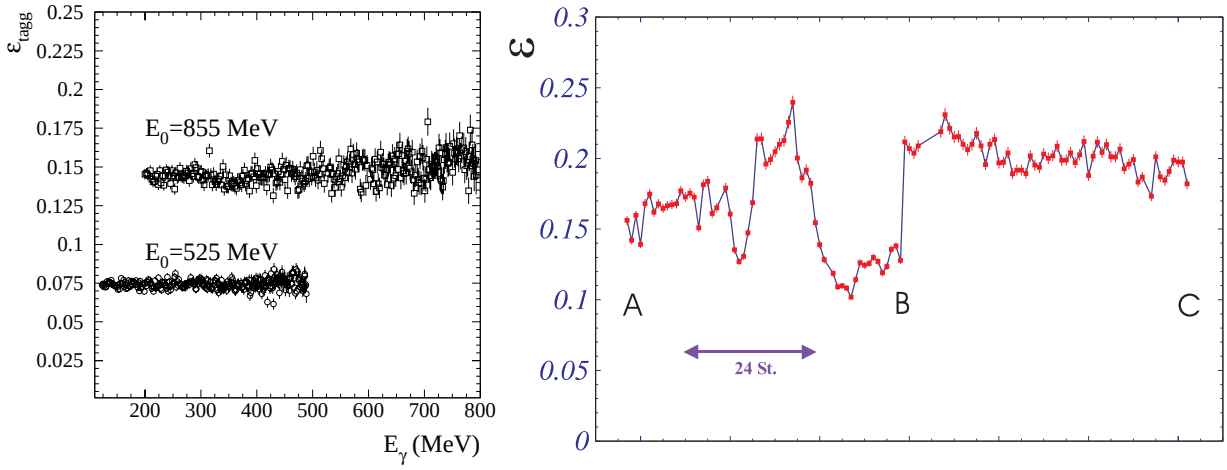

Figure 2.6. a) Energy dependence (left) and b) time evolution (right) of the tagging efficiency during GDH runs with 525 and 855 MeV MAMI energy. A period of approximately 24 hours is represented by the arrow. At time "B" the electron beam was re-adjusted by the MAMI-operator.

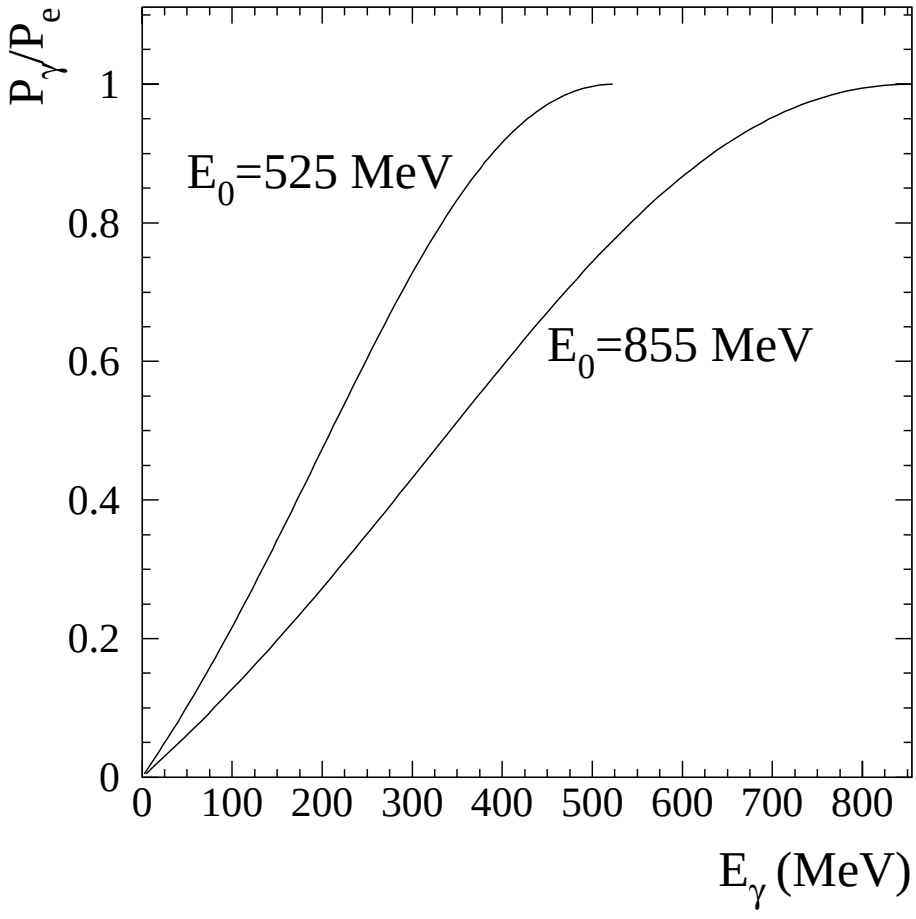

Figure 2.7. Relative polarization transfer P_γ/P_e from longitudinally polarized electrons to real photons in the bremsstrahlung process as a function of the photon energy E_γ for the two MAMI energy settings 525 and 855 MeV.

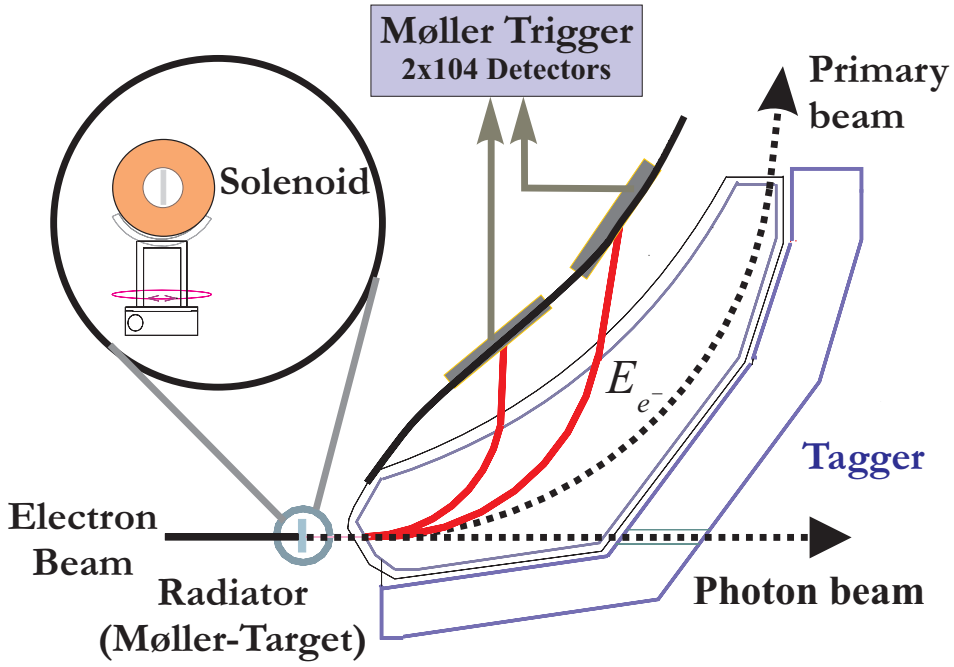

Figure 2.8. Setup of the Møller polarimeter. Pairwise coincidences of tagger channels from two blocks of 104 detectors each define the Møller trigger. The zoom shows the target foil mounted inside a rotatable solenoid. Any angle between $-25^\circ \leq \alpha \leq +25^\circ$ can be set.

measured by a Møller polarimeter, which makes use of the Møller scattering process off a magnetized ferromagnetic foil whereby an electron from MAMI interacts with a radiator electron both leaving the radiator and being detected in the tagger ladder. The energy sum of the two scattered electrons is equal to the initial energy of the incoming electron. By selecting pairs of energy channels in the tagger ladder who fulfill this condition it is possible to separate Møller events from bremsstrahlung scattering, c. f. Figure 2.8.

The derivation of the electron polarization from the count rates provided by the Møller polarimeter needs some further explanation. First of all one defines an asymmetry

$$A_{\text{Møller}} = \frac{N^{\uparrow\uparrow} - N^{\uparrow\downarrow}}{N^{\uparrow\uparrow} + N^{\uparrow\downarrow}}, \tag{2.5}$$

where $N^{\uparrow\uparrow}$ and $N^{\uparrow\downarrow}$ are the count rates for parallel and antiparallel orientation of electron and target foil polarization respectively. This asymmetry can be re-written as

$$A_{\text{Møller}} = \frac{(\mathrm{d}\sigma / \mathrm{d}E_{\mathrm{e}})^{\uparrow\uparrow} - (\mathrm{d}\sigma / \mathrm{d}E_{\mathrm{e}})^{\uparrow\downarrow}}{(\mathrm{d}\sigma / \mathrm{d}E_{\mathrm{e}})^{\uparrow\uparrow} + (\mathrm{d}\sigma / \mathrm{d}E_{\mathrm{e}})^{\uparrow\downarrow}}, \tag{2.6}$$

with the polarized Møller scattering cross section, again for parallel and antiparallel orientations

$$\left(\frac{\mathrm{d}\sigma}{\mathrm{d}E_{\mathrm{e}}}\right) = \left(\frac{\mathrm{d}\sigma}{\mathrm{d}E_{\mathrm{e}}}\right)^{\text{unpol}} \left(1 + \sum_{j,k} a_{jk} P_{\mathrm{t}}^{j} P_{\mathrm{e}}^{k}\right), \tag{2.7}$$

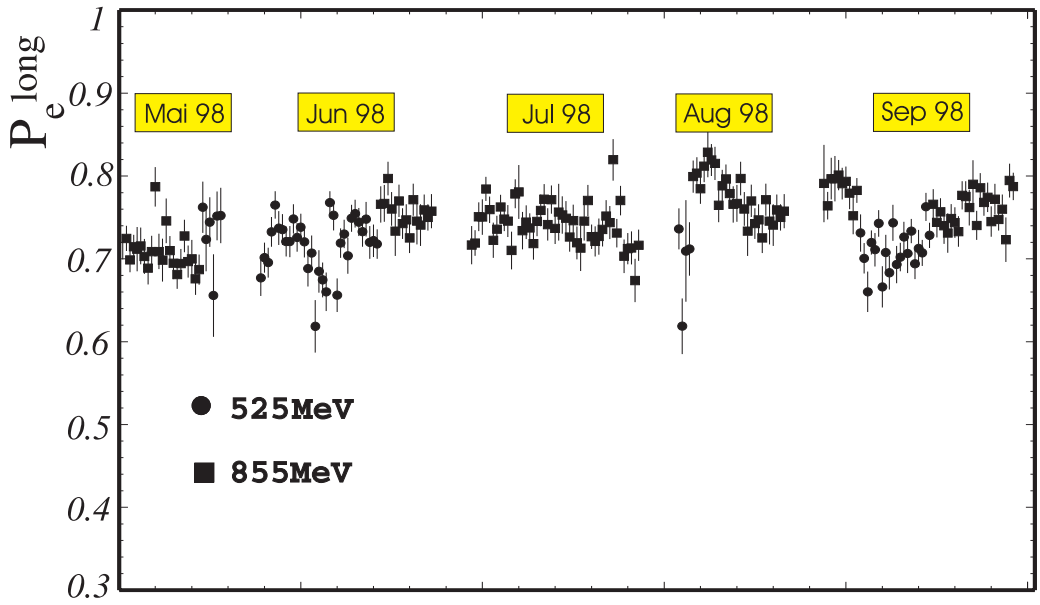

Figure 2.9. Time evolution of the photon beam polarization for run periods from May to September 1998. MAMI energies of 525 MeV are represented by filled circles, energies of 855 MeV by filled boxes.

where $\left(\frac{\mathrm{d}\sigma}{\mathrm{d}E_\mathrm{e}}\right)^{\mathrm{unpol}}$ is the unpolarized Møller cross section, P_t^j and P_e^k the Cartesian components of the target foil's and the electron beam's polarization, respectively, and a_{jk} the tensor *analyzing power* describing the polarization dependence of Møller scattering in the three spatial directions. The tensor's non-diagonal elements either vanish because of parity conservation or are negligible because of their weighting factor $(E_0 + m_e)/2m_e$. Hence, the asymmetry becomes

$$A_{\text{Møller}} = a_{zz} P_\mathrm{t} P_\mathrm{e} \cos\alpha. \tag{2.8}$$

P_t and P_e are the magnitudes of the target foil's and the electron beam's polarization vectors, respectively, α is the angle between both vectors, and $a_{zz} = -\frac{7}{9}$. The target foil polarization was measured to be $P_\mathrm{t} = (8.1 \pm 0.2)\%$. Because of experimental constraints, the angle between the two polarizations had to be non-zero and was chosen $\alpha = 25°$. This was a compromise between smallest possible angle, highest target foil polarization without using superconducting magnets, and a maximum bremsstrahlung yield. During the experiment, average electron polarizations of 75 percent were found. Four hours of beam-time were needed to obtain polarization values with a precision of two percent (Figure 2.9).

2.4 Polarized Target

The second essential ingredient in addition to circularly polarized photons is a polarized target. The polarized target setup used during the 1998 GDH experiment was provided by cooperation between the Bochum, Bonn and Nagoya groups [Bradtke99]. It is a frozen-spin target, i.e. the target material is first polarized at relatively high temperatures ($T \approx 300$ mK) and high

magnetic fields ($B \approx 2.5$ T) by dynamic nuclear polarization (DNP), then both the temperature and the magnetic field are lowered to $T \approx 50$ mK and $B \approx 500$ mT, respectively, "freezing" the high degree of polarization. The target setup consists of a horizontal cryostat to allow a maximum accessible solid angle for the detector system, a ^{3}He/^{4}He dilution refrigerator to reach temperatures as low as some 50 mK, a high homogeneity superconducting magnet providing magnetic fields up to 6.5 T during polarization build-up, an internal holding coil generating a low holding field of at most 0.48 T in frozen spin mode, a microwave system needed for the DNP process, an NMR (nuclear magnetic resonance) system to determine the target material's polarization degree, and an adequate target material (deuterated butanol, or in short, dbutanol). These components will be described in detail below.

Polarization Any polarization of a given system arises from the orientation of the system's spin I with reference to a certain axis z which is described by a series of $2I$ *orientation parameters*, i.e. expectation values of irreducible spin tensors [Jeffries60]. The parameters interesting for the description of an assembly's polarization are the vector polarization

$$P_z = \frac{1}{I}\frac{\sum_i \langle \Psi_i \mid I_z \mid \Psi_i \rangle N_i}{\sum_i N_i} \equiv \frac{\langle I_z \rangle}{I} \tag{2.9}$$

and the tensor polarization

$$P_{zz} = \frac{1}{I(2I-1)}\left(\frac{\sum_i 3\langle \Psi_i \mid I_z^2 \mid \Psi_i \rangle N_i}{\sum_i N_i} - I(I+1)\right) \equiv \frac{\langle 3I_z^2 - I(I+1)\rangle}{I^2}. \tag{2.10}$$

N_i and Ψ are the population and normalized wave function for the i^{th} energy level, respectively. The polarization degree of an assembly of particles with spin $I = 1/2$ is given by

$$P_z = \frac{N_{+\frac{1}{2}} - N_{-\frac{1}{2}}}{N_{+\frac{1}{2}} + N_{-\frac{1}{2}}} \qquad (P_{zz} \text{ vanishes}), \tag{2.11}$$

while the vector and tensor polarization of an assembly of spin $I = 1$ particles are

$$P_z = \frac{(N_{+1} - N_0) + (N_0 - N_{-1})}{N_{+1} + N_0 + N_{-1}} = \frac{N_{+1} - N_{-1}}{N_{+1} + N_0 + N_{-1}} \tag{2.12}$$

and

$$P_{zz} = \frac{(N_{+1} - N_0) - (N_0 - N_{-1})}{N_{+1} + N_0 + N_{-1}}. \tag{2.13}$$

$N_{\pm\frac{1}{2}}$ and N_i, $i \in \mathbb{Z}_0$ are the relative populations of the various spin projections on the respective quantization axis—usually the direction of the magnetic field B_0. The vector polarization value for thermal equilibrium is given by the *Brillouin function*

$$\begin{aligned} P_I &= \mathcal{B}_I\left(\frac{g_I \mu_M I B_0}{kT}\right) \\ &= \frac{2I+1}{2I}\coth\left(\frac{2I+1}{2I}\cdot\frac{g_I\mu_M I B_0}{kT}\right) - \frac{1}{2I}\coth\left(\frac{1}{2I}\cdot\frac{g_I\mu_M I B_0}{kT}\right). \end{aligned} \tag{2.14}$$

μ_m is the magneton, g_I the particle's g-factor. While the gyromagnetic ratio $\gamma = g_I\mu_M/\hbar$ is an intrinsic feature of the particle, the ratio B_0/T can more or less be chosen at will within the restrictions given by current technology. In any case, the latter ratio has to be as high as at least 10^3 T/K to create a sizeable nuclear thermal equilibrium polarization. Although this is achievable—HD-gas for example can be polarized using this technique at a magnetic field of 17 T and temperatures of 15 mK—the drawbacks make this procedure inapplicable for the purposes needed for the GDH experiment. These drawbacks are (the given values refer to the above mentioned HD-gas target example):

- very long polarization build-up time of several weeks,
- low polarization values of at most some 20 percent,
- limitation to low intensity beams due to low acceptable heat input,
- low radiation resistance,
- unrecoverable polarization once the material has depolarized for any reason.

Dynamic Nuclear Polarization. A much more suitable technique to gain a sizeable polarization is *dynamic nuclear polarization (DNP).* It uses the fact that the polarization of unpaired electrons—only these are polarizable—in a given system in thermal equilibrium is close to 100 percent due to their high magnetic moment, even at relatively high temperatures ($T \sim 1$ K) and low magnetic fields B_0 (some Teslas). The electron polarization is then transferred to the nuclei by irradiation with saturating microwaves of a frequency slightly off the electron Larmor frequency $\omega_s = \gamma_s B_0$, where γ_s is the electron's gyromagnetic ratio. This transfer is possible due to the *resolved solid state effect.* It describes the coupling of the nuclear to the electronic magnetic moments by the magnetic field $B_s = \hbar\gamma_s/r^3$ produced by the electron at the site of the nucleus at distance r. For simplicity, the following considerations will focus on a nuclear system of spin $I = 1/2$. A treatise for $I = 1$ can be found in [Jeffries60]. Figure 2.10 shows the corresponding level scheme for a dipolarly coupled electron-nucleus system with nuclear spin $I = 1/2$. ω_s, ω_I are the electronic and nuclear Larmor frequencies, W are the induced transition probabilities for an uncoupled electron-nucleus pair (*allowed* transitions), T_s^{-1} their spontaneous thermal relaxation rates, and V are the transition probabilities for the coupled pairs (*forbidden* transitions). The terms *allowed* and *forbidden* refer to the states that are allowed and forbidden *without dipole coupling* of electrons and nuclei, although both transition probabilities may become fairly comparable in some cases. Denoting the uncoupled "pure" states $|{+}{+}\rangle$, $|{+}{-}\rangle$, $|{-}{+}\rangle$, and $|{-}{-}\rangle$, as shown in Figure 2.10, these states must be replaced in first-order perturbation theory with the states

$$\begin{aligned} |a\rangle &= p\,|{+}{+}\rangle - q^*|{+}{-}\rangle, \\ |b\rangle &= p\,|{+}{-}\rangle + q\;|{+}{+}\rangle, \\ |c\rangle &= p\,|{-}{+}\rangle + q^*|{-}{-}\rangle, \\ |d\rangle &= p\,|{-}{-}\rangle - q\;|{-}{+}\rangle, \end{aligned} \tag{2.15}$$

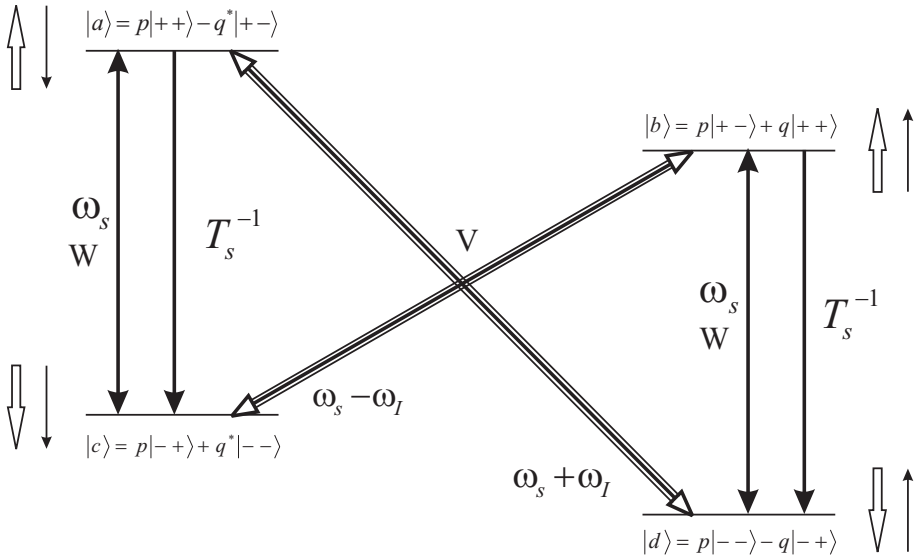

Figure 2.10. Four-level scheme of a dipolarly coupled electron-nucleus pair for a spin 1/2 nucleus. The relative spin orientations are symbolized at the margins; open arrows: electron spin orientation, thin arrows: nuclear spin orientation. Allowed transitions (that occur with probability W) are denoted by single arrows, forbidden transitions (probability V) by triple arrows. The thermal relaxation rate is approximately T_s^{-1}, c. f. [Abragam78] and [Goertz02].

i.e. basically the pure states with a small admixture

$$|q| = \frac{3\hbar\gamma_I\gamma_s}{2\omega_I r^3}\sin\theta\cos\theta\exp(i\phi) \sim \frac{B_s}{B_0} \sim 10^{-4} \ll 1 \tag{2.16}$$

from the nuclear spin state of opposite magnetic quantum number [Abragam78]. θ is the angle between the applied magnetic field and the distance vector $\vec{r}$ between the two involved spins. It follows that $|p| = \sqrt{1-|q|^2} \approx 1$.

Using the population numbers of the four states a, b, c, d, one can define the respective polarizations

$$P_s = \frac{n_- - n_+}{n_- + n_+} \equiv \frac{n_- - n_+}{N_s} \qquad \text{with } n_+ = a + b,\ n_- = c + d, \tag{2.17}$$

and

$$P_I = \frac{N_- - N_+}{N_- + N_+} \equiv \frac{N_- - N_+}{N_I} \qquad \text{with } N_+ = b + d,\ N_- = a + c. \tag{2.18}$$

The time evolution of the respective polarizations is then described by

$$\frac{\mathrm{d}P_s}{\mathrm{d}t} = -V(P_s - P_I) + \frac{1}{T_s}(P_s^0 - P_s), \tag{2.19}$$

$$\frac{\mathrm{d}P_I}{\mathrm{d}t} = \frac{N_s}{N_I}V(P_s - P_I) - \frac{1}{T_I}(P_I - P_I^0), \tag{2.20}$$

where the respective numbers in thermal equilibrium are denoted with superscript '0' and the relaxation times are T_s and T_I. From Equation 2.20 it is clear that a high nuclear polarization

increase rate depends on a high concentration of electrons N_s/N_I, on a large nuclear relaxation time T_I, and on a large difference in electronic and nuclear polarization $P_s - P_I$. This implies that the electronic relaxation time T_s should be small:

$$\frac{N_I T_s}{N_s T_I} \ll 1. \tag{2.21}$$

This means that the total rate of spontaneous electron spin flips N_s/T_s should considerably exceed the rate of spontaneous nuclear spin flips N_I/T_I, so the stationary polarizations for $\mathrm{d}P_{s,I} \,/\, \mathrm{d}t = 0$ reduce to

$$P_s = \frac{P_I^0 + P_s^0 \left(\frac{N_I}{N_s T_I V} + 1\right)}{\frac{N_I}{N_s T_I V} + 1} \sim P_s^0 \quad \text{due to } P_I^0 \ll P_s^0, \tag{2.22}$$

$$P_I = \frac{P_I^0 \frac{N_I}{N_s T_I V} + P_s^0}{\frac{N_I}{N_s T_I V} + 1}. \tag{2.23}$$

If also

$$N_s V \gg \frac{N_I}{T_I}, \tag{2.24}$$

i.e. the rate of induced transitions of electron spins $N_s V$ is much higher than the nuclear relaxation rate N_I/T_I, the nuclear polarization is only limited by the electronic polarization value in thermal equilibrium:

$$P_I^{\max} = P_s^0. \tag{2.25}$$

In a real material, the normal electron spin concentration is 10^{-4} to 10^{-3} per nucleus, i.e. one unpaired electron spin has to polarize some thousand nuclei in its vicinity, an effect named *spin diffusion*—the resonant mutual spin-flip of neighboring nuclear spins. This effect will become the less effective the higher the polarization drainage due to additional relaxation channels for the nuclear polarization. These are opened by impurities or crystalline imperfections, hence severely diminishing the maximum achievable nuclear polarization.

Target Material. Considering the conditions and requirements pointed out above, deuterated butanol was chosen as target material. It has a dilution factor—the fraction of polarized deuterons—of $f_D = 23.8$ percent, since the residuals (carbon and oxygen) are spinless, which fact minimizes the polarized background. To provide a sufficient density of paramagnetic centers ($1.82 \cdot 10^{19}$ electrons per cm^3 in case of deuterated butanol) for DNP, the material was chemically endowed with 0.5-percent-by-weight porphyrexide dissolved in 5-percent-by-weight water. The radiation damage from the A2 photon beam is negligible and the temperature stability is much better than that of TEMPO doped butanol. The material is shock-frozen, forming beads of 2 mm diameter, and placed in a cylindrical PTFE container of 2 cm length and diameter. The effective filling factor (fraction of deuterated butanol in the target cell container) of the material is $f_F = 63$ percent.

Refrigerator. The refrigerator basically has to fulfill the following requirements:

- Provide a cooling power of more than 30 mW at 300 mK for 10 cm^3 of target material during the DNP process;
- reach temperatures below 70 mK for frozen-spin mode;
- allow maximum accessible solid angle for the detector system.

A horizontal refrigerator of ^{3}He/^{4}He dilution type was built which allows one to place the cryogenic components at backward angles and thus obtaining an azimuthally symmetric mass distribution. A cooling power of at most 50 mW at 300 mK and a base temperature of 40 mK are available.

The target material can be placed with only a minute warming in the refrigerator using a sliding insert that also contains the NMR- and microwave guides. This insert is mounted in the refrigerator from the upstream side.

Internal Holding Coil. A superconducting internal coil is used during frozen-spin mode to provide the magnetic holding field of $B \approx 500$ mT at a homogeneity of better than 10^{-3} over the target cell region. Its fringe field does not exceed 20 mT outside the refrigerator. It is made up of four layers of 1050 turns each, consisting of a 100 μm multi-filament NbTi-wire with 10 μm varnish. The assembly's total thickness of 780 μm allows all target reaction products to traverse almost unaffectedly.

Polarizing Magnet. The magnetic field needed for the DNP process is provided by a superconducting solenoid built by the Saclay group. Its maximum magnetic field of 6.5 T (2.5 T during DNP process) is homogeneous better than 10^{-4} over the whole target sample region. In the A2 hall it is mounted on a rail system that allows a quick and reproducible positioning to enclose the static target during the polarization process, and as quick a removal for data taking periods.

Microwave System. The saturating electromagnetic field needed to create the nuclear polarization during the DNP process is created using a carcinotron as microwave source. It delivers a power output of 3.5 W at a frequency of 70 GHz—the electronic Larmor frequency at a magnetic field of 2.5 T—with a stability of 10^{-4}. This stability is needed to drive only single transitions, c. f. Figure 2.10. The microwaves are fed into the refrigerator using rectangular waveguides. During the DNP process, the microwave frequency is modulated in a bandwidth of 20 MHz with a frequency of 1 kHz. Thus, the maximum polarization for deuterons is increased by a few percent while also decreasing the polarization build-up time.

NMR. The purpose of the NMR (nuclear magnetic resonance) measurement is to determine, as accurately as possible, the target material's polarization value since it directly enters the evaluation of the helicity dependent cross sections. To this end, the target material is surrounded by a small coil working as sensing probe of a series Q-meter. This continuous wave RF circuit is

driven at the nuclear Larmor frequency inducing transitions between the nuclear Zeeman levels. The energy exchange between the target material and the Q-meter leads to a linear dependence of the coil's impedance $Z(\omega)$ and the complex magnetic susceptibility χ

$$Z(\omega) = R + i\omega L(1 + \eta\chi(\omega)), \tag{2.26}$$

$$\chi(\omega) = \chi'(\omega) + i\chi''(\omega), \tag{2.27}$$

where η is the effective filling factor of the target material, L the inductance for $\chi = 0$, ω the RF oscillator's frequency. χ'—the real part of the magnetic susceptibility (dispersion)—is the resulting inductance, χ''—the imaginary part—is basically the absorption of the RF field, i.e. the energy exchange caused by the nuclear Zeeman transitions. This quantity directly depends on the populations of the nuclear Zeeman levels and is hence a direct measure of the polarization of the target material. The Zeeman levels are broadened due to nuclear spin-spin interaction, so the polarization value P is an integral over the resonance region

$$P = c \int_{\Delta\omega} \chi''(\omega)\,\mathrm{d}\omega\,. \tag{2.28}$$

The factor of proportionality c needs to be obtained from a calibration measurement at known temperature and known magnetic field in thermal equilibrium. The material's polarization degree can then be calculated using the Brillouin function (Equation 2.14).

2.5 Detector Setup

For the studies of helicity dependencies of photo-nuclear cross sections it is necessary to have large angular and momentum acceptance detectors with sizeable detection efficiencies for both charged and uncharged particles. Moreover, by using high resolution tracking detectors to reconstruct particle trajectories it is possible to improve the particle identification beyond the limits given by the energy resolution provided by plastic scintillators alone. The detector DAPHNE that was built to meet these requirements as much as possible will be described in the following subsection.

2.5.1 DAPHNE.

DAPHNE is the main detector that was used during the GDH-experiment at MAMI [Audit91]. It was designed and built at the end of the 1980s by the groups of Saclay and Pavia at the *Commisariat à l'Energie Atomique* in Saclay, France. Its key characteristics are given in Table B.1 on page 97. DAPHNE consists of three principal parts arranged as a set of coaxial cylinders:

- Vertex detector,
- plastic scintillator calorimeter, and
- a sandwich of plastic scintillators and steel/lead/aluminum layers.

These parts will be described in more detail below.

Vertex Detector. The innermost part consists of three concentric cylindrical multi-wire proportional chambers (henceforth referred to as *MWPC*) with cathode strip readout. The walls are made of 1 mm thick Rohacell covered by 25 μm kapton foil with the cathode strips laminated on the interior surfaces. These strips are 0.1 μm thick by 4 mm wide aluminum layers with a 0.5 mm gap between adjacent strips. They are wound helically in opposite directions at angles $\pm 45^\circ$ with respect to the anode wires. The latter are made of 20 μm diameter tungsten wires arranged parallel to the cylinder axis in 2 mm intervals around the circumference. The anode-cathode distance amounts to 4 mm. The chambers are operated using a mixture of 74.5 percent argon, 25 percent ethane, and 0.5 percent freon. The geometrical characteristics are given in Table 2.1.

A swiftly moving charged particle passing through the MWPC creates a cloud of electron-ion pairs along its path. The electrons are accelerated towards the positive wires creating an avalanche of electron-ion pairs on their way by secondary ionization. The secondary electrons are quickly collected by the positive wires while the positive ion cloud moves slowly towards the cathode strips. Since the chambers are operated in proportional mode, the charges created by secondary ionization are proportional to the charges created by the original traversing particle. This analog information is read out via Alcatel 1757 charge amplifiers plus LeCroy FERA 4300(B) analog-to-digital converters, c. f. Section 3.6 on page 54. The determination of the center of the charge distribution induced on the strips allows one to find the intersection point of the involved internal and external strips with a ϑ-dependent precision of $0.6^\circ < \Delta\vartheta < 1.1^\circ$ for the polar angle. Ambiguities arising from the fact that the internal and external strips have *two* intersection points along the z-axis are resolved taking the hit wires into account (Figure 2.11). The latter are read out using a LeCroy PCOS 2735PC amplifier/discriminator. The resulting longitudinal resolution is $0.3\,\text{mm} < \Delta z < 1.5\,\text{mm}$. The fixed inter-wire spacing gives a precision of $\Delta\varphi = 2^\circ$ for the azimuthal angle. Having evaluated the impact points of all three chambers, the track is reconstructed by fitting a straight line to these points. Since, due to the above mentioned uncertainties,

	Chamber		
	1	2	3
Length [mm]	360	560	760
Internal radius [mm]	60	92	124
External radius [mm]	68	100	132
Number of wires	192	288	384
Number of internal strips	60	92	124
Number of external strips	68	100	132

Table 2.1. Geometrical specifications of the vertex detector.

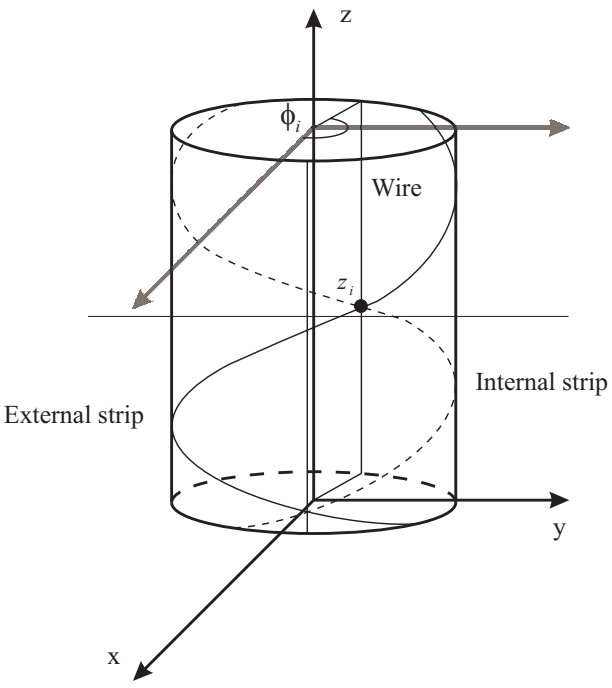

Figure 2.11. MWPC: Reconstruction of the impact point of a traversing particle.

the three points will never precisely build a straight line, the condition that the vertical angle β be greater than 172° is required, i. e. the point from Chamber 2 must not deviate by more than 2.3 mm (approx. one inter-wire gap) from the straight line that is given by the points from Chambers 1 and 3 (Figure 2.12). The track reconstruction efficiency is approx. 98.5 percent for single tracks and about 95 percent for double tracks.

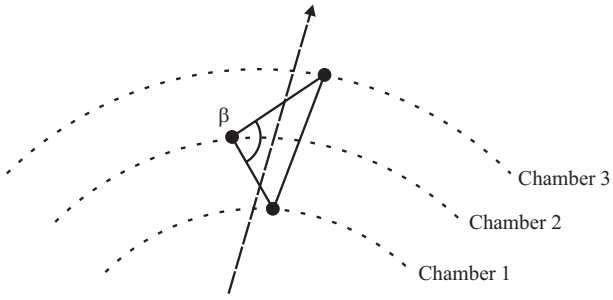

Figure 2.12. MWPC: Track reconstruction.

Scintillation detectors and sandwich. The above mentioned vertex detector is surrounded by a six layer plastic-scintillator calorimeter. The scintillator layers are labeled A to F, each of them consisting of 16 longitudinal bars mounted in such a way as to form a regular 16-sided polygon. The outer three layers (D–F) alternate with steel/lead and aluminum converters/absorbers forming a sandwich detector which adds a useful detection efficiency for photons originating from π^0-decay. All scintillators are read out by photomultipliers at both ends—except for layer A which are read out from beam entry side only. Table B.2 lists the geometrical specifications of the scintillators and converters/absorbers. The inner three layers (A–C) allow the identification of charged particles and the determination of their kinetic energies. For this purpose, Layer A is used as ΔE-detector, while Layer B provides the full energy information, as especially many protons stop in this layer already. Charged particles not stopping in the first three layers but reaching the sandwich detector can be identified using an extended $\Delta E/E$-method named *range-fit* [Braghieri94]. This method is explained in more detail in Section 4.5.

2.5.2 MIDAS.

MIDAS, the *MIcrostrip Detector Array System*, was built by the *Istituto Nazionale di Fisica Nucleare (INFN), Sezione di Pavia*, Italy [Altieri00]. This setup is an add-on mounted close to the DAPHNE target. It allows for the detection of charged hadrons emitted to polar angles between 7.5 and 16.5 degrees thus reducing the corrections for extrapolations to full solid angle required for total photo-absorption cross sections. Its setup is shown in Figure 2.13.

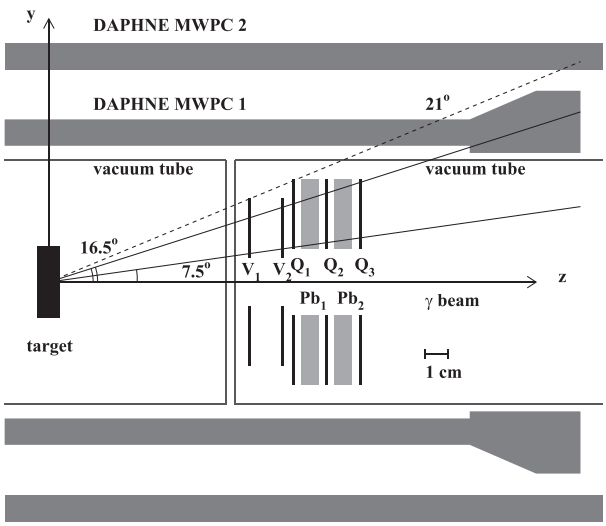

Figure 2.13. MIDAS detector mounted adjacent to the cryotarget.

Since DAPHNE's mechanical frame prevents particle transmission in the polar angular region between 5 and 21 degrees, MIDAS has to be mounted *on*

frame, i. e. as close to the target as possible without disturbing particle emission in DAPHNE's acceptance. Due to the very limited space available close to the target, MIDAS meets the primary objective of compactness by utilizing silicon detectors. It consists of two major parts: the tracking detector for trajectory reconstruction and the sandwich detector for particle identification and energy measurement. A central hole allows the primary photon beam to pass through.

The tracking part is made up of two annular double-sided semiconductor silicon detectors V_1 and V_2. The p-side of the tracking detectors is divided into 48 concentric rings, while the n-side is segmented into 16 radial sectors. The resolution is approximately 12 degrees in azimuth and about 1.4 degrees in polar angle.

The second part consists of an annular silicon-lead sandwich (Q_1, Q_2, Q_3) with single sided silicon detectors where only the p-side is segmented radially (quadrants). This part is used for particle identification using the range-fit method adapted to the MIDAS geometry. It allows to identify protons with a pion contamination of less than three percent. The sandwich also provides the MIDAS-trigger. A coincidence $Q_1 \oplus Q_2$ together with a high threshold selects low energy protons with a high energy loss rate that stop in MIDAS. High energy hadrons produce a triple coincidence $Q_1 \oplus Q_2 \oplus Q_3$ and are not stopped in MIDAS. These triggers allow the detection of protons with energies $T_p > 60$ MeV and of pions with energies $T_\pi > 50$ MeV while suppressing 99 percent of the electromagnetic background. The remaining background basically originates from pair production processes from material placed upstream (target material, target windows, etc.) In most of these cases only one of the electrons enters MIDAS, while the second is emitted at very small polar angles and can thus be suppressed by the Čerenkov detector that will be described in the following subsection.

2.5.3 Čerenkov Detector.

A detailed description of this detector can be found in [Lannoy00], a schematic of the detector is presented in Figure 2.14. The inner volume is filled with nitrogen gas. The Čerenkov light that is produced in the aerogel radiator close to the entrance window or in the nitrogen is focused on the photomultiplier by a large ellipsoidal mirror. A funnel is mounted close to the photomultiplier to increase the light yield. The detection efficiency is $(99.99 \pm 0.002)\%$ for electron energies above 3 MeV. Together with the fact that at MAMI energies no hadronic reaction products are emitted with sufficient kinetic energies to create Čerenkov light in the media used in the detector, this

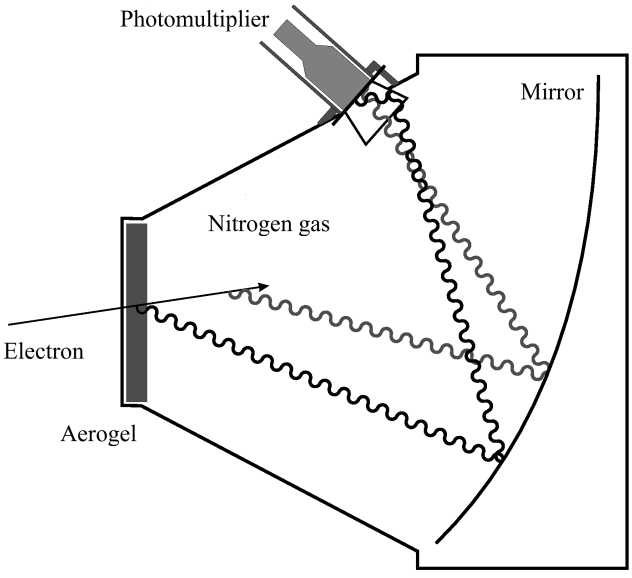

Figure 2.14. Schematic of the Čerenkov detector.

allows to operate the Čerenkov detector as a threshold detector. It suppresses the electromagnetic background contributions to the reactions under study in the GDH experiment significantly. For this purpose the Čerenkov detector is operated in anti-coincidence with MIDAS and the forward components.

2.5.4 Forward Components.

The forward components consist of the *Scintillator from Tübingen for Angular Reconstruction* (STAR) and the *Far Forward Wall* (FFW) detectors [Sauer96]. They cover the polar angular region $2^\circ < \vartheta < 5^\circ$. The STAR detector consists of a large square scintillator sheet with a photomultiplier tube at each corner. It serves as a trigger plate for charged particles. It is followed by an array of nine segmented concentric scintillator rings from which information on the polar angle of the charged particle can be obtained. A trigger plate similar to that of STAR is implemented in the FFW detector. It is followed by a scintillator-lead sandwich acting as a shower detector for photons originating from π^0 decay. The information given by these components is not yet included in the analysis procedure.

2.5.5 A2 Hall.

Figure 2.15 shows the arrangement of the aforementioned detectors in the A2 hall where the GDH experiment was carried out. All components are mounted on a rail system to easily allow re-arrangements of the setup for re-polarization and data-taking periods. The figure shows the setup in an intermediate state between these two periods. When proceeding to a re-polarization phase, the polarization magnet would be pushed towards the photon beam axis and then upstream to cover the target nozzle. Instead, when continuing with a data-taking period, the DAPHNE frame including the Čerenkov detector and the forward rack would be pushed towards the target so that the latter would be centered inside DAPHNE and be placed directly in front of MIDAS. The MAMI electron beam would enter from below.

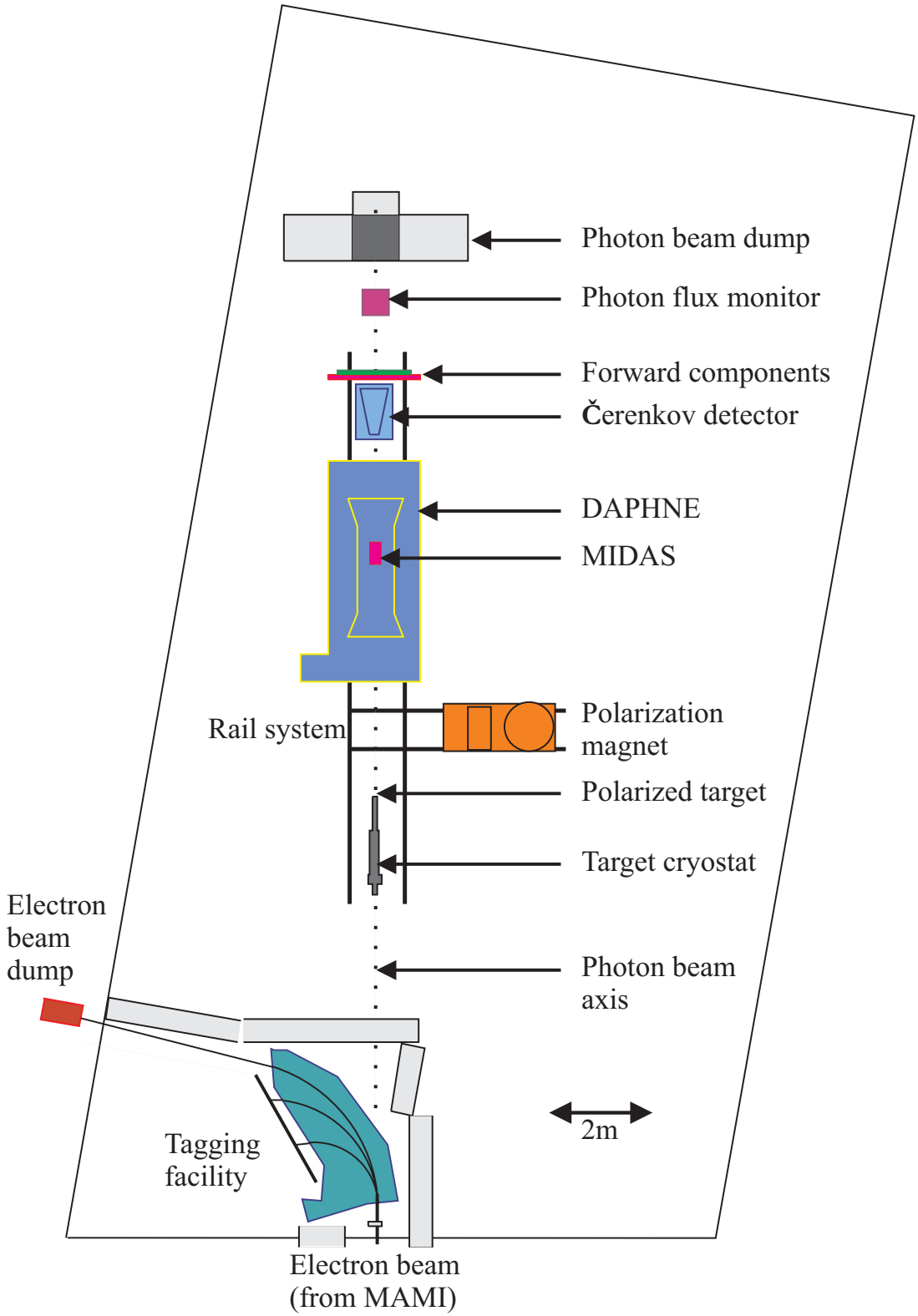

Figure 2.15. Floor plan of the A2 hall.

Chapter 3

Preparations

AFTER the 1998 GDH experiment the detector system DAPHNE was in a status that did not allow further experiments without a considerable loss in the quality of the acquired data. The attenuation lengths had become critically low (see Table 3.1 and Figure 3.16), due to an EU Directive it was no longer allowed to supply the wire chambers with the nominal quenching gas and hence it was difficult to keep them at the necessary voltages, and—after a total of more than 500 hours of beam time—the readout electronics operated on the verge of stability. In preparation of the nGDH experiment scheduled for 2002/03, this status had to be improved significantly—a task that was carried out in the course of this thesis. To this end, DAPHNE was dismantled and the plastic scintillators exchanged with new material. The wire chambers were taken out and shipped to the collaborators at the *Istituto Nazionale di Fisica Nucleare, Sezione di Pavia,* Italy, for refurbishing and to find a new gas mixture. The new plastic scintillators had to be glued to their light-guides, packed, and—without the wire chambers—new techniques had to be developed to test them before re-assembly. In addition, the material for the A layer scintillators that had been bought two years before the start of our work was not found to be useful because of defects in the plastics' surfaces. Several attempts to recover this material by polishing the surface—in our workshops as well as manually—failed since the effective attenuation lengths could not be improved significantly, so new material had to be purchased. A very high start-value of the attenuation lengths is desirable because due to the normal aging process the attenuation lengths decrease exponentially with time. This

Layer	1994	1997	Change
A	1140 ± 40	850 ± 60	-290 ± 70 (-34%)
B	1020 ± 30	793 ± 14	-230 ± 30 (-29%)
C	472 ± 6	400 ± 30	-70 ± 30 (-18%)
D	644 ± 14	530 ± 20	-110 ± 20 (-21%)
E	760 ± 30	620 ± 20	-140 ± 30 (-23%)
F	650 ± 11	520 ± 10	-130 ± 15 (-25%)

Table 3.1. History of the attenuation lengths of the plastic scintillator layers of DAPHNE (average over all sectors of each layer) measured in 1994 and 1997. All dimensions in mm.

behavior had been observed already for the 1997/98 DAPHNE detector. The light-guides had undergone an aging process, too, their transmissions varying by about 15 percent around an average value. Ten of 32 light-guides of Layer B were replaced, and ten of 16 of Layer A. The light-guides of the remaining layers were found suitable for future use.

The determination of the effective attenuation lengths, c. f. Sections 3.4 and 3.5, was important, because it allowed to quality-test the freshly glued connection between the scintillators and their light-guides. If, for any reason, this connection was bad or loosened or broke, the according effective attenuation length would decrease significantly and indicate this problem. Since such a decrease is quite significant (a broken connection of an A layer detector in the 1997 DAPHNE setup resulted in a decrease in the effective attenuation length by a factor two compared to the value before and to the other detectors of the same layer) these measurements did not need to give highly accurate results. An error level of 10 to 20 percent would still be regarded acceptable. However, even the least accurate of our methods delivered results below the minimum requirement of a 10 percent error level.

This chapter will give a short introduction to the interaction of fast particles with matter (Section 3.1), to the scintillation process (Section 3.2), and the definition of an (effective) attenuation length (Section 3.4), and will then focus on the test measurements and the results for the effective attenuation lengths (Section 3.5). The modifications on the readout electronics are the topic of the second part of this chapter.

To avoid later confusion when presenting the analysis results in the Chapters 4 and 5, I would like to point out that the work to be described in this chapter was done in preparation for the *2003 n*GDH experiment, while the data that were analyzed are from the *1998 pilot* experiment on the deuteron.

3.1 Interaction of Fast Charged Particles with Matter

The interaction of swiftly moving particles with matter is—though quite complicated to handle theoretically when going into detail and for high accuracy—sufficiently well known on an accuracy level of one percent. The key processes involved by which a fast particle loses kinetic energy are ionization and atomic excitation of the matter, and radiative energy transfer (bremsstrahlung, Čerenkov light). Except for electrons, the radiative energy losses are usually negligible, especially for the mean kinetic energies of the particles that were utilized for the tests of the DAPHNE scintillators, so the focus in the following discussion will be on heavier particles. The ionization-energy loss is described approximatively by the Bethe-Bloch equation

$$-\frac{\mathrm{d}E}{\mathrm{d}x} = 4\pi N_A r_e^2 m_e c^2 z^2 \frac{Z}{A}\frac{1}{\beta^2}\left[\frac{1}{2}\ln\frac{2m_e c^2\beta^2\gamma^2 T_{\max}}{I^2} - \beta^2 - \frac{\delta}{2}\right]. \tag{3.1}$$

$T_{\max}$ is the maximum kinetic energy which can be transferred to a free electron in a single encounter, N_A is Avogadro's number, $r_e = e^2/4\pi\varepsilon_0 m_e c^2$ the classical electron radius, $m_e c^2$ the electron's rest energy, ze the charge of the incident particle, β, γ its well known relativistic kinematic variables, Z, A the atomic number and atomic mass of the absorber, I its mean excitation energy in eV, and δ the density effect correction.

As mentioned before, Equation 3.1 can reproduce the energy loss of, for instance, charged muons in copper with an accuracy of one percent in the energy range between 6 MeV and 6 GeV,

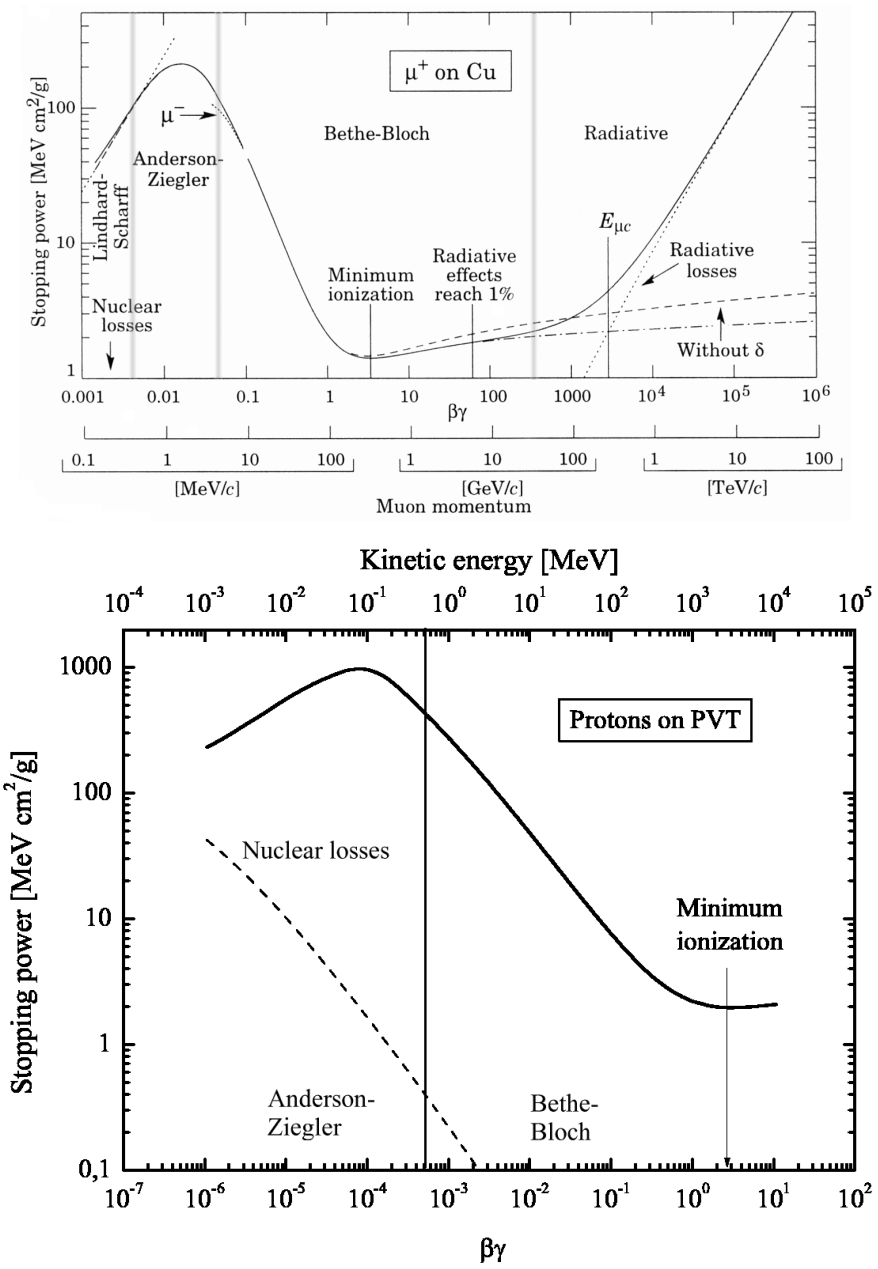

Figure 3.1. Energy loss (=stopping power) as a function of $\beta\gamma = p/Mc$. Solid curves represent the total energy loss. The vertical lines indicate boundaries between different approximations. *Top:* Stopping power for μ^+ on copper. Especially at very low momenta the energy loss depends strongly on the electronic configuration of the absorber material. In this region the particle's charge has also an effect on the ionization energy loss (Barkas effect, dotted line, labeled μ^-). E_{μ_c} labels the so-called *critical energy* where ionization and radiative energy losses are equal. For ultra-high kinetic energies radiative energy losses are dominant ($\beta\gamma > 10^4$). The figure has been taken from [Alvarez04], p. 242. *Bottom:* Stopping power for protons on PVT (polyvinyltoluene, the solvent used in most solid plastic scintillators). The dashed line represents the energy loss due to (non-ionizing) nuclear interactions. The data used for this plot were taken from [Berger00].

c. f. Figure 3.1, top. For energies below, shell corrections have to be applied. This is rather difficult since these corrections are extremely sensitive to the knowledge of the atomic energy levels of the absorber material. For hydrogen—the only element where the atomic energy levels can really be calculated—it is possible to derive proper shell correction values. For heavier elements the calculation of the energy levels becomes model dependent and it is no longer possible to stringently derive the necessary corrections without the use of experimental values for the mean ionization-energy I as a free parameter [Bichsel92]. For $0.01 < \beta < 0.05$ only phenomenological fitting formulae by Andersen and Ziegler are available at this time [Alvarez04]. At extremely low kinetic energies, e. g. protons of a few hundred eV, non-ionizing nuclear recoil energy loss is considered dominating the total energy loss, c. f. Figure 3.1, bottom. Another difficulty in regions of very low kinetic energy originates from the Barkas effect, i. e. different energy losses for positively and negatively charged traversing particles with otherwise identical properties [Barkas56]. For relativistic kinetic energies, the ionization energy losses depend on the density of the absorber material (hence *density effect*) as has been shown in [Fermi40]. At even higher energies radiative losses increase in importance and are dominant for ultra-relativistic particles. The energy where ionization losses equal radiative losses is called *critical energy.*

3.2 Scintillation in Organic Materials

An investigation of the scintillation process in organic materials is not the aim of this thesis, so the well known properties of this process will only shortly be recalled in this section. Exhaustive sources of detailed information on this topic are [Birks64], [Birks58]–[Birks71], [Nafisi67], [Al-Obaidi78], and [Hallam78]. In general, an organic scintillator consists of a solvent material—in case of solid scintillators mostly polyvinyl-toluene (PVT) like the DAPHNE scintillators—plus a certain concentration of solute that is responsible for the emission of detectable light. The scintillation in such a binary material is a two step process: 1) Energy deposition in the solvent by the traversing fast particle to produce excited states, 2) decay of these excited states back to the ground state. The former process has been discussed in the previous section, the latter will shortly be described in the following. For certain applications it is useful to have more than one solute. An energy transfer between the solutes would then be introduced in addition. However, since the same mechanisms are involved as in the energy transfer from solvent to solute, this step can be neglected in the following.

Investigations show that the spectral emission of the scintillator is characteristic of the solute [Bowen49], although usually present in small concentrations only. The necessary energy transfer from the solvent to the solute has been studied in e. g. [Powell71]. Three basic mechanisms are to be considered:

1. Radiative re-absorption which is simply the emission of a (real) photon by one molecule and its subsequent re-absorption by another molecule [Birks54]. Radiative energy transfer can occur from excited polymer segments to residual monomers, i. e. monomers that did not take part in the polymerization reaction, and to solute molecules. For this an overlap between fluorescence and absorption spectra of the involved substances is necessary.

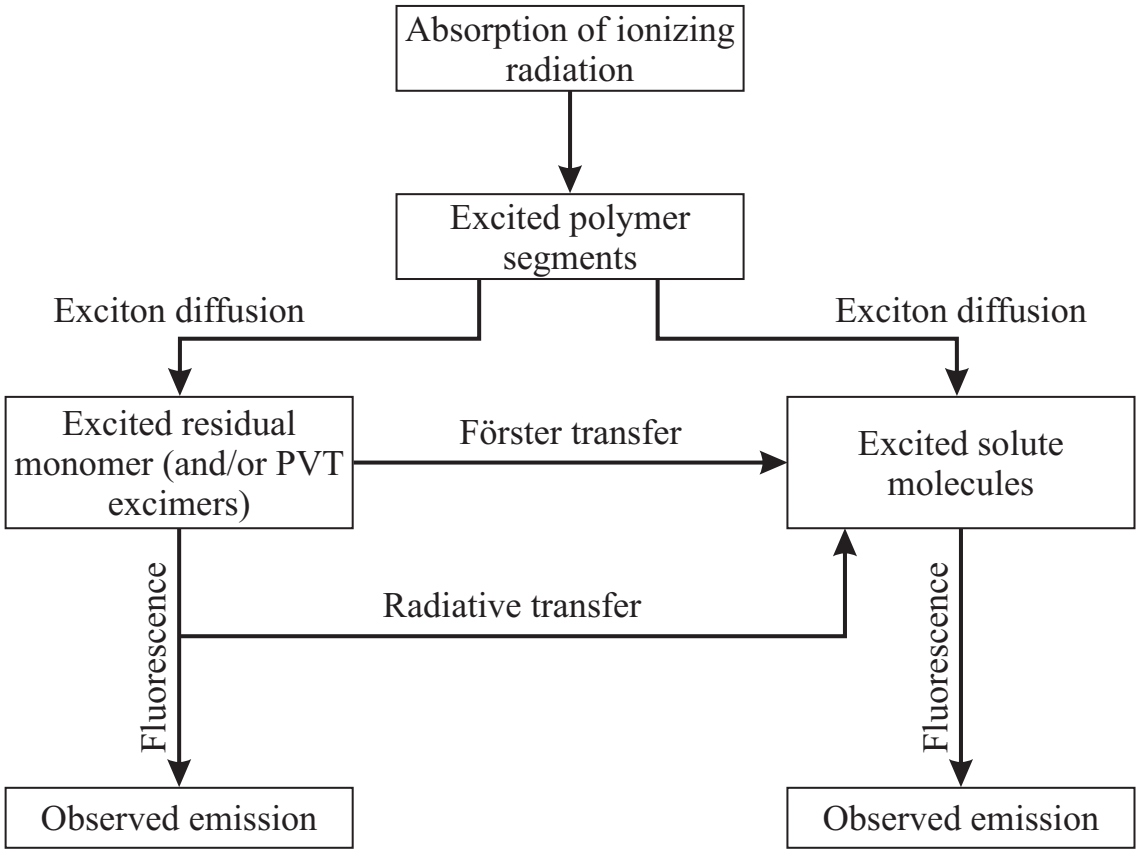

Figure 3.2. Kinetic scheme of the scintillation process [Hallam78].

2. Long-range resonant interaction which involves the transfer of a virtual photon from one molecule to another through the multipole-multipole coupling of their Coulomb fields, also known as *Förster transfer* [Förster48, Dexter53]. A theoretical treatment of this radiationless single-step transfer process of electronic excitation energy from a donor to an acceptor has been presented by Förster in 1948, who based his model on an interaction between the dipole moments of the donor and acceptor.

3. Exciton diffusion and trapping in which the excitation energy migrates through the host lattice until it is trapped at an impurity [Franck38]. Excited polymer segments can transfer energy to neighboring segments thus resulting in a delocalization of excitation energy analogous to exciton diffusion in organic molecular crystals. Excitons diffuse through the material until they either decay spontaneously or are trapped. Trapping centers may be solute molecules, residual monomer or PVT excimer forming sites. Excimers are dimers which form a bound state in an excited electronic state and which are unbound otherwise.

One should note that the intermolecular interaction in (2) and (3) is the same, but while (2) is a one-step process, (3) is a multi-step process.

Summarizing, the energy-transfer mechanism in plastic scintillators can be described by the kinetic scheme shown in Figure 3.2. In bulk polymerized plastic scintillators containing high solute concentrations, direct exciton trapping by the solute molecules is the dominant process,

but at low concentrations trapping is predominantly by residual monomer. In the latter case energy transfer from residual monomer to the solute can occur either radiatively or due to long-range resonance, and the degree of transfer is determined by the absorption spectrum of the solute.

Once the energy has passed to the solute molecules, the scintillation light is produced by transitions of the excited *free valence electrons* of the solute molecules occupying the π-*molecular orbitals* back to the ground state. These transitions are preceeded by a so-called *internal degradation*, a radiationless relaxation to an intermediate state. Due to this degradation the scintillator material becomes transparent for its own scintillation light because it separates the absorption and emission spectrum of the molecule by the amount of energy that went into internal degradation and hence the emitted light has insufficient energy to be re-absorbed. Usually, also states are excited where radiative transitions to the ground state are suppressed by multipole selection rules. These transitions are responsible for the slow component of the scintillation light.

3.3 Test of the Light-Guides

In modern experiments in particle physics it is necessary to convert the scintillation light to electrical signals that can be processed by a fast electronic readout. The conversion is done through photomultiplier tubes (in short, *photomultipliers* or PMTs) which use the scintillation photons to knock out electrons from their photo-cathode via the photo-effect. By applying high voltages, these electrons are accelerated and emit an increased number of secondary electrons from a dynode. In a cascade of typically some ten stages an electrical pulse is generated whose amplitude is proportional to the intensity of the impinging scintillation light. For a proper readout it is necessary to couple the PMTs to the plastic scintillators in such a way as to transmit as many scintillation photons as possible. Since usually the cross section of the scintillators is not compatible to the circular windows of the PMTs, the connection has to be established using *light-adaptors.* If, for any reason, the PMTs cannot be mounted close to the scintillator additional *light-guides* have to be employed to transfer the light from the scintillator to the PMT window. Usually no distinction is made between these two functions and the combination of adaptors and guides is simply referred to as *light-guide.* This nomenclature will also be followed in this thesis.

Ideally—neglecting all possible losses—a light-guide would transmit 100 percent of the incoming light which enters at angles that allow total reflection on the walls of the light-guide. This type is called *adiabatic* light-guide. However, phase-space considerations, c. f. [Garwin52], show that this ideal case is only allowed when the area of the entrance window equals the area of the exit window. Otherwise, the ideal light-guide can transmit at most the ratio

$$T_{\text{adiabatic}} \sim A_{\text{exit}}/A_{\text{entrance}}, \tag{3.2}$$

where the A_i are the respective areas of the entrance and exit windows of the light-guide and $A_{\text{exit}} < A_{\text{entrance}}$. For a *real* light-guide, all kinds of losses can occur, c. f. next section. Depending on the shape of the light-guide these losses can be significant and usually one has $T_{\text{real}} \ll T_{\text{adiabatic}}$.

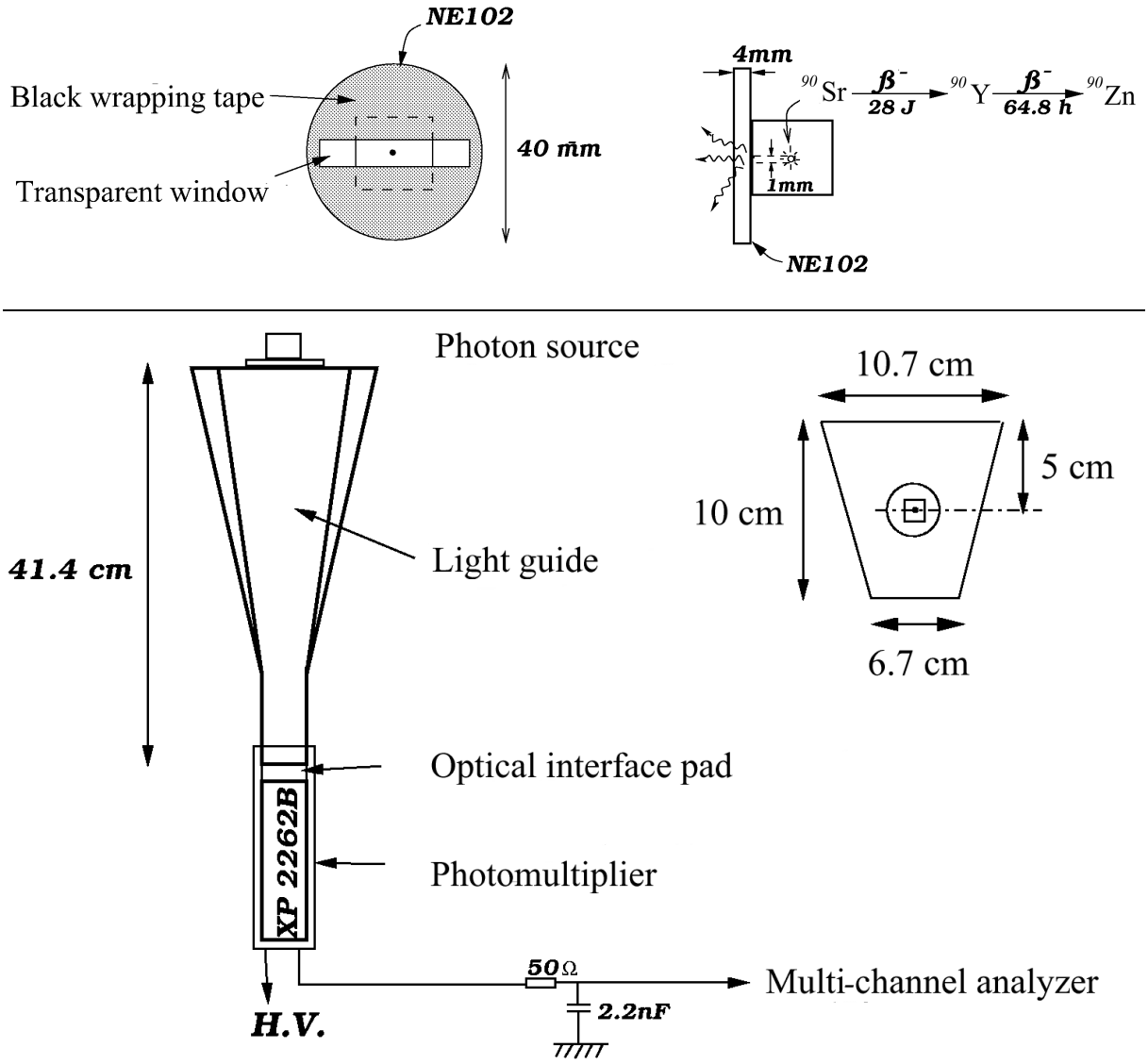

Figure 3.3. Setup for the test of the transmittance of the B layer light-guides. Top: Photon source. Bottom: Mounted light-guide read out by an XP2262B-type PMT.

For very complicated geometries it can be useful to go a different way, especially when sharp edges are involved. In such a case only a negligible fraction of light can be transferred by internal reflection. The method of choice would be to employ *wavelength shifting material* which absorbs the scintillation light and emits it at lower wavelength but—and this is the important point—*isotropically*. Although the absorption process is not 100 percent effective, the fraction of the isotropically emitted light that can be transferred through total internal reflection in the wavelength shifter usually exceeds the amount of light that would reach the PMTs without wavelength shifting [Garwin60]. This method is not used in DAPHNE itself, but in the 2003 forward wall which will be described later. In DAPHNE ordinary light-guides are used.

For the quality test of the DAPHNE light-guides a setup as shown in Figure 3.3 was used. A collimated Sr90 source was connected to a disc of an NE-102-type plastic scintillator. This disc was covered with one layer of a light-tight black adhesive tape except for a window where the scintillation photons could leave the scintillator. The window was placed on the light-guide to be examined and the transmitted photons were registered by an XP2262B-type PMT. Its output was fed to a multi-channel analyzer for pulse height analysis. The maximum of the resulting pulse height spectrum was then taken as transmittance. To suppress influences due to the varying quality of the coupling between light-guide and PMT, each measurement was repeated several times by subsequent re- and dismounting of the light-guide. The average value of these measurements was used for the further considerations. Because the absolute transmittance could not be determined, all light-guides of a certain layer were measured and an average value over all light-guides of that layer was calculated. A variation of the individual transmittances of more than 15 percent from the average was chosen as the criterion for replacement. Since the shape of the light-guides of different layers varied a lot, the setup as shown in Figure 3.3 had to be modified for each layer. Details for all measurements described here can be found in [Domingo00]. As already mentioned in the introduction of this chapter, ten of 32 light-guides of Layer B were replaced, and ten of 16 of Layer A. The light-guides of the remaining layers were found suitable for future use.

3.4 Effective Attenuation Length

The losses on the way through the scintillator material and the light-guides to the PMT are basically due to two main effects:

1. Attenuation through the scintillation material by self-absorption, with the intensity I decreasing exponentially
$$I(x) = I_0 \exp(-x/\ell), \tag{3.3}$$
where ℓ is the (physical) *attenuation length*, and x the path length traveled by the light.

2. Escape through the geometrical scintillator boundaries.

Effect (2) is by far the more important of the two since the dimensions of the scintillators of DAPHNE do not exceed the physical attenuation length ($\sim$1 m) significantly. In principle, the only light that could be detected is that reaching the PMTs directly or through total and partial

internal reflection, depending on the angle of incidence. For angles

$$\theta_B \geq \sin^{-1}\left(\frac{n_{\text{out}}}{n_{\text{scint}}}\right) \tag{3.4}$$

total reflection would occur and partial reflection otherwise. n_{scint}, n_{out} are the indices of refraction for the scintillator and the surrounding material respectively. The light collection in a large rectangular liquid scintillator has been studied both theoretically and experimentally in [Smith75] and the references therein. It was shown that the light loss in scintillation photons could be decreased significantly by covering the scintillator with highly reflective material (mirrors in the case of [Smith75]) to redirect escaping photons back into the scintillator. Further improvement can be achieved by polishing the surface of the plastic scintillator to increase internal reflection. The results of some measurements of the attenuation length for a rectangular plastic scintillator with various wrappings are shown in Figure 3.4 which has been taken from [Nicoll71]. As can be easily seen, the best attenuation lengths were achieved when wrapping the scintillator with aluminum foil all over except where the PMT was coupled to it (configuration C). Hence, the DAPHNE scintillators were covered with aluminized mylar foil. The resulting losses are not treated separately but are combined in an *effective attenuation length* λ. When not specified otherwise, the term "attenuation length" will henceforth be used synonym for the effective attenuation length.

3.5 Determination of the Effective Attenuation Lengths of the New Scintillators for DAPHNE

To measure the (effective) attenuation lengths of the new DAPHNE scintillators, the bars of Layers B through F were mounted as shown in Figure 3.5 (b). Choosing the origin of the coordinate system in the middle of the scintillator bar with positive distances to the right, one has the following correlations between the pulse heights $P_{1|2}$ of the PMTs and the coordinate x_0 of a traversing particle:

$$P_1(x_0) = P_1^0 \exp\left(\frac{-(L/2+x_0)}{\lambda}\right), \tag{3.5}$$

$$P_2(x_0) = P_2^0 \exp\left(\frac{-(L/2-x_0)}{\lambda}\right). \tag{3.6}$$

L is the length of the scintillator bar and the P_i^0 are factors that are proportional to the energy deposited in the scintillator by the traversing particle and to the amplification of the individual PMT. Dividing Equation 3.5 by Equation 3.6 and defining $P^0 \equiv \frac{P_1^0}{P_2^0}$ one has

$$\frac{P_1(x_0)}{P_2(x_0)} = P^0 \exp\left(-\frac{2x_0}{\lambda}\right) \tag{3.7}$$

which is independent of the scintillator length L.

For Layer A—which is read out from one side only, c. f. Figure 3.5 (a)—it has turned out to be appropriate using a slightly modified function, that is the sum of two exponential functions,

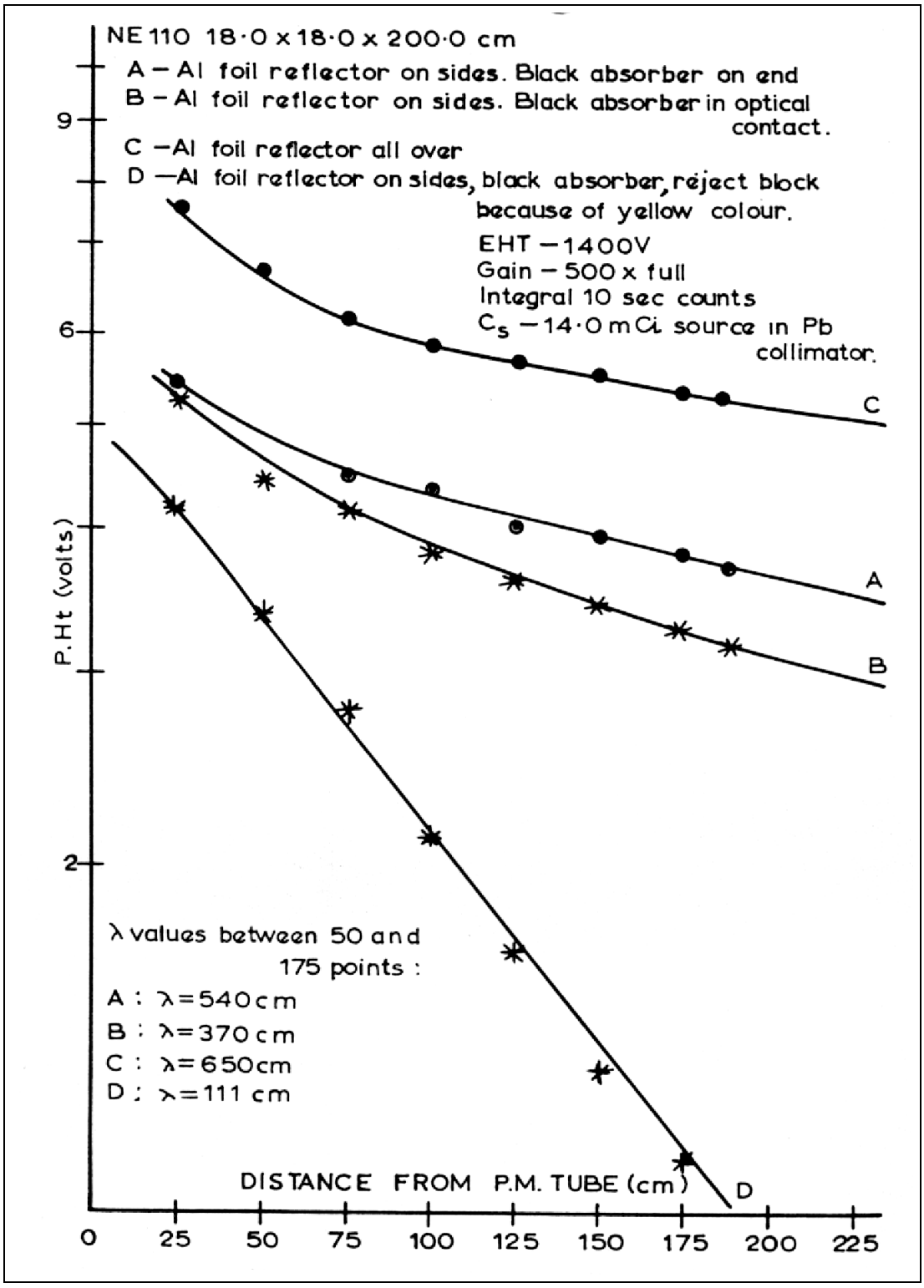

Figure 3.4. Measured attenuation lengths of a bulk plastic scintillator (BC412; $18\times18\times200\text{cm}^{3}$) for various configurations [Nicoll71]. Shown are the pulse heights of the output signals in volts versus the distance between source and PMT in centimeters. The various settings are described in the figure text.

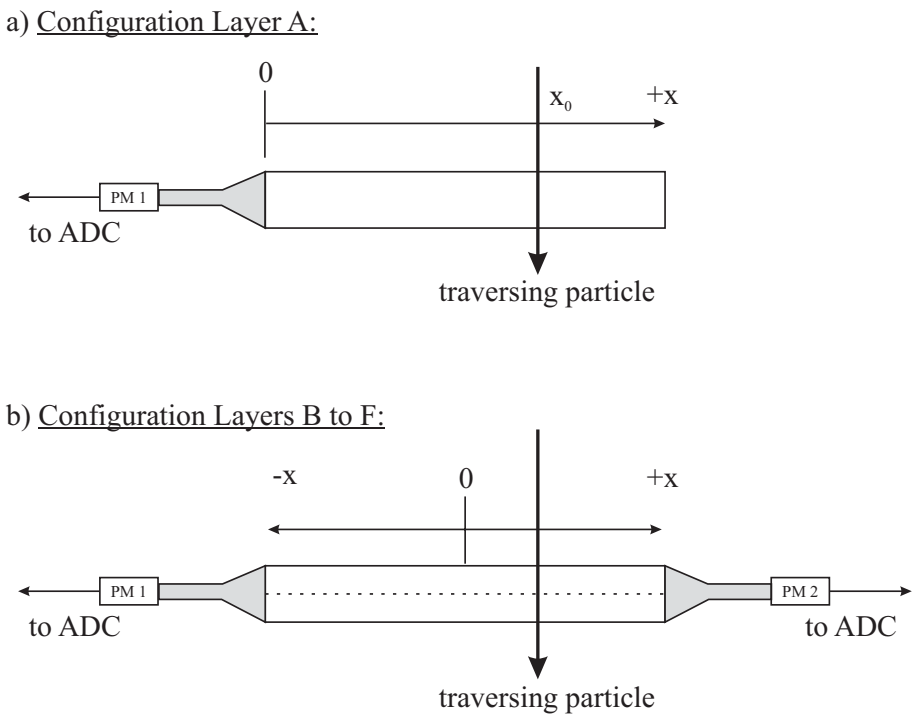

Figure 3.5. Setup for the measurement of the effective attenuation lengths of DAPHNE's scintillators. a) Layer A, b) Layers B through F.

which takes not only the exponential attenuation of direct light, but also a component due to reflection from the opposite end of the scintillator into account:

$$P(x_0) = \frac{1}{2} P^0 \left\{ \exp\left(\frac{-x_0}{\lambda}\right) + \exp\left(\frac{-(2L - x_0)}{\lambda}\right) \right\}. \tag{3.8}$$

If the impact points of the traversing particles are known one can fit the above functions to the measured pulse height distribution with P^0 and λ as free parameters. The next problem that is to be discussed is the determination of the according pulse heights.

The considerations in Section 3.1 have been concerned with the *mean* energy loss of a fast particle. However, since the energy lost by a particle passing through matter is the result of a large number of independent events, the process is a statistical phenomenon, i. e. no unique value for the energy loss (and hence for the pulse height) can be obtained. On the contrary, one will find a continuous distribution of pulse heights when studying single collisions. It has been shown that the resultant energy loss distribution is negatively skewed—the high energy-loss tail being due to those collisions in which a large amount of energy is transferred to the target electron in a single encounter. In a somewhat thin absorber, the small probability of such collisions results in a relatively large random statistical variation in their number, and thus fluctuations in the total energy loss occur. Several theories predict the probability distributions of energy loss also known as *straggling functions*. Of these, those of Landau and Vavilov are probably the most comprehensive since they are not only applicable to thick absorbers where the distribution is Gaussian-like (due to the central-limit theorem), but also to thin and intermediate absorbers. For the scintillators of DAPHNE not the original Landau-Vavilov distribution was taken because

of its non-analytic form, but the following similar function with four free parameters P_1 through P_4

$$f(x) = \begin{cases} P_1 \exp\left(-\dfrac{(x-P_2)^2}{2P_3^2}\right) & \text{for } x < P_2 + P_4, \\ P_1 \exp\left(-\dfrac{(x-P_2)P_4}{2P_3^2} + \dfrac{P_4^2}{2P_3^2}\right) & \text{for } x \geq P_2 + P_4. \end{cases} \tag{3.9}$$

x is the measured pulse height (also referred to as ADC *channel*, c. f. Subsection 3.6.1), P_1 is the height of the distribution in the maximum, P_2 the position of the maximum, P_3 is the σ of the Gaussian part, and P_4 the position at which the exponential tail is appended. Figure 3.6 shows a typical straggling function as measured with an A layer detector and cosmic radiation. The position of the maximum, i. e. the most probable energy loss, is chosen as pulse height for the attenuation length determination. With this, the only problem left is the determination of the impact points of the traversing particles.

Three different procedures were applied to this end:

1. To produce scintillation light at very well defined positions every ten centimeters along the scintillator bar, a collimated Sr90 source is placed on top of the scintillator and the pulse height distribution was measured. Unfortunately, this method does not provide a very precise illumination of the scintillator due to the continuous energy distribution of the low energetic electrons from the source, though it allows very accurate positioning.

2. To establish measurements using cosmic radiation, two additional small plastic counters (*paddles*, $60 \times 60 \times 2$ mm^3 of active volume) are mounted above and below the scintillator bar to be investigated and read out in coincidence, c. f. Figure 3.7. Hence the uncertainty in the position of the entering cosmic particle is limited by the paddle width. The paddles are mounted to form a mechanical unit that can be moved along a rail parallel to the x-axis. A comparison between the results for the attenuation lengths using this setup and the results with the setup described under point (1) shows that it is sufficient to use a coincidence of PMT 1 and 2 and one of the paddle detectors. Using a coincidence of the two paddles with PMTs 1 and 2 running freely increases the time consumption of a total scan by a factor of approximately three without a significant increase in accuracy. However, this latter setup is used to determine the effective velocity of light in the scintillator material, c_{eff}, which quantity is necessary for the method of point (3) to be described below. The result of such a measurement is shown in Figure 3.8. With this, the effective velocity of light has been determined to be

$$c_{\text{eff}} = (17 \pm 4)\ \text{cm/ns} = 0.57 \cdot c_{\text{vacuum}}. \tag{3.10}$$

   The value one expects from the refraction index of the plastic of $n_{\text{BC-412}} = 1.58$ would result in $c_{\text{eff}} = 0.63 \cdot c_{\text{vacuum}}$. The discrepancy is due to a longer effective distance the light travels because of multiple reflections in the scintillator.

3. The fastest method utilizes the time information from PMTs 1 and 2 without additional counters. PMT 1 gives the start for the readout while the signal from PMT 2 stops a clock

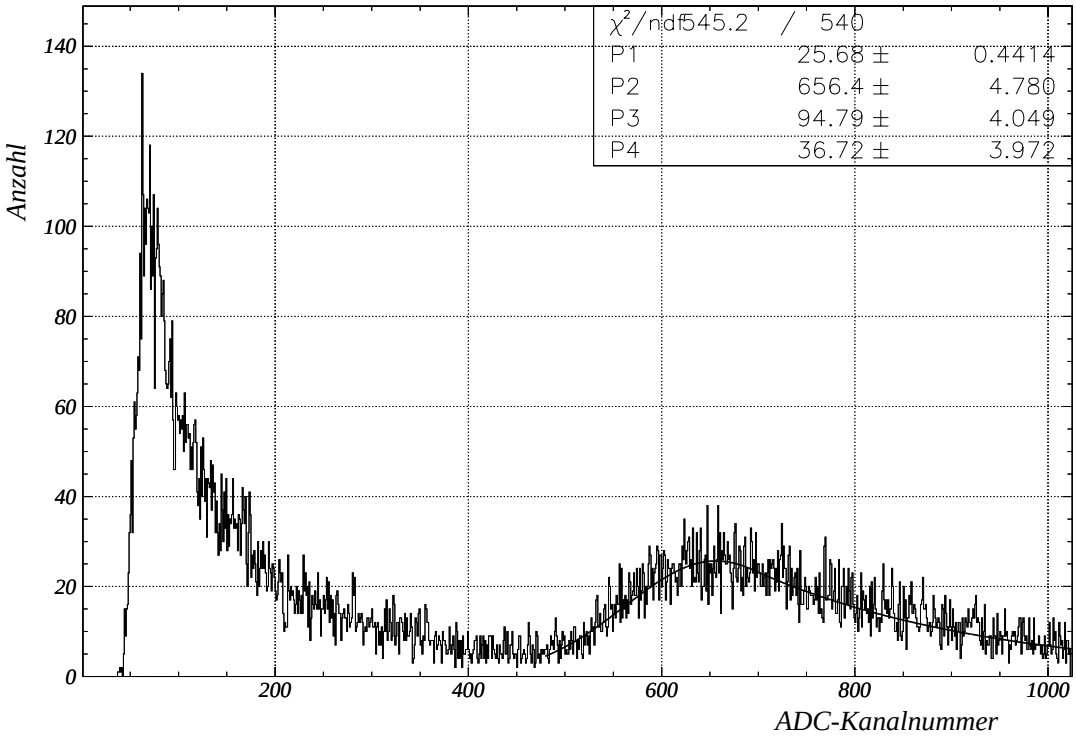

Figure 3.6. Straggling function as measured with an A layer detector using cosmic radiation. The part of the distribution below ADC channel 400 is due to noise of the PMTs. The full line is a fit to the data using Equation 3.9.

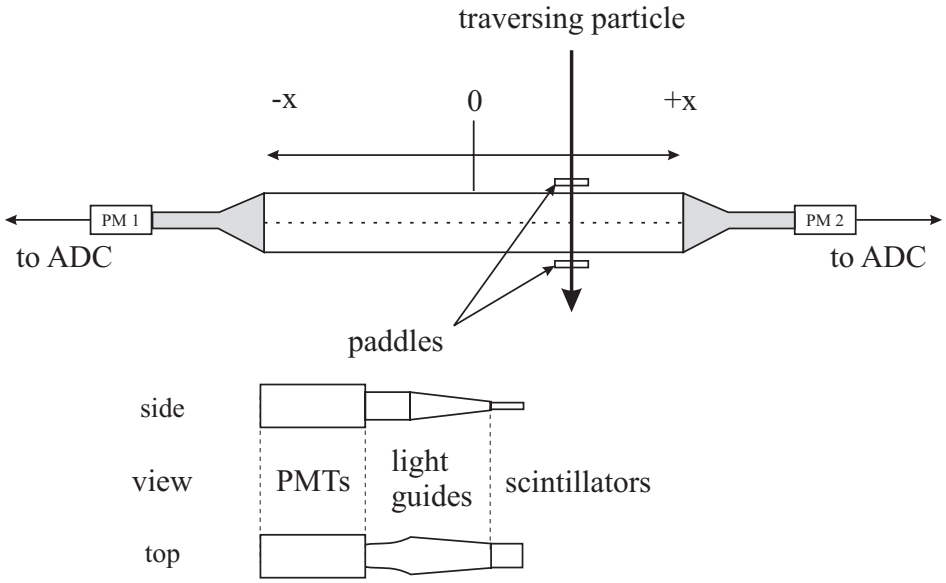

Figure 3.7. Setup for the determination of the attenuation lengths using cosmic radiation and paddle detectors.

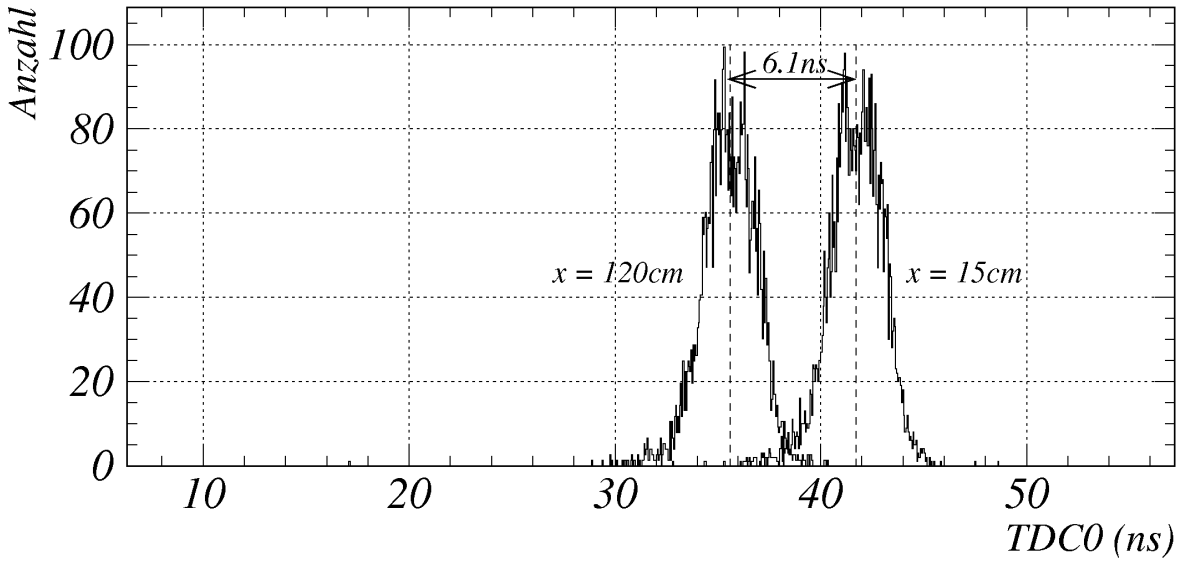

Figure 3.8. Time difference for two measurements at distances $d = 15$ cm and $d = 120$ cm from the according PMT. The space between the two distributions corresponds to 6.1 ns as indicated in the figure. From such measurements one could estimate the time resolution of the apparatus to be approximately 3 ns.

(TDC, time-to-digital converter, c. f. Subsection 3.6.1). Timing and position information are related as follows

$$t_{\mathrm{start|stop}} = c_{\mathrm{eff}}^{-1}\left(\frac{L}{2} \mp x_0 + L_l\right) + t_{\mathrm{D}}, \qquad \text{with } t_{\mathrm{D}} = \begin{cases} 42 \text{ ns for } t_{\mathrm{stop}}, \\ 0 \text{ otherwise.} \end{cases} \tag{3.11}$$

L_l is the length of the light-guides. The minus sign is valid for the start time t_{start}, the plus sign for the stop time t_{stop}. The additional delay t_{D} for the stop time is arbitrary in value but necessary to register also particles at $x < 0$. The position information can then be reconstructed using the time difference $\Delta t := t_{\mathrm{stop}} - t_{\mathrm{start}}$ by

$$x_0 = \frac{c_{\mathrm{eff}}}{2}(t_{\mathrm{D}} - \Delta t). \tag{3.12}$$

The ADC information for each PMT is then plotted versus the position of each event. The resulting two-dimensional histogram is then sliced in bins for various positions. The projections of the bins onto the ADC axis delivers the straggling functions—after a subtraction of the background due to noisy PMTs—that are needed for the determination of the attenuation lengths.

The accuracy of this latter method depends on the time resolution of the apparatus. From Figure 3.8 the time resolution can be estimated to be in the order of 3 ns (full width at half maximum). However, this value is not the intrinsic value of the apparatus used in method (3), since the geometric extension of the paddles enters the above value for the time resolution because events in a region of at least 60 mm width (the width of the paddles) are accepted. This

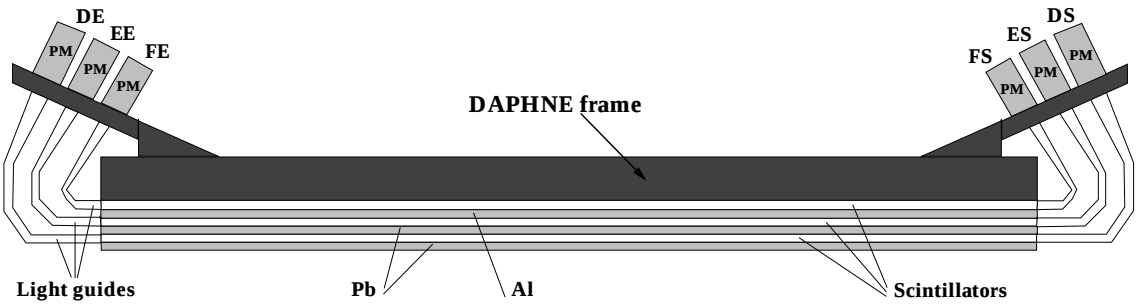

Figure 3.9. One sector of Layers D through F mounted in their frame, separated by the converter/absorber material (grey). The way these scintillators are mounted allows for the measurement of all three layers at the same time. The achieved accuracy could also be improved by requiring events that were registered in all three layers in coincidence and at the same position.

effect should be small (a width of 60 mm corresponds to a time of 0.35 ns) so one can stick to a time resolution value of approximately 3 ns resulting in a spatial resolution of approximately 50 cm or better, i. e. according to this rough estimation, only events with a minimum distance of 50 cm could be separated. The strategy to find sufficiently well defined positions for this method is to start with bins of only a few centimeters in width whose neighbors are at 20 cm distance in each direction and to try to reproduce the attenuation length that has been measured by method (2) before. The width of each bin is fine-tuned to gather sufficient statistics during one day of measuring time. It turns out that the original choice of 20 cm distance and 10 cm total bin width is sufficient to reproduce the attenuation lengths within an error of better than 10 percent, c. f. Table 3.2. Please note that one obtains systematically lower values for the attenuation lengths by the timing method than by method (2). The above procedures are reported in [Domingo00] in greater detail. As well, lists with all results for the attenuation length measurements of Layers A through C and schematics of the electronics setup can be found there.

B	$\lambda_{\mathrm{eff}}^{\mathrm{timing}}$ [cm]	$\lambda_{\mathrm{eff}}^{\mathrm{paddles}}$ [cm]
1	617 ± 15	650 ± 20
10	544 ± 20	600 ± 20
11	580 ± 30	596 ± 20

Table 3.2. Comparison of the results for the attenuation lengths of selected B layer scintillators measured with paddles and the timing method. The discrepancies between both measurements were below 10 percent. The average value for all scintillators from the timing measurements is $\bar{\lambda}_{\mathrm{eff}}^{B}$ = (607 $\pm$ 15) cm.

For Layers D to F, which arrived a few months after the other three layers, only the timing method was used. The "natural" mounting of the layers, c. f. Figure 3.9, allows one to gain additional accuracy. Since three scintillators are read out at the same time, only those events are accepted that are in the same bin in all three detectors. The increased measuring time due to the loss in statistics is balanced by the factor of three one gains by measuring three bars in parallel. Details on this work can be found in [Giménez02]. A comparison of the attenuation lengths of DAPHNE from 1994 with our results is given in Table 3.3.

After the detector had been reassembled and with the refurbished wire chambers in place again, the standard method for the determination of the attenuation lengths, as described in [Lang96] and [Windisch02], could be used. Table 3.3 also shows the results of these mea-

	1994	2000/2001	Improvement $\Delta\bar{\lambda}$	2002
$\bar{\lambda}_A$ [mm]	1140 ± 40	1550 ± 40	+410 ± 60 (+36%)	1652 ± 95
$\bar{\lambda}_B$ [mm]	1020 ± 30	6070 ± 60	+5050 ± 70 (+500%)	5214 ± 1113
$\bar{\lambda}_C$ [mm]	472 ± 6	1600 ± 50	+1130 ± 50 (+240%)	1575 ± 244
$\bar{\lambda}_D$ [mm]	644 ± 14	1250 ± 30	+610 ± 30 (+94%)	1646 ± 830
$\bar{\lambda}_E$ [mm]	760 ± 30	1220 ± 40	+460 ± 50 (+61%)	1364 ± 520
$\bar{\lambda}_F$ [mm]	650 ± 11	1480 ± 30	+830 ± 30 (+130%)	1784 ± 530

Table 3.3. Comparison between 'old' (1994) and 'new' (2000/2001) effective attenuation lengths for the scintillator layers in DAPHNE. Also shown are the first results with the refurbished wire chambers from 2002 [Windisch02].

surements in 2002. It is clearly visible that a tremendous increase in the attenuation lengths has been achieved, especially for the B layer where the old values are exceeded by a factor of five. These measurements were done without all parameters finally determined that compensate for mechanical misalignment of the chamber components, and with a readout electronic whose trigger logic had been slightly altered with reference to the 1997/1998 GDH experiment. The work on the electronics will be the topic of the rest of this chapter.

3.6 DAPHNE's Readout Electronics

The second part of the work that was done in the course of this thesis is the revival of the readout electronics and its adaptation to the requirements of the 2003 nGDH measurement. The DAPHNE sub-trigger conditions were altered to cope with this. In addition, the VME computer that reads the QDC, TDC, and scaler information and transfers these data to a workstation where they are saved on a storage medium, was replaced with a faster machine that allows a twice-as-high readout rate at doubled photon beam intensity compared to the 1997 GDH experiment. The rest of the readout electronics was—apart from necessary repairs and replacements—left the way it has been described in [Lang04], Chapter 4. Also see this reference for a detailed description of the 1997/98 electronics setup which was in operation for the data that have been analyzed for this thesis, c. f. Chapters 4 and 5. But before going into details about the DAPHNE electronics a little introduction will follow to explain the function of the key electronic modules that are used in the DAPHNE setup.

3.6.1 QDC, TDC & Co.

ADC/QDC. The main function of an ADC/QDC module is the conversion of the value of an analog quantity into a digital number that can be processed by a readout computer. In nuclear physics, an ADC may be of two types: 1) peak-sensing, or 2) charge sensitive. In the latter case the device is referred to as QDC. An ADC of type (1) transfers the maximum of a voltage signal, while a QDC converts the total integrated current of the applied signal. This is usually

the case when a fast PMT signal is to be treated. The integration time of the QDC is given by a gate signal that has to be applied from an external source and has to be adjusted in such a way as to cover the PMT signal under investigation. A review of the most common techniques to electronically realize an ADC has been given in [Henry73]. The simplest method uses the input signal to charge a capacitor. The discharge is carried out at a constant rate, and a scaler (see below) is fed with the signals of an oscillator during the discharge time. The number of counted oscillations is proportional to the charge of the input pulse. This method is known as the *Wilkinson method*.

Discriminator. A discriminator module translates analog input signals to logic signals of an adjustable duration and specified constant amplitude. The input signal has to exceed a certain—adjustable as well—threshold value to create an output signal. Otherwise, no response is made. Since discriminators are usually used to create time-critical logic signals that start and stop precise clocks, it is essential that the time relation between the arrival of the input pulse and the issuance of the output pulse be constant. In *leading edge discriminators* the output signal is created the moment the pulse crosses the threshold level. For pulses with a large variation in amplitude this timing is not constant (*time-walk*). A more precise method is *constant fraction discrimination* where the logic signal is generated at a constant fraction of the peak height. The result is an essentially walk-free output signal. The only requirement for the input pulses is identical rise time which is usually fulfilled for PMT signals. Details about this discrimination technique can be found e. g. in a current issue of [Leo87].

Register (Latch). These modules with several parallel inputs record the pattern of input pulses. Usually an additional gate signal is required to start the process of the input (*coincidence* registers). *Output* registers possess additional outputs for logic signals. The latches used in the tagger just loop through the input to the output while a gate signal is present.

Scaler. A scaler module counts the number of logic signals fed in and presents the result as a digital number. Via gate or inhibit inputs these modules can be kept from counting for certain times which is useful for e. g. dead-time measurements.

TDC. The function of a TDC module is generally that of a clock that can determine time intervals very precisely. To this end, a start signal is necessary to start the internal scaler that counts the internal oscillator or clock until a stop signal is applied. The TDCs in DAPHNE are realized in a different way. The start/stop signals are fed into a time-to-amplitude converter that creates an analog output signal whose charge is proportional to the time difference between the start and the stop signal. In addition, a logic pulse is generated of the same duration as the analog output signal. These two signals are then used to feed a QDC module.

3.6.2 DAPHNE's sub-triggers

The heart of a modern detector in medium and high-energy physics is the so-called *trigger electronics.* This part of the readout electronics is meant to analyze the response of a detector

after a reaction has taken place and to decide as fast as possible whether to read the information provided by the detector and save it on a storage medium or to discard the event. To achieve this, the analog information given by the detector's PMTs is translated to logic signals via *discriminators*. If a certain adjustable pulse height is exceeded by a PMT signal these modules create a defined signal on the output (usually 750 mV at 50 Ω impedance, NIM standard) of adjustable duration. Setting these thresholds carefully allows one to preselect e. g. minimum energy depositions that will enter into the trigger decision. Certain combinations of these logic signals from the various detector components can then be selected by programmable logic units to initiate the readout of the analog information itself. Together with the different detection efficiencies of the detector components and the expected reaction products and their kinematics one can define trigger conditions that favor for example charged particles in the final state. In DAPHNE, one works with four sub-triggers, C1 through C4, of which C1 and C2 are the triggers for the charged particles, while C3 and C4 are responsible for the neutral reaction channels.

Sub-triggers C1 and C2. For a fulfillment of the C1-condition, basically a signal in Layer A is required. Additionally one has either a signal from both A and BE together (analog sum) or a signal in CE and CS, i. e. in Boolean notation

$$\mathbf{C1} = A \cdot (A\,BE + CE \cdot CS). \tag{3.13}$$

The affixes E and S denote signals from the beam-entry side (E, from French "entrée") and the beam-exit side (S, French: "Sortie") respectively, c. f. Section 2.5. The first part of the OR-condition that makes use of the sum of A and BE realizes a $\Delta E/E$-like cut that eliminates most of the electromagnetic background that stops in B. Since this suppresses relativistic pions as well—which will not stop in B—such pions are registered by the second part requiring a signal from C layer. These conditions ensure a high trigger efficiency for charged pions and protons in the final state. Figure 3.10 presents a schematic diagram for the C1 sub-trigger. For high count rates are to be expected for this sub-trigger, the signal is divided by a factor of two, i. e. only every second event for which this condition is fulfilled for any of the 16 sectors generates the C1 trigger signal. The timing of this signal is dominated by the timing of the signal in the corresponding A layer scintillator.

The sub-trigger C2 is a copy of C1 with the additional requirement of *at least two sectors* (multiplicity two) having fulfilled the condition but without any division factor.

Sub-triggers C3 and C4. Figures B.1 and B.2 on pages 99 and 100 show schematics for these sub-triggers. They are meant to favor neutral events. In Boolean notation they have the conditions

$$\mathbf{C3} \;=\; \langle B\rangle_{\bar{t}} \cdot (BS + CE \cdot CS), \tag{3.14}$$

and

$$\mathbf{C4} \;=\; \langle E\rangle_{\bar{t}} \cdot (DE \cdot DS + FE \cdot FS). \tag{3.15}$$

$\langle B\rangle_{\bar{t}}$ and $\langle E\rangle_{\bar{t}}$ denote the time-averaged signal of the E and S PMTs of the respective layer. This time-average is necessary to reduce the large time fluctuations of the B layer signals due to the voluminosity of the scintillators. In addition, the timing of the B and E layer detectors is

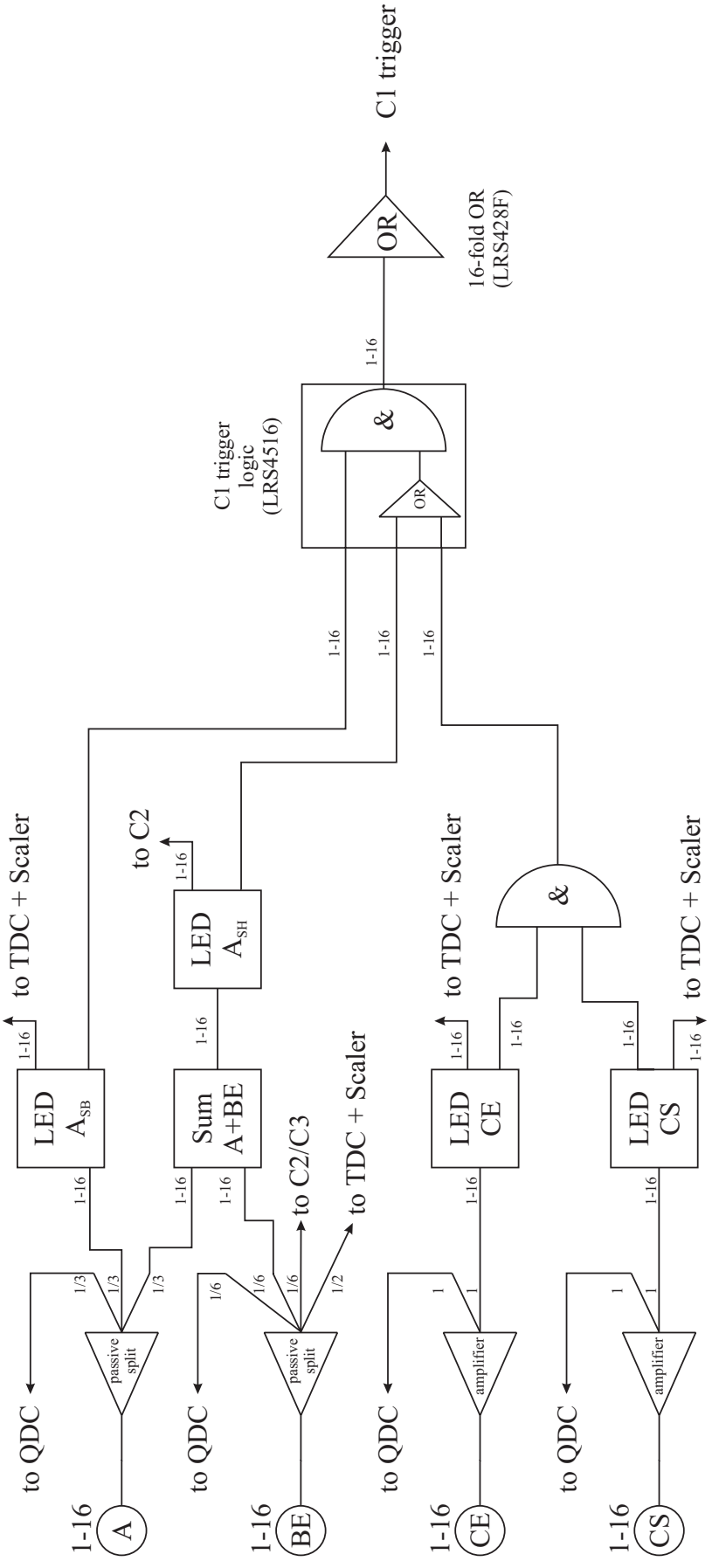

Figure 3.10. Schematic showing the DAPHNE sub-trigger C1. The trigger condition is processed for each of the 16 DAPHNE sectors individually before being merged by a 16-fold OR. The sub-trigger C2 is identical apart from the additional requirement for *at least two sectors* having fulfilled the above trigger condition.

critical since their signals are used to start the TDCs and hence a stabilization is necessary. As in the case of C2, a multiplicity of two is required, but no division takes place. A second line with this trigger was available in the configuration of 1997 where a division took place. This line is not used in the 2003 nGDH experiment.

The idea behind these trigger conditions is to have a neutron-like sub-trigger (C3) using the B layer's relatively highest neutron detection efficiency, since all other layers have a neutron detection efficiency of at least a factor ten less. The coincidence with C layer signals is meant to handle events where the neutron interacted with the B scintillator material close to the outer limit of the bar with the induced particle shower entering C layer and giving a signal there. The noise rate of CE and CS—which is increased by the amplifier—is reduced requiring a coincidence CE·CS. Neutrons interacting elsewhere in the B layer material are registered requiring a high signal in BS. Sub-trigger C4 employs the conversion efficiency of the sandwich for photons from the neutral pion decay. Again, the coincidences DE·DS and FE·FS reduce the noise rate.

In further studies C3 and C4 have not proven to be efficient for neutron and pion separation. In addition the DAPHNE setup fails to provide sufficient information on the neutron kinematics for a reliable event reconstruction. With this, C3 and C4 were relinquished as individual sub-triggers but combined in an OR-condition. Since this combination is still polluted by noise, a division factor and a multiplicity of two were required. As a result, C3C4 is used as trigger for neutral pions only.

Sub-trigger MIDAS. The MIDAS trigger is no longer accepted as a stand-alone trigger but only in combination with any other sub-trigger.

3.7 Trigger Processing and Tagger Connection

The sub-trigger signals generated by the individual detector components are fed into a 2×8 channel programmable logic unit (PLU, module from LeCroy, type LRS 4508 PLU). This unit consists of two stages, each of which processes eight input/output signals in parallel (8 bit input/output). The output in response to any input pattern can be programmed via the CAMAC bus for the two stages individually. This allows

- an easy selection of individual sub-triggers for diagnosis purposes,
- the inclusion/exclusion of the tagger and hence toggling between normal data acquisition mode in the photon beam and detector calibration mode using cosmic radiation,
- pulser generated readout which is uncorrelated to physics events for pedestal determination runs,
- photon-flux measurements in beam with the lead-glass/pair-detector triggering.

Figure 3.11 shows a schematic of the trigger electronics used for the 2003 measurements which fulfills the above requirements. The interface between the DAPHNE detector and its components on one hand side and the tagger electronics on the other hand side, is realized via six logic signals J0 to J5.

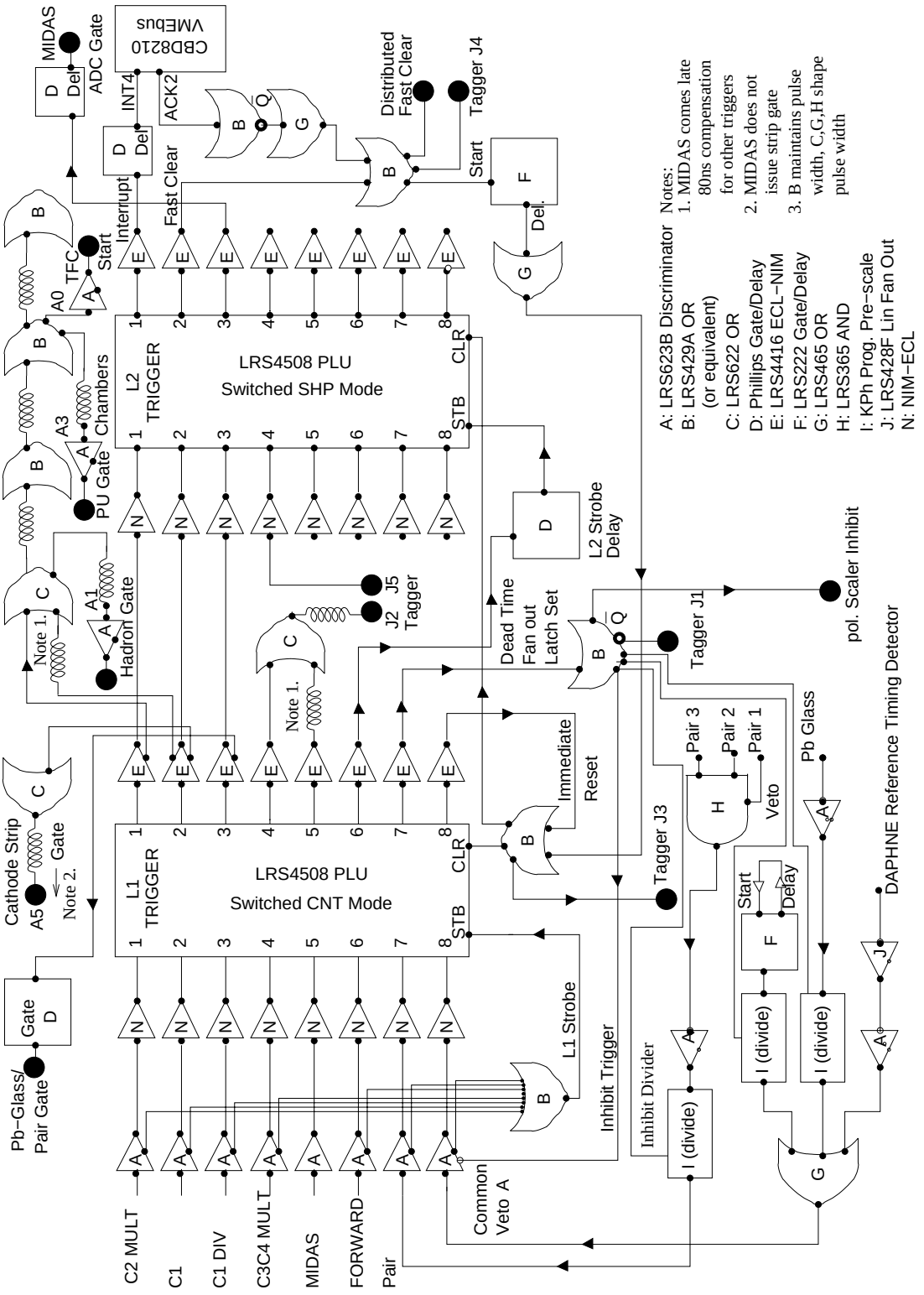

Figure 3.11. Schematic for the generation of the central GDH experiment trigger from the sub-triggers.

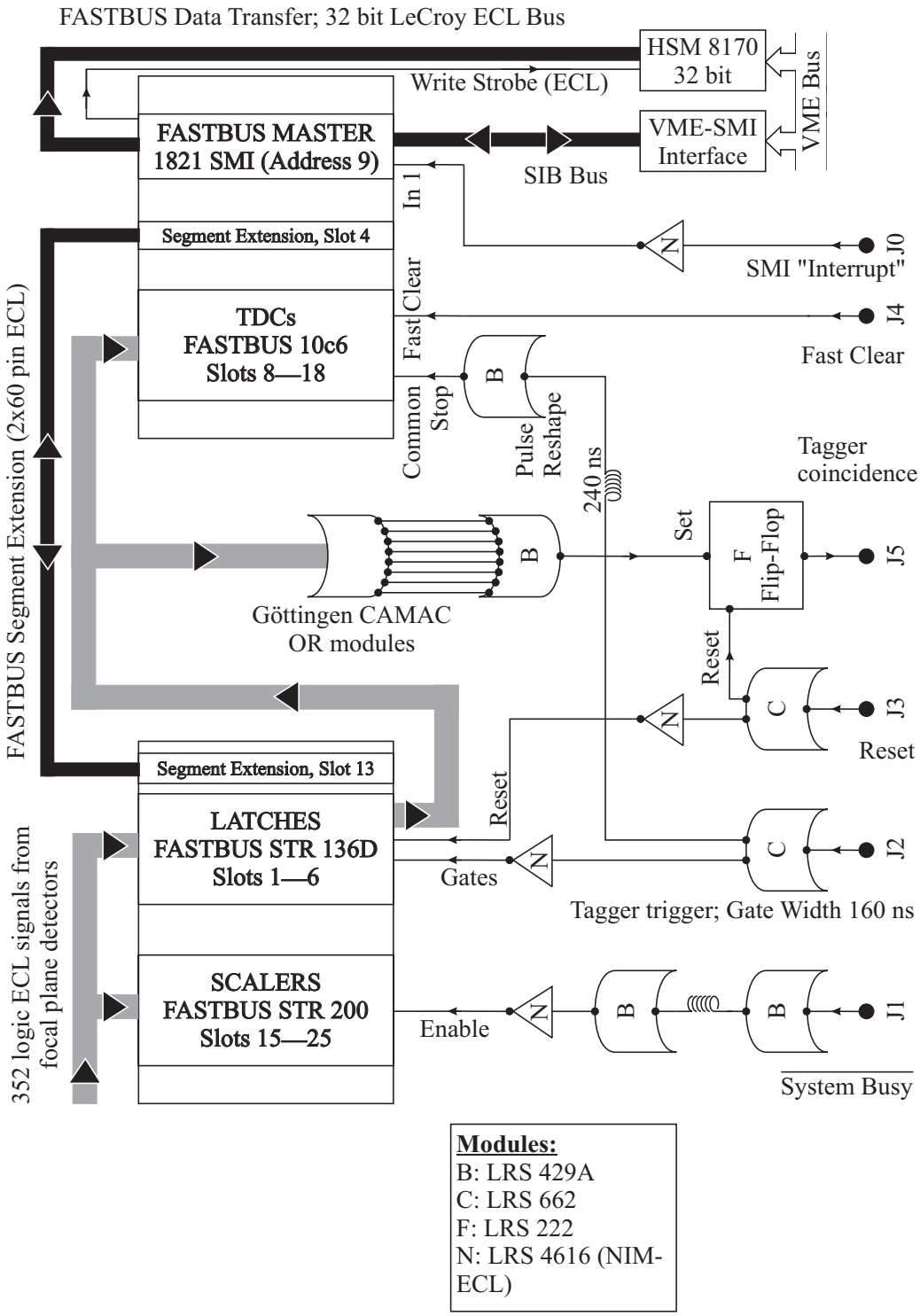

Figure 3.12. Schematic overview of the tagger electronics with the interface signals J0 to J5.

J0. This signal is necessary to enable the fast data transfer from the tagger fastbus modules (TDCs, scalers) to a high-speed memory module (HSM).

J1 is an inverted system-busy signal fed to the enable input of the tagger scalers. It allows operation of the scalers while the readout system is idle, and blocks them during readout of the acquired data.

J2 is also named *experiment trigger* or in short, *X-trigger*, since it initiates the coincidence inquiry of the tagger electronics. It is issued after a pattern of sub-trigger signals has been applied to the DAPHNE-PLU inputs that had been defined acceptable. It gates the tagger latches for a duration of 160 ns. The output signals are passed to the tagger TDC modules to start the clocks. With a certain fixed delay added, J2 gives the common stop for the tagger TDCs. This delay is chosen long enough to not discard any "good" signals, i. e. signals that originate from bremsstrahlung events.

J3 is the general reset signal for the tagger after a successful readout of the detector and tagger electronics.

J4. In case no coincident event has been registered by the tagger, this signal initiates a fast-clear of the tagger TDC modules. Any possibly running conversion in the TDC modules is stopped immediately and the modules are reset.

J5 gives the tagger answer to a coincidence inquiry. It is created from an OR of all 352 tagger channel signals that passed the latches before, i. e. that are in coincidence with particles seen in the detector. In case an OR signal exists, it sets a flip-flop whose output level goes as J5 to DAPHNE where it starts the readout of the detector modules. The flip-flop is reset by the signal J3.

Figure 3.12 shows a schematic overview of the tagger electronics.

3.8 New Forward Wall

3.8.1 Setup

Since the forward wall setup that had been used in the 1998 GDH experiment was in operation in Bonn for the measurement of the high energy part of the GDH sum rule on the proton, a new forward wall was built in Mainz to cover the polar angles below 5°. It consists of 60 modules which are made up of a hexagonal BaF_2 scintillator plus an individual PMT. These modules are very similar to those used in a common TAPS setup [Matulewicz90], except for the plastic scintillator disc used as a veto for charged particles which is missing in our setup, a smaller inner diameter of the hexagons of only 5 cm instead of 5.8 cm, and a reduced length of only 23 cm instead of 25 cm. The left part of Figure 3.13 shows a schematic of such a module. These

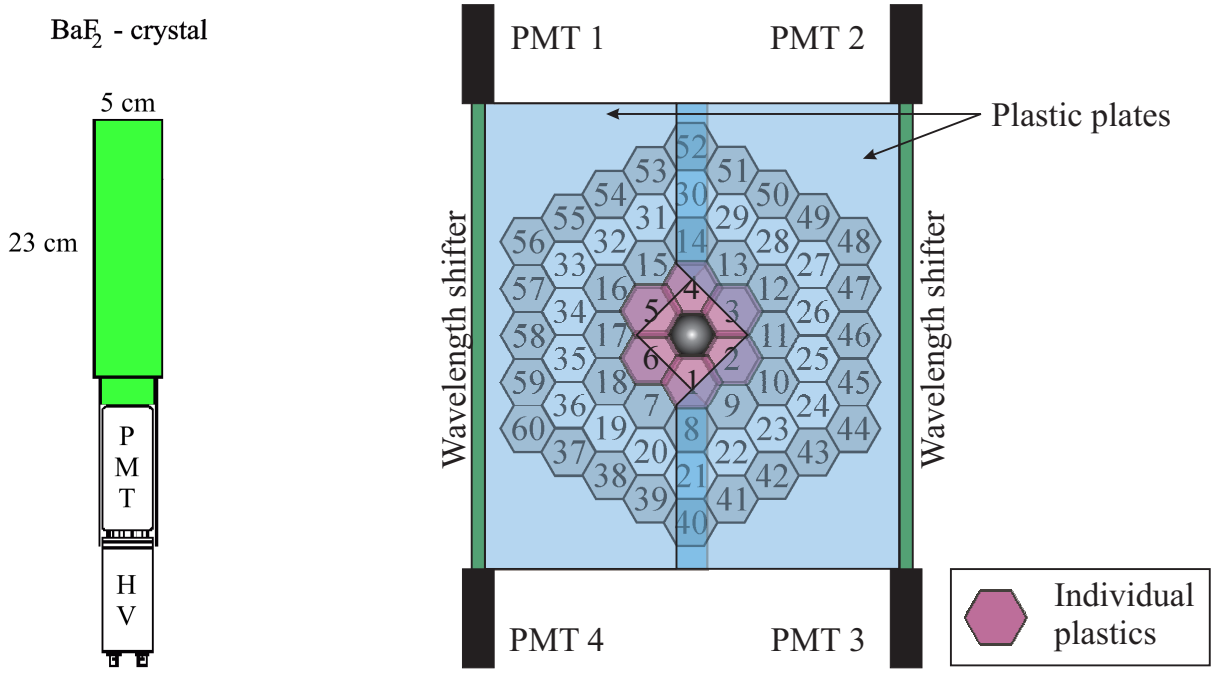

Figure 3.13. *Left:* BaF_2 scintillator module used in the forward wall. *Right:* Schematic of the setup of the 60 modules in the 2003 forward wall, view along beam axis. For details see text.

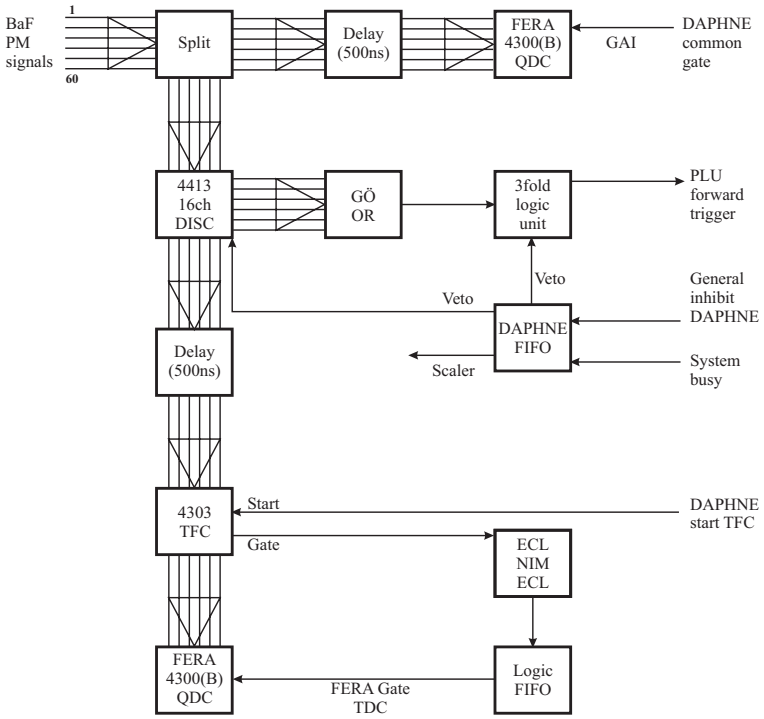

Figure 3.14. Schematic of the readout electronics for the 2003 BaF_2 forward wall. For details see text.

60 modules are arranged in such a way as to form a large hexagon of 25 cm edge length with the central module taken out for the main photon beam to pass through, c. f. Figure 3.13, right part. To allow for the distinction of charged and uncharged particles, two large plastic sheets of 5 mm thickness are placed at the beam entry side of the wall with an overlap of approximately 1 cm. Each of these sheets covers about one half of the setup. For the readout, their outer edges are optically connected to wavelength shifter bars each of which in turn is read out by two individual PMTs (labeled PMT 1 to 4). The wavelength shifter has a quadratic base area of 5 mm edge length. It absorbs the blue scintillation light of the plastic sheets and emits green light isotropically. Due to this isotropy of the emitted green light it is possible to greatly increase the light throughput to the PMTs at the ends of the wavelength shifters, c. f. Section 3.3. In the center, where the main photon beam has to pass through, a triangular part was removed from the sheets. Six individual hexagonal plastics of 5 mm thickness and 5.8 cm inner diameter are mounted in front of the innermost ring of the $\mathrm{BaF_2}$ detectors to cover the resulting quadratic hole. The whole setup is mounted on a dedicated rack that is movable on the GDH rail system in the A2 hall. The distance from the Čerenkov detector to the plastic sheets is 10 mm with the same distance between the sheets and the $\mathrm{BaF_2}$ modules.

The wall has been tested before the 2003 nGDH experiment runs in several beamtimes and has proven to be operational. For details on these tests and their results see [Klempt02]. These tests were carried out stand-alone—with a dedicated VME readout computer system. To fit the forward electronics to the DAPHNE readout the former needed to be modified.

3.8.2 Electronics

The forward electronics have been set up completely from scratch. The signals from the 60 $\mathrm{BaF_2}$ modules are split into two branches. The analog information is fed to FERA 4300(B) QDC modules while leading-edge discriminators generate two more branches of logic signals one of which is responsible for the stop of the individual FERA TFCs (= Time to FERA Converter; together with a QDC module it acts as a TDC). The second is fed to two 48-channel OR modules (Göttingen ORs) that create the forward trigger signal. All necessary gate signals for the QDCs, start signals for the TDCs, and for the control of the forward FERA chain that manages the data transfer to the readout computer are generated in the DAPHNE electronics.

3.9 Conclusions

The above described settings of both the renewed DAPHNE and the tagger have been thoroughly tested in several dedicated beam times at the end of 2002/beginning of 2003. These tests allowed to find new values for the thresholds of DAPHNE and other parameters necessary to cope with mechanical imperfections of the detector setup. Several (unpolarized) target materials have been used to obtain parameters for the detector calibration. The energy resolutions have been determined in several steps. 1) Using cosmic radiation, one determines the corrections for the mechanical imperfections of the wire chambers. 2) One can determine the reaction kinematics of the charged particles from the reactions $\gamma d \rightarrow p{+}n$ and $\gamma p \rightarrow n{+}\pi^+$ using the wire chamber information. An identification of these reactions and a separation from background at this stage of the calibration process is possible using $\Delta E/E$-plots with very generous cuts applied. 3) Since

the geometry of the detector is well known, one can calculate the energy deposited by the respective particle from the reaction kinematics and plot this value versus the ADC-information of the according scintillator. For the bars that are read out from both sides, one can use the quantity $\sqrt{\mathrm{ADC}_1 \cdot \mathrm{ADC}_2}$, where the position dependence of the ADC-values cancels and hence no correction needs to be applied. This correction is necessary for A layer only. 4) The resulting 2-dimensional plots, Figure 3.15, show a linear distribution of the registered events. A straight line fit to this distribution will give the energy calibration information. The energy resolution can be extracted when vertically slicing the 2-dimensional histograms and projecting them onto the vertical axis. The full width at half maximum of these projections is the energy resolution at the corresponding photon energy. A comparison of energy resolution values as functions of the deposited energy from 1992 (dashed line), 1997 (dash-dotted line), and 2003 (full line) is presented in Figure 3.16. As can be clearly seen, in 2003 one reached a status very close to the one of 1992 when the scintillators were new. The 1992-values for A layer were much worse because the quality of the scintillator material was substandard. The different shapes of the presented distributions for 2003 are due to an unexpected slight difference in energy resolutions for pions and protons. This effect is under investigation at this time. With this, the detector setup was ready for the final nGDH experiment in summer 2003.

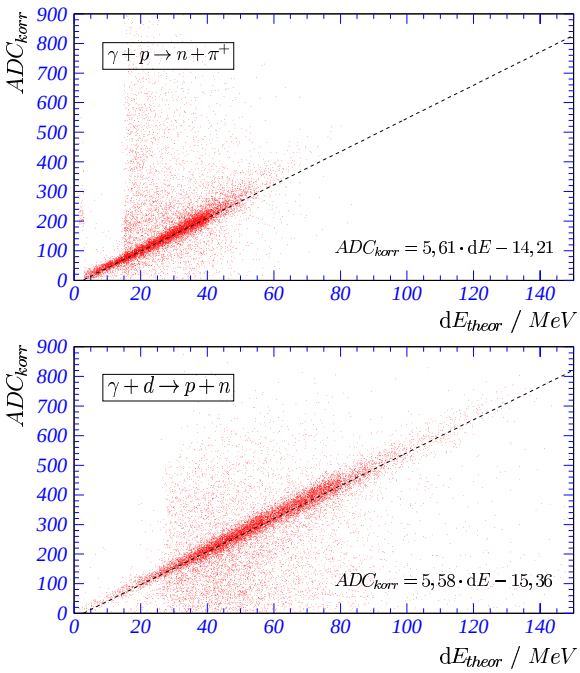

Figure 3.15. Calibration of the DAPHNE detector. Plotted are the energy depositions in ADC channels as functions of the expected energy depositions from the two-body kinematics of the two reactions that are given in the figure text. The equations in the figure give the results of the straight line fits to the data which are drawn as dashed lines as well.

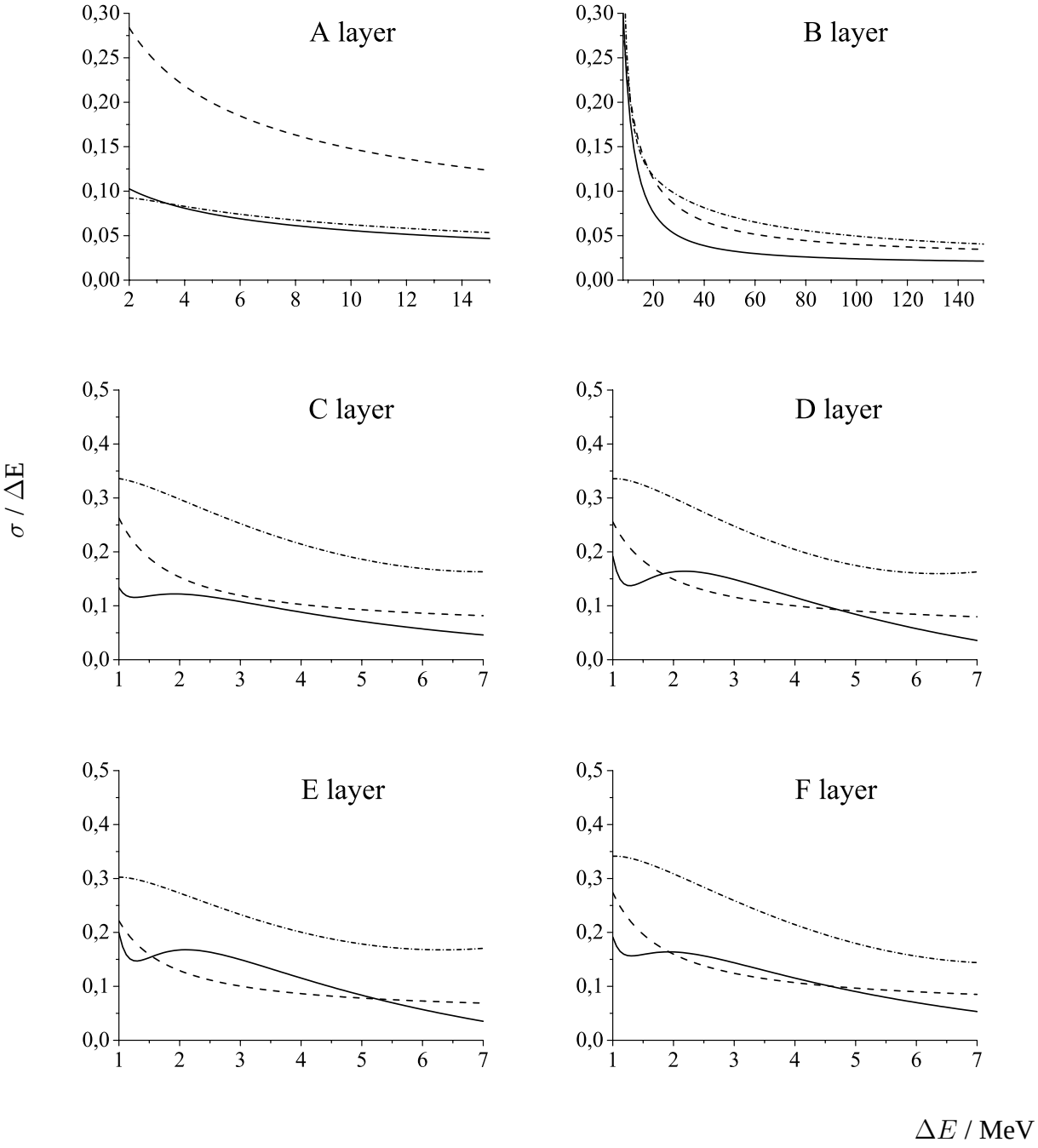

Figure 3.16. Historical survey of the energy resolutions of the DAPHNE layers in 1992 (dashed line), 1997 (dash-dotted line), and 2003 (full line). Shown is the energy deposition in the scintillator ΔE versus the relative energy resolution $\sigma/\Delta E$. The values for all sectors of a layer were averaged to give the presented curves. Their varying shapes are due to slightly different energy resolutions for pions and protons. It is clear that—except for A layer—one reached a status that is comparable to DAPHNE's original setup immediately after its first assembly in 1990. Layer A had been replaced between 1992 and 1997. Figure courtesy of P. Pedroni.

Chapter 4

Photodisintegration of the Unpolarized Deuteron for Photon Energies below 450 MeV: Analysis Procedure and Results

ONE of the most important steps when re-activating DAPHNE in 1997 after some years of inactivity was to understand the detector's response to the reaction products under investigation. Several test measurements were carried out to this end with various unpolarized target materials (liquid hydrogen, liquid deuterium, etc.) These data were not only used for calibration purposes and efficiency studies but also to reproduce known unpolarized cross sections for the reactions under study in the GDH experiment and thus to test the analysis procedures. The analysis procedure for the photodisintegration reaction of the unpolarized deuteron ($\gamma + d \longrightarrow p + n$, photon energy below $E_\gamma = 450$ MeV) will be described in the following sections. Only data recorded using the detector system DAPHNE have been analyzed. The reasons for the limitation in photon energy range will be given at the end of this chapter as well. After having delivered satisfying results—which will also be presented in this chapter—the method could be applied to data from polarized measurements with only slight modifications concerning beam and target parameters (i. e. taking the polarization observables into account and altering the target geometry settings).

4.1 Introduction

The cross section for any given photoreaction can be written as

$$\sigma(E_\gamma) = \frac{N(E_\gamma)}{L(E_\gamma)}, \tag{4.1}$$

with $N(E_\gamma)$ the number of reactions with a corresponding photon energy E_γ and $L(E_\gamma)$ the integrated luminosity of the reaction. Since a real detector setup always has a detection efficiency below unity, the number of reactions and the number of detected reactions are related as

$$N(E_\gamma) = \frac{N_{\mathrm{det}}(E_\gamma)}{\varepsilon_{\mathrm{det}}(E_\gamma)}, \tag{4.2}$$

where $N_{\mathrm{det}}(E_\gamma)$ is the number of detected reactions and $\varepsilon_{\mathrm{det}}(E_\gamma)$ the detection efficiency of the setup. The luminosity reads

$$L(E_\gamma) = N_\gamma(E_\gamma) \cdot N_{\mathrm{target}} \cdot d_{\mathrm{target}}. \tag{4.3}$$

$N_\gamma(E_\gamma)$ is the number of photons irradiating a target of thickness d_{target} with $N_{\mathrm{target}} = \varrho\frac{N_A}{A}$ target nuclei per unit volume. ϱ is the target material's density, N_A Avogadro's number, and A the mass number of the target nuclei. For liquid hydrogen the density is $\varrho = 0.169$ g cm^{-3}, the atomic weight is $A = 2.014$ g mol^{-1}, and hence $N_{\mathrm{target}} = 2.05 \cdot 10^{23}$ cm^{-3}.

Following the procedure described in Section 2.2, the number of photons can be evaluated to be $N_\gamma(E_\gamma) = \frac{N_{\mathrm{pair}}(E_\gamma)}{\varepsilon_{\mathrm{pair}}(E_\gamma)}$. With this, one yields for the total cross section

$$\sigma(E_\gamma) = \frac{N_{\mathrm{det}}(E_\gamma) \cdot \varepsilon_{\mathrm{pair}}(E_\gamma)}{N_{\mathrm{pair}}(E_\gamma) \cdot \varrho\frac{N_A}{A} \cdot d_{\mathrm{target}} \cdot \varepsilon_{\mathrm{det}}(E_\gamma)}. \tag{4.4}$$

Unfortunately, the detector system does not cover all angles, so the total cross section is not directly accessible. More convenient is the ϑ-differential cross section

$$\frac{\mathrm{d}}{\mathrm{d}\vartheta}\sigma(E_\gamma, \vartheta) = \frac{1}{2\pi(\cos\vartheta_2 - \cos\vartheta_1)} \cdot \frac{N_{\mathrm{det}}(E_\gamma) \cdot \varepsilon_{\mathrm{pair}}(E_\gamma)}{N_{\mathrm{pair}}(E_\gamma) \cdot \varrho\frac{N_A}{A} \cdot d_{\mathrm{target}} \cdot \varepsilon_{\mathrm{det}}(E_\gamma)}. \tag{4.5}$$

This differential cross section can be directly extracted from the data and compared to theoretical predictions. Calculations that were found to agree can then be used to extrapolate into uncovered angular regions to evaluate the total reaction cross section.

The practical procedure to determine the cross section for deuteron photodisintegration follows the subsequent steps:

- Calibrate the detector using data taken with an unpolarized liquid hydrogen and a liquid deuterium target.
- Determine $N_\gamma(E_\gamma)$ as described above (Section 2.2).
- Apply general geometrical cuts to ensure all events originate from the target material only. Correct for events lost by above cuts as far as possible (Subsection 4.2.1).
- Calculate the effect of the detector's and target cell's finite dimensions and correct for it (Subsection 4.2.2).
- Subtract the contribution of random events that have no proper time correlation electron-photon (Section 4.3).

- Identify the reaction, i. e. find events with only a single charged track in DAPHNE identified as proton events. The reaction kinematics are used to separate events originating from photodisintegration and other reactions with a proton in the final state (Sections 4.6 and 4.5). The neutron can only be detected with an efficiency below 20%, and even in this case DAPHNE cannot provide sufficiently precise information to reconstruct the reaction kinematics and thus unambiguously identify the photodisintegration reaction. For this reason, the neutron information was ignored.

- Compute the detection efficiency of the setup and the cuts applied, $\varepsilon_{\mathrm{det}}(E_\gamma)$, by means of simulations (Section 4.7).

- Subtract the contributions from competing reactions that are still present after the above cuts, again by simulation. For photon energies below 450 MeV this is not necessary since the contribution by neutral pion production are negligibly small.

So far the procedure is independent from the polarization observables. In the case of a polarized deuterated butanol target and polarized photon beam, it is necessary to additionally

- take the polarization information of both beam and target into account, c. f. Sections 2.3 and 2.4.

The procedure results in $N_{\mathrm{det}}(E_\gamma)$ which enters Equations 4.4 or 4.5. For presentation of the cross section and for comparison with existing theoretical predictions it is necessary to use an adequate energy binning (Section 4.4). The aforementioned steps will be described in detail in the following sections.

4.2 Cuts and Corrections

4.2.1 DAPHNE

Azimuthal Correction

Due to the segmentation of the plastic scintillator layers in DAPHNE, there are gaps in the azimuthal coverage between adjacent sectors. Moreover, particles passing close to a sector border can deposit energy in both neighboring sectors due to Coulomb multiple scattering or even miss detectors of that sector because of variations in the mechanical alignment of the plastic scintillator bars. This could confuse the offline analysis-algorithm for track classification since charged particles should produce signals in all passed layers and missing layers usually indicate neutral events. These problems are handled by defining certain azimuthal regions where no such problems occur and by rejecting all particles with trajectories outside. Figure 4.1 illustrates the situation. This approach avoids most ambiguities in track classification and enables one to calculate the fraction of particles that will be cut away (which fraction only depends on fixed geometrical parameters).

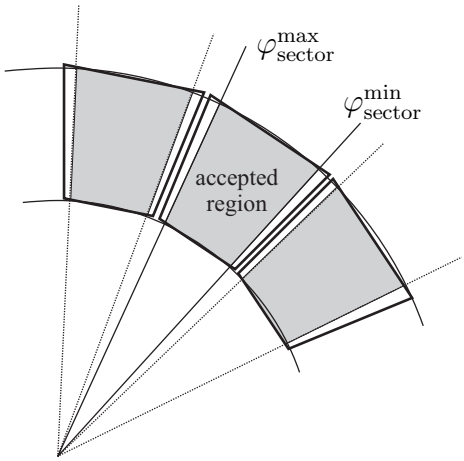

Figure 4.1. Illustration of the gaps in DAPHNE's azimuthal coverage. Shown is a cross section in xy-plane (the plane perpendicular to the photon beam axis) through three neighboring bars of DAPHNE's B layer. Only trajectories emitted into the angular regions between $\varphi^{\min}_{\text{sector}}$ and $\varphi^{\max}_{\text{sector}}$ (shaded regions, labeled *accepted region*) are accepted in the offline analysis.

The accepted φ range is determined as follows: Projecting the particle's trajectory onto a plane perpendicular to the photon beam axis and using polar coordinates, the projected trajectory has the intersection point coordinates (d, φ_d) with the hit plastic scintillator bar of any given layer. The distribution of the quantity

$$\Delta\varphi = \alpha \cdot i - \varphi_d, \tag{4.6}$$

with $\alpha = 360^\circ/16 = 22.5^\circ = \frac{1}{8}\pi$ the theoretical azimuthal width of one sector and i the sector number, can be fitted using the function

$$f(\Delta\varphi) = \begin{cases} c \cdot \exp\left(-0.5 \cdot (\Delta\varphi - \alpha_1)^2/\sigma^2\right) & \text{for } \Delta\varphi < \alpha_1, \\ c & \text{for } \alpha_1 \le \Delta\varphi \le \alpha_2, \\ c \cdot \exp\left(-0.5 \cdot (\Delta\varphi - \alpha_2)^2/\sigma^2\right) & \text{for } \Delta\varphi > \alpha_2, \end{cases} \tag{4.7}$$

with the α_i as free parameters and σ the experimental resolution in φ, see Figure 4.2. The azimuthal coverage is then given by

$$A_\varphi = \alpha_2 - \alpha_1 + 2.35\sigma \approx 0.35 \approx 20^\circ. \tag{4.8}$$

The corresponding azimuthal efficiency is evaluated using a simulation. For 1998 data the according correction factor was determined to be 1.18. This factor is a global correction and independent from φ because the cross sections under investigation are also φ-independent. For more details see [Isbert93] and [Pedroni98].

Polar Cuts

The finite length of the wire chambers and the plastic scintillators of DAPHNE implies a limited coverage in polar angle ϑ. Hence, the polar angle was subjected to the following condition

$$23^\circ < \vartheta < 158^\circ \tag{4.9}$$

to avoid marginal effects close to the light-guides of the plastic scintillator bars like in the case of the azimuthal angle and to reject trajectories that hit the MIDAS frame. A correction for the uncovered ϑ-ranges is not easily possible without the use of theoretical calculations that describe the behavior of the investigated—and in the polarized case yet completely unknown—cross sections in dependence from the polar angle.

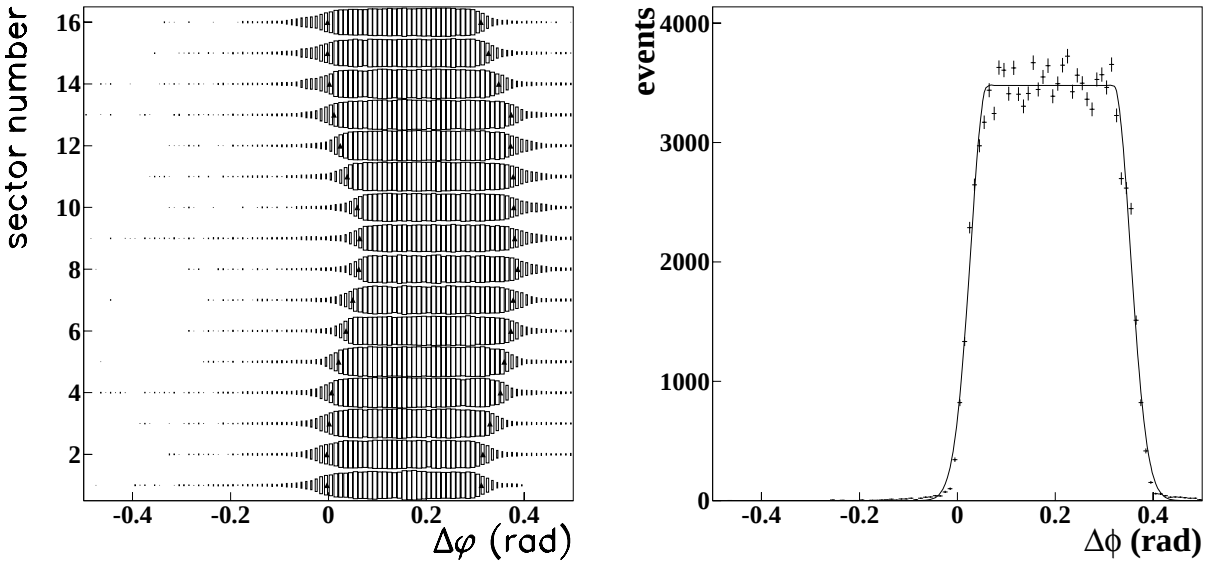

Figure 4.2. Distribution of $\Delta\varphi$ a) for all sectors (left), b) for Sector 5 (right). a): The filled triangles indicate the limits of the accepted azimuthal regions for each sector. Due to (slight) mechanical misalignments of the scintillator bars, the distributions start at non-zero $\Delta\varphi$. b) The line represents the function fitted to the $\Delta\varphi$ values according to Equation 4.7. The figures were taken from [Pedroni98].

4.2.2 Target

The selection of the events originating from only the target material can be achieved by either subtracting contributions from material around the target cell, i. e. kapton windows, copper structures, aluminum windows, etc. using empty target runs, or by applying certain conditions to the trajectories and event vertices that cut out all unwanted contributions. Since the wire chambers provide very precise and accurate data on the event geometry, the latter option was chosen. To this end there are basically two cuts that are to be applied to the data: a cut in the plane perpendicular to the photon beam axis (xy-plane), and a cut along the photon beam axis (z-axis). The cut in the xy-plane can be applied without any further implications involved and it rejects events originating from outside a cylinder along the z-axis of radius $r = \sqrt{x^2 + y^2} \leq 21.5$ mm.

The situation is slightly more complicated for the cut in z-direction. The physical limits of the target cell itself along the z-axis are

$$d^{\text{real}}_{\text{target}} = z^{\text{phys}}_{\text{max}} - z^{\text{phys}}_{\text{min}} = 43\text{ mm} - (-153\text{ mm}) = 196\text{ mm}. \tag{4.10}$$

To safely cut out the target cell windows one chooses limits on the z-axis that account for the largest error in the wire chambers' vertex-reconstruction (approximately 1.5 mm for single tracks; Section 2.5.1 on Page 33):

$$d^{\text{soft}}_{\text{target}} = z_{\text{max}} - z_{\text{min}} = 15\text{ mm} - (-115\text{ mm}) = 130\text{ mm}. \tag{4.11}$$

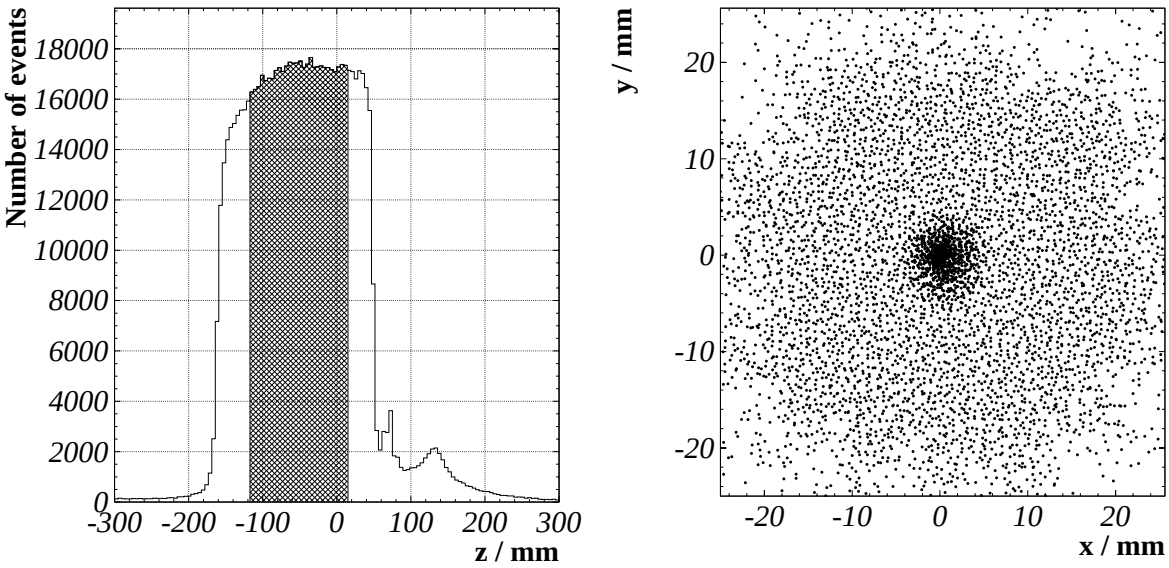

Figure 4.3. a) Event-vertex distribution along z-axis (left). Only events in the shaded region were accepted (-115 mm$\leq z \leq 15$ mm). b) Event-vertex distribution in xy-plane (right). The events accepted fulfilled the condition $\sqrt{x^2+y^2} \leq 21.5$ mm.

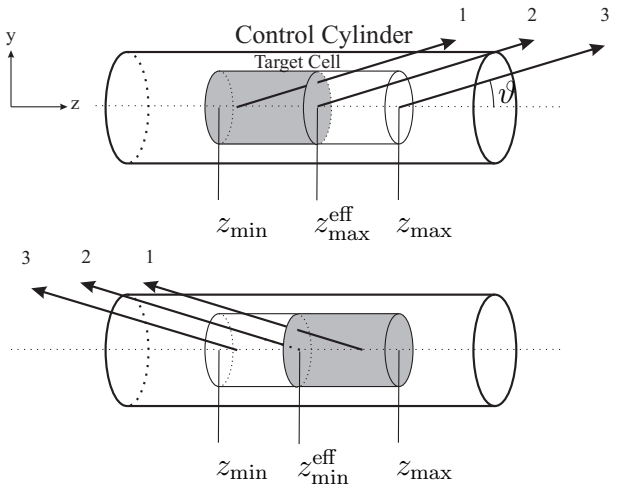

Figure 4.4. Effective target length correction. DAPHNE's angular coverage is modeled by the surface of the so-called *control cylinder.* The photon beam axis is represented by the dashed line. The two parts show the situation for particle emission in forward/backward direction.

Figure 4.3 (a) shows an example distribution of event-vertices along the z-axis. The accepted region is shaded. Close to the limits of this region one can see peaks due to events originating from target window material. Farther downstream (towards positive z-values) the MIDAS entrance window is visible.

Complications arise, since—due to the finite extensions of both target cell and plastic scintillator bars along the photon beam axis—the detection probability for certain particles with identical polar emission angles depends on the origin on the z-axis. The simplest approach to correct for this effect is modeling the angular coverage of DAPHNE by the surface of a cylinder referred to as *control cylinder* in Figure 4.4. This figure shows the situation for three single-track events that originate from different points on the z-axis. The arrows 1–3 represent the according trajectories with identical polar angle ϑ. Trajectory 1 is usually detected, while Trajectory 3 is not. Trajectory 2 is on the edge of the covered region and defines the limit of the target region $z^{\text{eff}}_{\text{min/max}}$ that is still perceived by DAPHNE (shaded region in Figure 4.4). The physical limits of the target cell are denoted z_{min} and z_{max}. If the effective target length is

$$L_{\text{eff}} = z^{\text{eff}}_{\text{max}} - z_{\text{min}} \quad \text{for } \vartheta \leq \frac{\pi}{2}, \tag{4.12}$$

$$L_{\text{eff}} = z_{\text{max}} - z^{\text{eff}}_{\text{min}} \quad \text{for } \vartheta > \frac{\pi}{2}, \tag{4.13}$$

the correction factor for each event is

$$w = \frac{L}{L_{\text{eff}}}. \tag{4.14}$$

4.3 Random Subtraction

DAPHNE and all additional detector components are driven in coincidence with the tagger to separate photon induced reactions from accidentals seen in the detector setup, c. f. Sections 3.6 and 3.7. This means that only events are accepted that appear in a certain time window around the detection of an electron in the tagger. The width of the coincidence time window is 160 ns. Photon induced events have a stable time difference since the electrons and photons travel with the speed of light and the path lengths of the electrons in the tagger and of the photons from the radiator to the target are constant. Hence, these events will appear at similar time differences in the TDC spectra producing prominent peaks. The absolute position of these peaks will vary with the tagger channel number because of slight variations in the individual path lengths of the electrons in the spectrometer magnet and of the cables that conduct the signals. To be able to easily apply time cuts, these peaks are shifted to the same position in the TDC spectra and are plotted in only one histogram. Figure 4.5 shows a typical histogram after such a shift. To correct for accidentals one defines two regions in this spectrum. Region 1 contains only accidentals in a time window comparable to the width of the coincidence peak while Region 2 contains both, accidentals and photon induced events. As can be seen from the figure, the contribution of accidentals is very constant over the whole coincidence window, so a simple subtraction of events in Region 1 from those of Region 2 corrects for the accidental contribution. To improve the statistical error of this procedure it is possible to increase the width of Region 1, taking more accidentals into account and to normalize it to the width of Region 2. However, the situation is slightly more involved for it is possible to have multiple hits in the tagger.

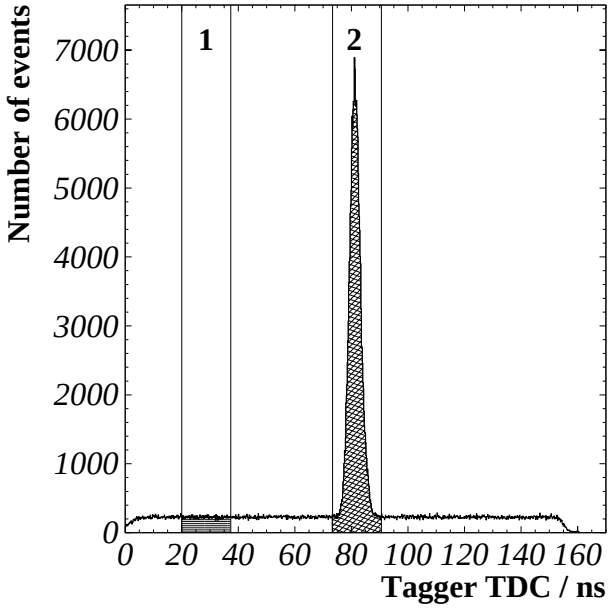

Figure 4.5. Time-difference spectrum for all tagger channels. The peak in Region 2 arises from events having a stable time-relation between DAPHNE and the tagger, i. e. events originating from photon-induced reactions. Events in the wide base are accidental coincidences. Events from Region 1 were subtracted from those of Region 2.

There are basically two sources for this:

- An electron undergoes the bremsstrahlung effect in the radiator and is counted in a tagger detector. There it is scattered and then hits an adjacent tagger detector. This effect can easily be recognized because the tagger channels involved build an uninterrupted chain. It is corrected for by only taking that tagger channel into account who corresponds with the highest photon energy, since—for geometrical reasons—the electrons are preferably scattered into tagger channels that belong to higher electron energies and hence lower photon energies, so the first hit was in the channel with the highest photon energy.
- A number of random electrons and possibly "good" electrons enter the tagger within the coincidence interval. This case can be recognized by multiple hits in non-adjacent tagger channels. Each of these events must be treated individually as described above.

It is possible, though very unlikely, that one has a combination of the two above cases, i. e. random electrons hitting adjacent tagger channels. Because of the very low probability this case was neglected.

4.4 Energy Binning

In order to present cross sections as functions of energy it is necessary to convert the tagger channels into photon energy bins. From the knowledge of the tagger magnetic field and the geometry and position of the focal plane detectors it is possible to calculate the electron energies that are covered by each tagger channel, i. e. to calibrate the tagger. From this the photon energy is known according to Equation 2.1 on page 21. The width of the energy range covered by each focal plane detector varies with the channel number so it is not possible to straightforwardly

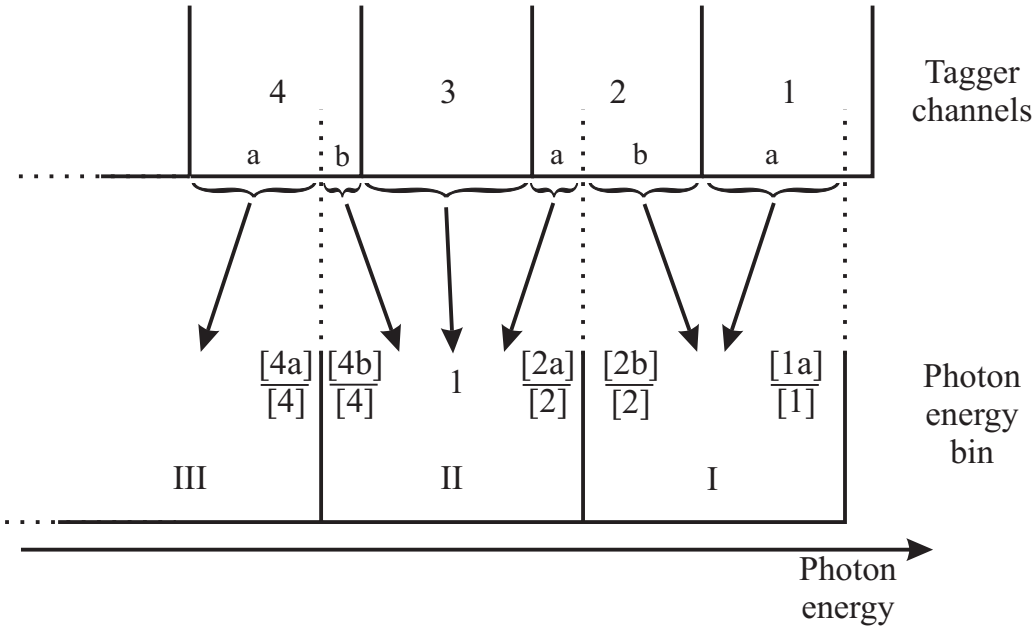

Figure 4.6. Bin-overlap method to convert tagger channels to photon energy bins. The upper scale shows the tagger channel bins while the lower scale represents the arbitrarily chosen, yet equally dimensioned photon energy bins. The arrows carry the weights given to the event in the photon energy bins. The quantities in square brackets denote the width of the labeled regions. For more details see text.

convert tagger channels to energy bins of equal size. The method that is used in this thesis to carry out this conversion is the so-called *bin-overlap method* [Holvoet00], as illustrated in Figure 4.6. This method assigns weights to each event that depend on the overlaps of the event's tagger channel with the according photon energy bins. The event is then distributed among the involved photon energy bins with the respective weighting factors. The weighting factors are given by the fractions of the tagger channel that overlap with the photon energy bin, i. e. the energy width of the overlap region is divided by the full energy width of the tagger channel. It holds that the sum of the weights equals unity for each event. All data presented in this thesis are obtained using this procedure.

4.5 Particle Identification

The first condition applied to the data when analyzing is to require only single-track events in DAPHNE that have a "good" trajectory in the wire chambers plus at least a signal from the corresponding A layer sector of DAPHNE. Problematic events due to electromagnetic background that only give a signal in the wire chambers but not in the corresponding sector of Layer A, or no signal in the wire chambers but in Layer A, are refused. With this condition, the DAPHNE detector provides sufficient information on each event to use the range-fit method—an extended version of the well known $\Delta E/E$-method. Range-fit takes a particle's energy depositions in all traversed DAPHNE layers into account allowing for clean particle identification and yields the

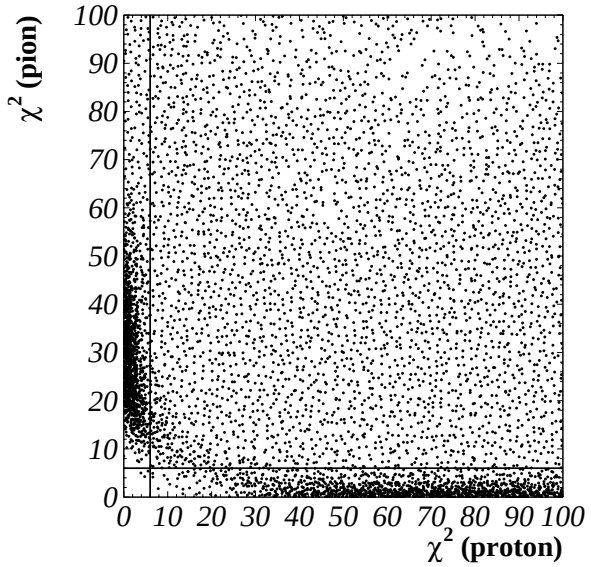

Figure 4.7. Range-fit method, $\chi^2_{\min}$ plot. The concentration of events close to the ordinate is due to protons, that close to the abscissa is due to pions.

particle's initial kinetic energy. The method has been carefully developed and thoroughly tested over the past ten years [Braghieri94, Murphy93]. It relies heavily on the integrated Bethe-Bloch formula which relates the energy loss of a particle and its path through a material. From the geometry of DAPHNE a particle's energy deposition $\Delta E^{\text{theo}}_{\text{layer}}$ can be calculated for each layer when the initial kinetic energy E_0 is known. On the other hand, taking the measured energy depositions in each passed layer $\Delta E^{\text{exp}}_{\text{layer}}$ into account, the initial kinetic energy can be obtained by the minimization of

$$\chi^2(E_0) = \frac{1}{N-1}\sum_{i=1}^{N}\frac{\left|\Delta E^{\text{theo}}_{\text{layer}}(E_0) - \Delta E^{\text{exp}}_{\text{layer}}\right|^2}{\sigma_i^2} \xrightarrow{\min} \chi^2_{\min} \tag{4.15}$$

using a least-square fit with E_0 as free parameter. N is the number of the layer the particle stops in, σ_i are the energy resolutions of the respective layers. This is a very general approach which in principle allows the identification of all charged particles that are stopped in DAPHNE. For the analysis of the GDH data in Mainz it is sufficient to tell protons from pions, i. e. once running range-fit assuming the particle is a proton and once it is a pion, since these are the only charged hadrons that can be produced at MAMI at this time. The resulting $\chi^2_{\min}$ distribution is depicted in Figure 4.7. As can easily be seen, there are two concentrations of events, one with low $\chi^2_{\min}$ for the pion hypothesis (pions) and one with low $\chi^2_{\min}$ for the proton hypothesis (protons). The lines indicate the limits applied to the $\chi^2_{\min}$ values of each hypothesis. Events with $\chi^2_{\min}$ values exceeding the limits for *both* hypotheses are totally rejected. Figure 4.8 shows the effect of the range-fit process. Plotted is the total energy deposition for particles stopping in Layer B versus the energy deposition in Layer A alone ($\Delta E/E$ plot). One can easily recognize three concentrations of events that are made up of particles of different types (electrons, pions, and protons as denoted in the figure) which are nicely separated by the procedure.

However, one has to take care of protons that scarcely enter Layer B and do not deposit much excess energy. In this case, multiple scattering of the particle plays the dominant role and may result in energy sharing between adjacent sectors of A and B layer. The range-fit process has a low identification efficiency for such particles, although one can easily identify them in

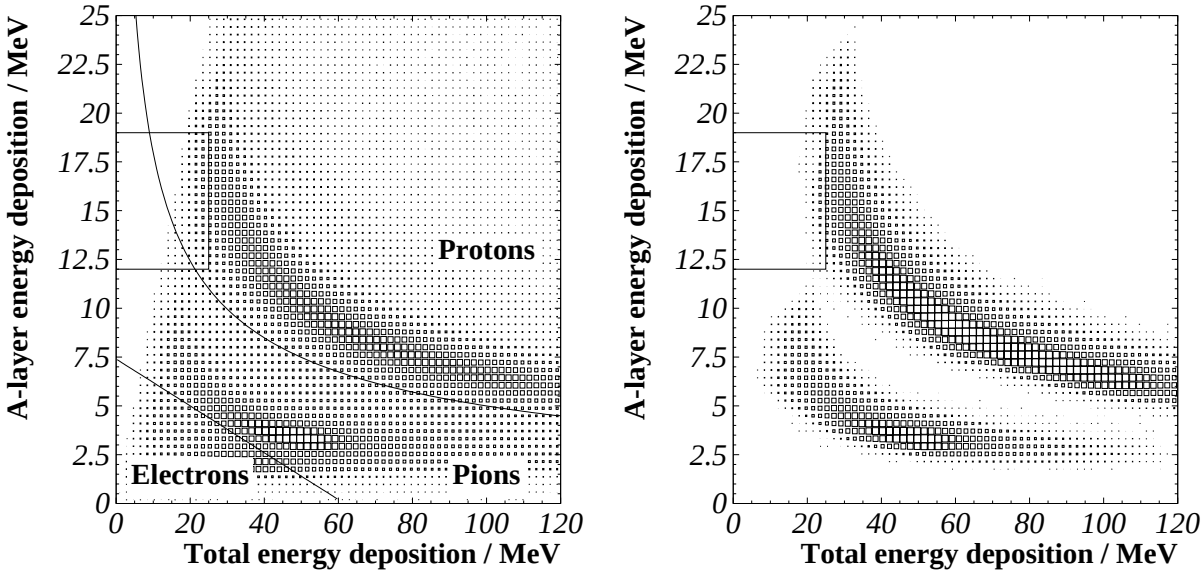

Figure 4.8. $\Delta E/E$-plot and range-fit method for particle identification. Shown is the sum of the energy depositions in A and B layer versus the energy deposition in A layer alone. The energy depositions are corrected for ϑ. *Left:* Raw events without particle identification. One can see three bands that correspond to three different particle types. The band with low energy deposition in both A and B (lower left) consists of electrons. Slightly above are pions and above this—well separated, with relatively higher energy depositions in A and B—one can find the proton events. Even without applying the range-fit method it would be possible to identify most of the particles and to separate them using the cuts that are represented by the lines added to the histogram. Merely electrons and pions with total energy depositions above 50 MeV can hardly be distinguished in this plot. *Right:* Events after range-fit procedure. The upper band consists of events identified as protons, the lower band is made of pion events. The box indicates a region of reduced identification efficiency. All events in this box are assumed to be protons.

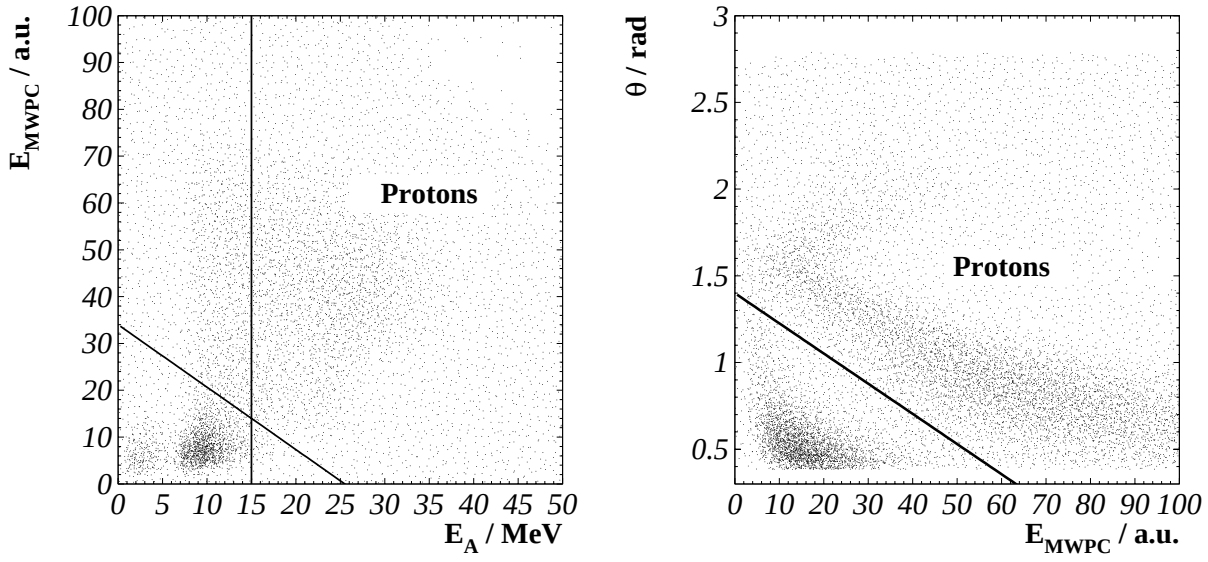

Figure 4.9. Particle identification, Stop-A particles. *Left:* Energy deposition in Layer A E_{A} in MeV versus path length corrected energy deposition in the wire chambers E_{MWPC} in arbitrary units. In the lower left are some event concentrations of electrons and pions which are indistinguishable but can be separated from the protons that are located in the upper right of the plot. The lines represent the cuts applied to the data. *Right:* Path length corrected energy deposition in the wire chambers versus polar angle ϑ. Again, the line represents the cut applied to the data.

Figure 4.8 (boxed region). For this reason, one does not rely on range-fit in this case but regards all of these particles as protons. The limits chosen for this region are

$$12\ \text{MeV} \leq \quad E_{\mathrm{A}} \quad \leq 19\ \text{MeV}, \tag{4.16}$$

$$E_{\mathrm{B}} \quad \leq 25\ \text{MeV}. \tag{4.17}$$

With range-fit it is possible to easily identify particles that stop in any layer between and including Layer B and Layer E. Particles stopping in Layer A cannot be treated using range-fit because at least two energy depositions are necessary for Equation 4.15 not to diverge. Nonetheless it is still possible to identify such particles taking the energy deposition in the wire chambers (ΔE) and in A layer (E) into account and creating a $\Delta E/E$-like plot. Yet, this identification will not be as accurate and efficient as range-fit, since the wire chambers' energy resolution is very poor compared to that of the plastic scintillators. Figure 4.9 depicts the plots that were used to this end. The cuts applied to the energy are

$$E_{\mathrm{A}} \quad > \quad 15\ \text{MeV}, \tag{4.18}$$

$$E_{\mathrm{MWPC}} \cdot \sin\vartheta \quad > \quad a_1 E_{\mathrm{A}} + b_1, \tag{4.19}$$

with

$$a_1 = -45, \quad b_1 = 1500 \qquad \text{for deuterium target,} \tag{4.20}$$

$$a_1 = -40, \quad b_1 = 1020 \qquad \text{for deuterated butanol target.} \tag{4.21}$$

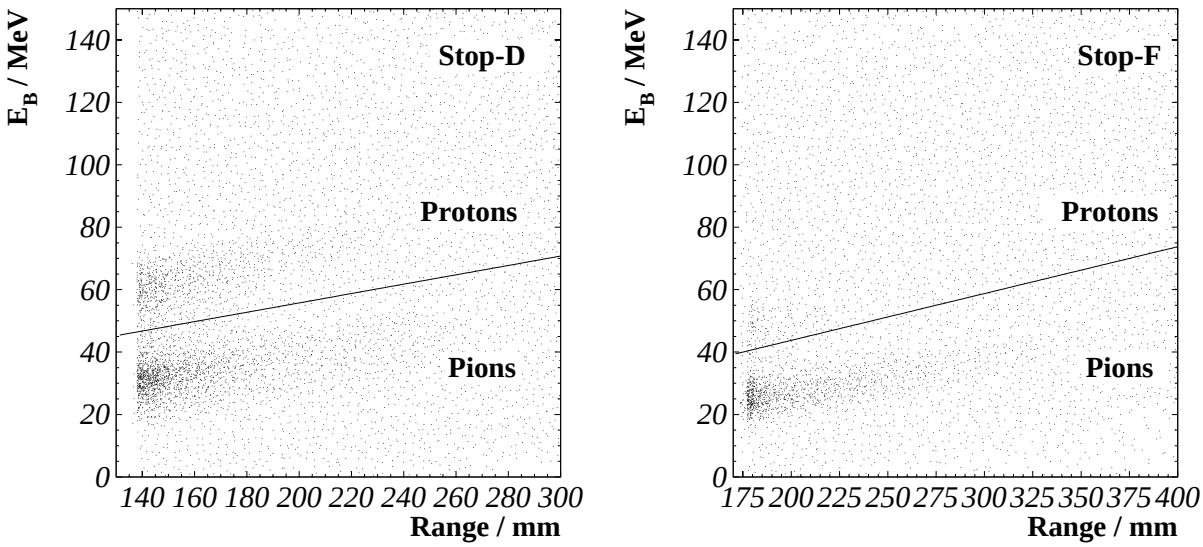

Figure 4.10. Particle identification, Stop-F particles. Plotted is the particle's minimum range in scintillator equivalent distance versus energy deposition in Layer B. *Left:* Stop-D particles. The line separates protons and pions. *Right:* Stop-F particles. The line represents the cut that was applied. As expected, most protons stop before F layer, so there is an almost negligible fraction of protons in this layer, while the portion of pions is considerable.

The cut given by Equation 4.18 is necessary to avoid complications due to the z-position dependency of the detection threshold in Layer A (remember that it is read by only one photomultiplier) at deposited energies below this limit. The other cut parameters depend also on the target setup, because at these low particle energies the influence of variations in material between target and wire chambers is quite considerable.

A problem also arises for Stop-F particles. Stop-F means that these particles reach the F layer of DAPHNE, but there is no further information available that could tell whether these particles actually stopped in F or whether they left the detector at all. There is still means for an identification when plotting the particle's minimum range R in scintillator equivalent thickness versus the energy deposition in Layer B, see Figure 4.10. One can find the protons and pions in different regions in this plot. Stop-D is also shown to present some protons for clarity, since there is almost no protons visible in Stop-F. The line in the Stop-F plot represents the applied cut which corresponds to the condition

$$E_{\mathrm{B}} > 0.15\ \mathrm{MeV/mm} \cdot R + 13.75\ \mathrm{MeV}. \tag{4.22}$$

4.6 Reaction Kinematics

Once the particle type has been determined as described in the preceeding sections and the background has been rejected as cleanly as possible, the next step in the analysis procedure is to separate the protons from photodisintegration and from competing reactions, mainly the

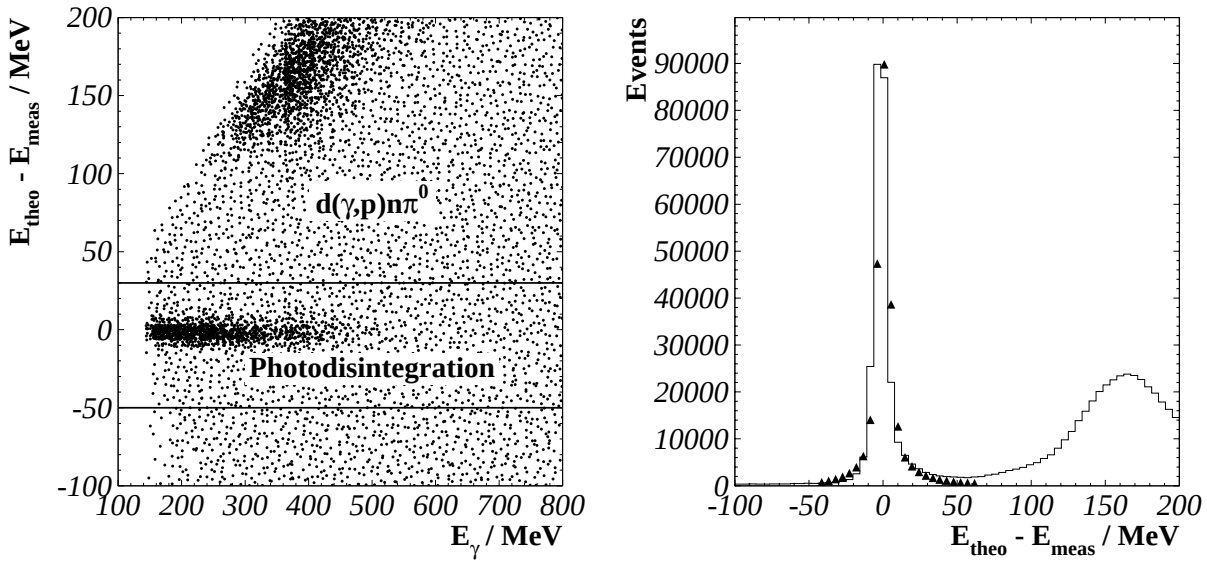

Figure 4.11. Photodisintegration, missing energy plot for deuterium target. a) Photon energy E_γ versus missing energy $E_{\mathrm{miss}} = E_{\mathrm{theo}} - E_{\mathrm{meas}}$ (left). The lines represent the cuts applied. The particles originate from $d(\gamma, p)n$ and $d(\gamma, p)n\pi^0$ as labeled in the diagram. b) Projection of the 2-dimensional plot onto the vertical axis and comparison with simulation (GEANT) represented by the filled triangles (right).

reaction

$$\gamma + d \longrightarrow p + n_{\mathrm{spectator}} + \pi^0. \tag{4.23}$$

This is achieved using the kinematical properties of the photodisintegration reaction. It can easily be calculated, since this reaction is a two body reaction. The difference of the expected and measured energy $E_{\mathrm{theo}} - E_{\mathrm{meas}}$, known as *missing energy* E_{miss}, for particles originating from the designated reaction will be around zero, while events from e. g. π^0 production will most likely appear at larger values of missing energy. Figure 4.11 shows the distribution of the aforementioned difference versus photon energy (left part) and as a one dimensional plot (right part) for deuterium target. The lines in the left part of Figure 4.11 indicate the limits of the cuts that are applied during analysis.

4.7 Cut Efficiency—Simulation

The idea of applying cuts to the data is to remove unwanted background. However, any cut will also remove some fraction of the events originating from the designated reaction. Usually the cuts are set in a way that this fraction is as small as possible, but normally they are a compromise between removing background and keeping "good" events. Hence it is necessary to know the number of "good" events that were cut away and to correct for this unwanted loss. This number can be estimated using the GEANT (GEometry ANd Tracking) package that utilizes Monte Carlo techniques to simulate reactions and interactions with detector materials. The detector and target geometry and the dimensions of its components are included in the simulation program.

The standard GEANT routines are well suited for high energy multi-hadron showers. To improve their insufficient accuracy below photon energies of a few GeV, a modification of the GEANT hadronic interaction generation was necessary [Pedroni88]. As an example, Figure 4.11 b) shows the simulated missing energy distribution of photodisintegration events with all cuts that were also applied to the experiment data (filled triangles) compared to the analysis result.

4.8 Calibration Results and Error Discussion

The results obtained from the runs with unpolarized liquid deuterium target in the photon energy range between 180 and 460 MeV are represented by the open circles in Figures 4.12 and 4.13. Only differential cross sections as a function of the proton's polar angle in cms are shown and are confronted with results of [Crawford96] (filled triangles) and [Arends84] (open squares). The Crawford measurement was carried out using the DAPHNE detector and the same target that was used for the current work. Apart from some minor deviations especially at 360 MeV and 440 MeV photon energy, the otherwise good agreement of all three measurements shows that the detector is sufficiently well understood to extract the cross section information on the desired reaction and that one can proceed to analyze the data from the doubly polarized experiment. The calculations by M. Schwamb for the unpolarized differential cross sections [Schwamb03] are represented by the full lines.

The photon energy range that is covered by the data is limited at its lower end by the minimum required kinetic energy of the protons to be detected in the A layer of DAPHNE. The upper energy limit is evident from Figure 4.11 b), since—using the cuts presented in the previous section—one spuriously accepts events from the incoherent π^0-production reaction. Although this fraction is rather small, its relative importance increases with energy. At photon energies above 450 MeV it can no longer be neglected, c. f. Figure 4.13. While the data points from this experiment are safely below the data from [Crawford96] for energies below 450 MeV, they overshoot these data for higher photon energies. This background cannot be removed without a significant effort in establishing an accurate simulation program. Another problem in this context is the decrease in event statistics due to the $1/E_\gamma$ behavior of the bremsstrahlung cross section, c. f. Section 2.2. The error bars increasing with the energy in Figures 4.12 and 4.13 reflect this fact. The lack in statistics is even worse in the case of the doubly polarized experiment with roughly 150 hours duration, so it was decided to refrain from subtracting the contribution of the π^0-production reaction and only deal with the photon energy range below 450 MeV. The fact that the data from this work are systematically slightly below the Crawford data was not considered critical because the comparison of results from several measurements in [Crawford96]—among them the data from [Arends84]—seems to indicate that the Crawford data have the tendency to slightly overshoot the results of the other measurements. The calculations of M. Schwamb reproduce the data quite fine, although below and above the Δ-region they underestimate the cross section. But even in these cases the shapes are well described.

The systematic uncertainties include the error in the photon flux determination of about two percent and the above mentioned contribution from the incoherent π^0-production. The latter contribution has been estimated to stay below 10 percent for all photon energies. The total error is hence still dominated by the statistical error which reaches approximately 25 percent at 460 MeV photon energy. All other errors are negligibly small.

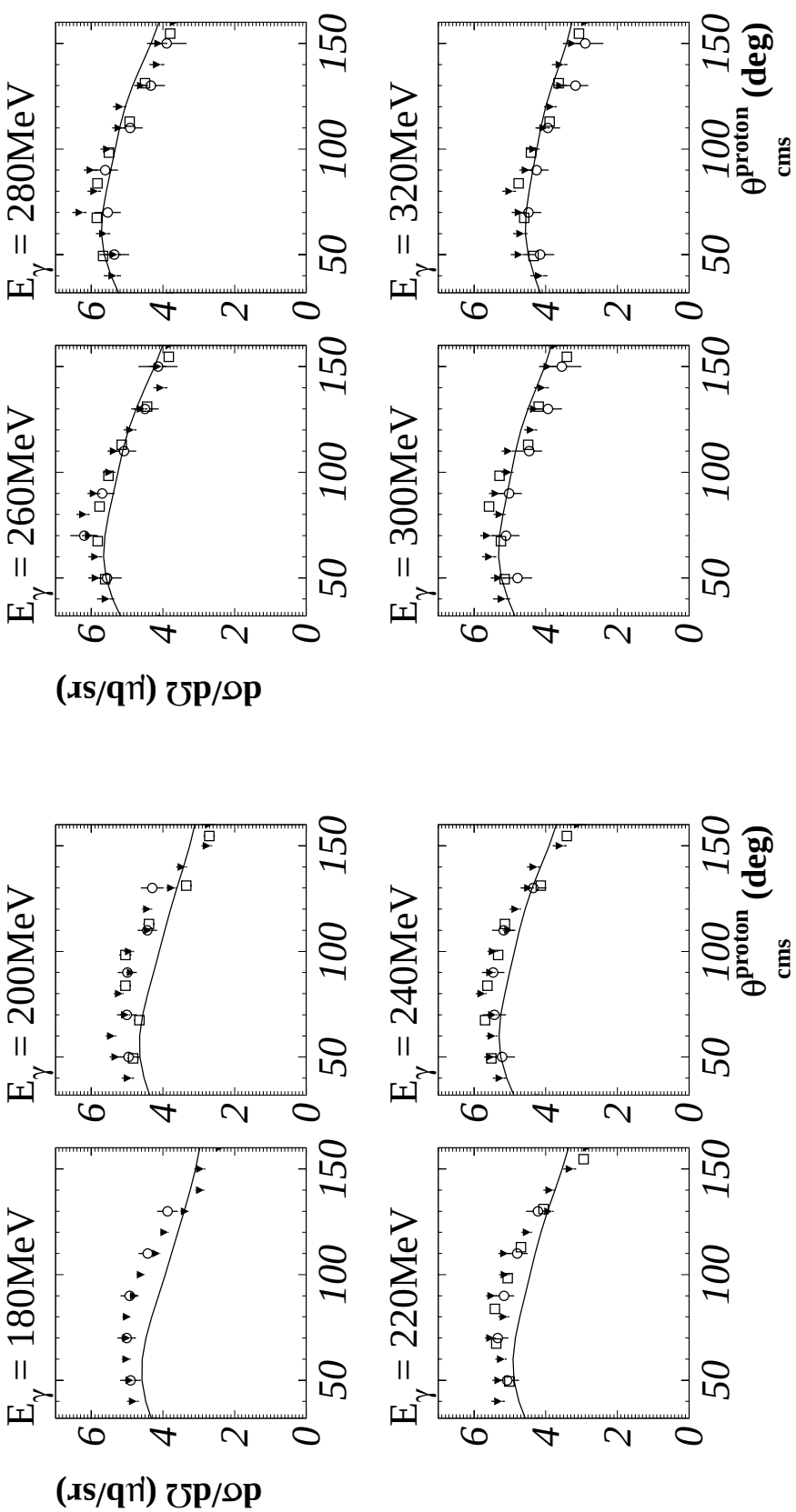

Figure 4.12. Differential cross section for deuteron photodisintegration versus polar angle of the proton in center-of-mass frame for photon energies E_γ between 180 and 320 MeV. Each energy bin is 20 MeV wide. The results from this work are represented by open circles. Measurements from [Crawford96] (filled triangles) and [Arends84] (open squares) are given as well. The line represents calculations by M. Schwamb [Schwamb03]. Only statistical errors are plotted.

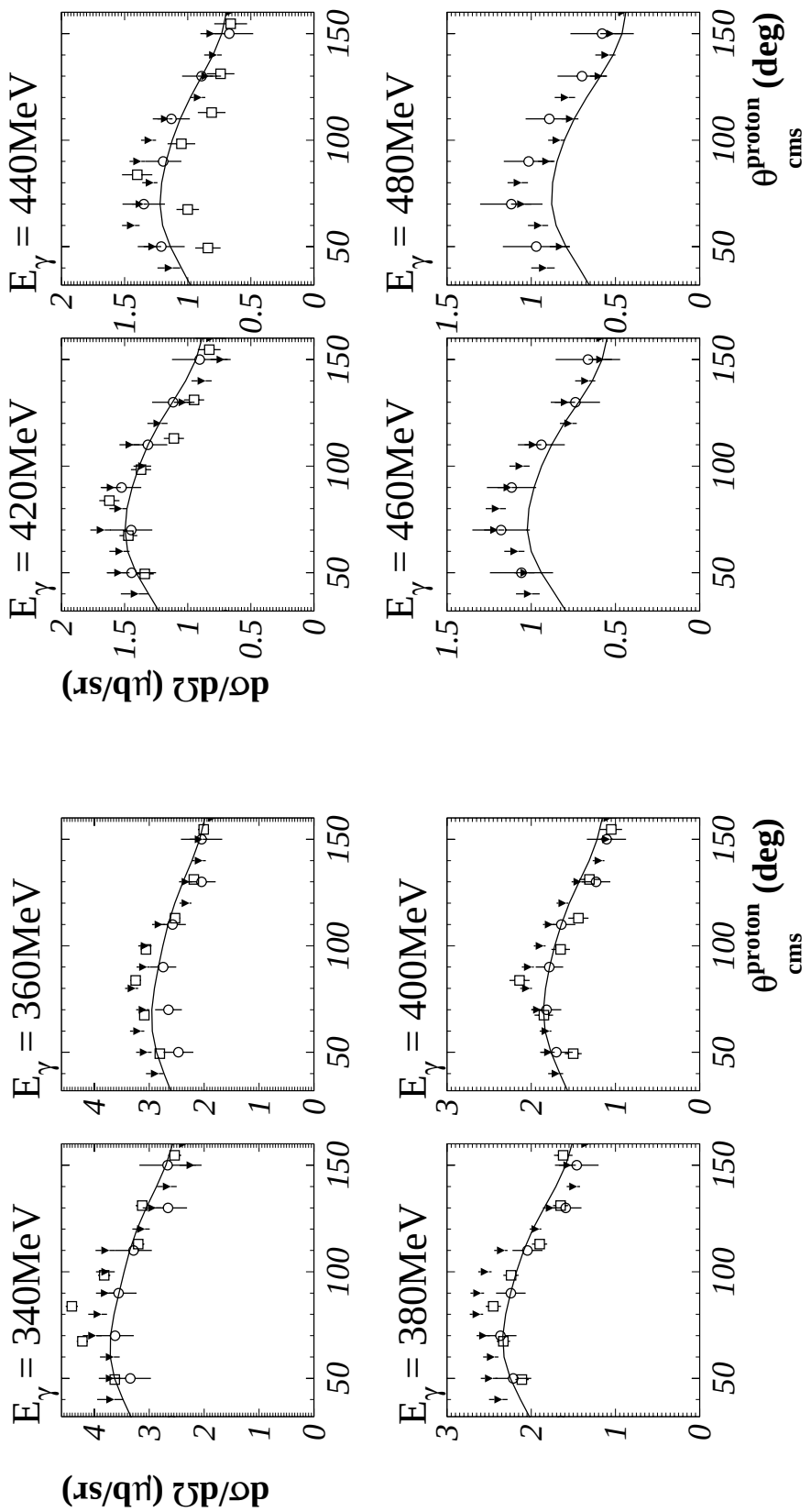

Figure 4.13. Differential cross section for photodisintegration versus polar angle of the proton in center-of-mass frame for photon energies E_γ between 340 and 480 MeV. Each energy bin is 20 MeV wide. The results from this work are represented by open circles. Measurements from [Crawford96] (filled triangles) and [Arends84] (open squares) are given as well. The line represents calculations by M. Schwamb [Schwamb03]. Only statistical errors are plotted.

	$E_\gamma = 180$ MeV	$E_\gamma = 200$ MeV	$E_\gamma = 220$ MeV	$E_\gamma = 240$ MeV	$E_\gamma = 260$ MeV	$E_\gamma = 280$ MeV	$E_\gamma = 300$ MeV
$\vartheta_{\rm cms}^{\rm prot}$ [deg]	$\frac{d\sigma}{d\Omega}\pm$(stat.) [$\mu$b]	$\frac{d\sigma}{d\Omega}\pm$(stat.) [$\mu$b]	$\frac{d\sigma}{d\Omega}\pm$(stat.) [$\mu$b]	$\frac{d\sigma}{d\Omega}\pm$(stat.) [$\mu$b]	$\frac{d\sigma}{d\Omega}\pm$(stat.) [$\mu$b]	$\frac{d\sigma}{d\Omega}\pm$(stat.) [$\mu$b]	$\frac{d\sigma}{d\Omega}\pm$(stat.) [$\mu$b]
30	4.3360±0.3135	4.1734±0.3255	4.3456±0.3511	4.4022±0.3660	4.2466±0.3770	3.9451±0.3901	3.6866±0.4238
50	5.0595±0.2968	5.1185±0.3186	5.2328±0.3403	5.3791±0.3672	5.7358±0.4210	5.5269±0.4308	4.9393±0.4228
70	5.1723±0.2683	5.1635±0.2841	5.5092±0.3109	5.6024±0.3345	6.3933±0.3984	5.7151±0.3791	5.2644±0.3858
90	5.0875±0.2600	5.1486±0.2754	5.3293±0.2954	5.6413±0.3242	5.8729±0.3531	5.7894±0.3707	5.1796±0.3693
110	4.5645±0.2645	4.5761±0.2801	4.9477±0.3055	5.3337±0.3370	5.2458±0.3505	5.0731±0.3630	4.6045±0.3741
130	3.9922±0.2987	4.4340±0.3284	4.3493±0.3437	4.4844±0.3687	4.6416±0.3940	4.4723±0.4049	4.0633±0.4042
150	—	—	—	—	4.2695±0.5597	4.0195±0.5680	3.6661±0.5738

	$E_\gamma = 320$ MeV	$E_\gamma = 340$ MeV	$E_\gamma = 360$ MeV	$E_\gamma = 380$ MeV	$E_\gamma = 400$ MeV	$E_\gamma = 420$ MeV	$E_\gamma = 440$ MeV
$\vartheta_{\rm cms}^{\rm prot}$ [deg]	$\frac{d\sigma}{d\Omega}\pm$(stat.) [$\mu$b]	$\frac{d\sigma}{d\Omega}\pm$(stat.) [$\mu$b]	$\frac{d\sigma}{d\Omega}\pm$(stat.) [$\mu$b]	$\frac{d\sigma}{d\Omega}\pm$(stat.) [$\mu$b]	$\frac{d\sigma}{d\Omega}\pm$(stat.) [$\mu$b]	$\frac{d\sigma}{d\Omega}\pm$(stat.) [$\mu$b]	$\frac{d\sigma}{d\Omega}\pm$(stat.) [$\mu$b]
30	3.0996±0.3938	2.6737±0.3756	2.0641±0.2708	1.7000±0.2132	1.0694±0.1789	0.7228±0.1469	0.5581±0.1341
50	4.2873±0.4096	3.4532±0.3880	2.5466±0.2791	2.2828±0.2194	1.7535±0.2006	1.4890±0.1989	1.2473±0.1921
70	4.6259±0.3725	3.7359±0.3511	2.7339±0.2521	2.4380±0.1963	1.8760±0.1828	1.4927±0.1720	1.3898±0.1734
90	4.3898±0.3482	3.6703±0.3371	2.8339±0.2455	2.3134±0.1810	1.8402±0.1687	1.5715±0.1617	1.2316±0.1491
110	4.0677±0.3582	3.3889±0.3440	2.6596±0.2543	2.1077±0.1846	1.6931±0.1723	1.3566±0.1591	1.1655±0.1510
130	3.2716±0.3708	2.7416±0.3549	2.1121±0.2648	1.6386±0.1904	1.2702±0.1769	1.1492±0.1733	0.9181±0.1596
150	2.9874±0.5221	2.7509±0.5284	2.1109±0.3872	1.5048±0.2669	1.1405±0.2394	0.9334±0.2270	0.6924±0.1956

	$E_\gamma = 460$ MeV
$\vartheta_{\rm cms}^{\rm prot}$ [deg]	$\frac{d\sigma}{d\Omega}\pm$(stat.) [$\mu$b]
30	0.6169±0.1447
50	1.0907±0.1936
70	1.2161±0.1762
90	1.1516±0.1509
110	0.9691±0.1440
130	0.7612±0.1509
150	0.6835±0.1975

Table 4.1. Results for the unpolarized differential photodisintegration cross section.

Chapter 5

Photodisintegration of the Polarized Deuteron for Circularly Polarized Photons of Energies below 450 MeV: Analysis Procedure and Results

ANALYSIS and results for the photodisintegration of polarized deuterons by means of circularly polarized photons is the topic of this chapter. The data have been taken in late 1998 during a pilot measurement that covered some 150 hours of statistics. They were subjected to the analysis method that is described in Chapter 4 with some minute modifications that will be discussed here. These results—another primary objective of this thesis—are the first of their kind since such an experiment had never been carried out before.

The observables of interest are the absorption cross sections for the two possible alignments of the photon helicity and the deuteron spin. The cross section corresponding to the parallel orientation is denoted σ_{p}, while σ_{a} is the cross section for antiparallel orientation. Transversal polarization cannot be achieved with the given target setup.

For reasons given in Section 2.4 on Page 27, deuterated butanol was chosen as target material. This material contains—besides deuterium—carbon and oxygen nuclei. The subtraction of their contributions is easily possible when only considering the difference $\sigma_{\mathrm{p}} - \sigma_{\mathrm{a}}$ of the photodisintegration cross sections. Since both carbon and oxygen are even-even nuclei and hence spinless, their contributions are identical for both cross sections and will cancel in the cross section difference which is shown in Figure 5.1. Unfortunately, the propagated statistical error increases unavoidably when considering the cross section difference (cf. error bars in Figure 5.1 (b)).

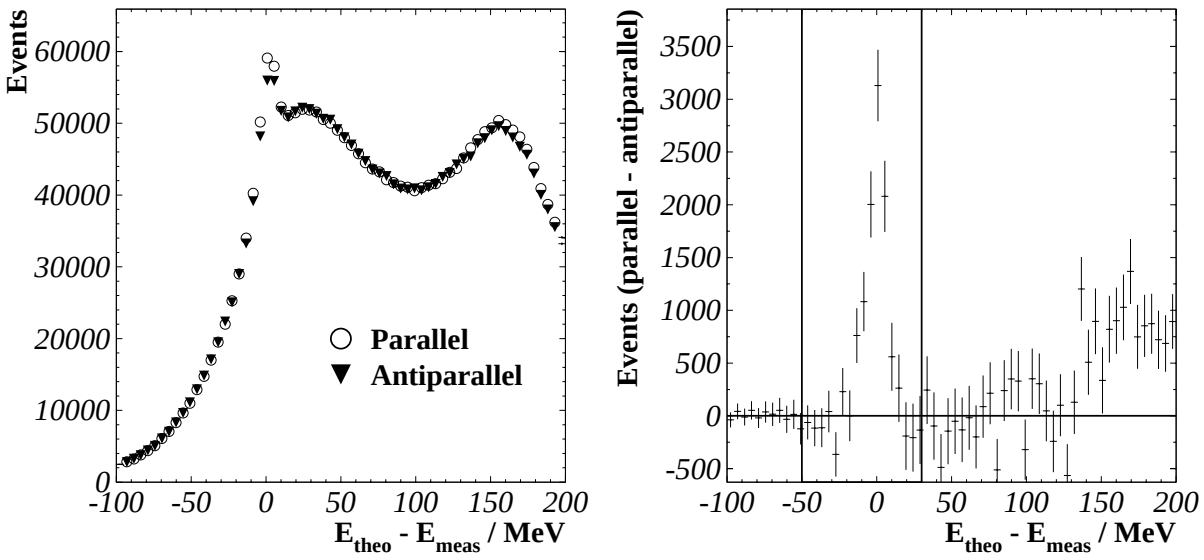

Figure 5.1. a) *Left:* Missing energy spectra for photodisintegration for the helicity-spin orientations parallel (open circles) and antiparallel (solid triangles). b) *Right:* Difference of the missing energy spectra for the two helicity-spin orientations. The vertical lines indicate the cut limits that were applied during analysis.

5.1 Analysis

The analysis of the data from the polarized measurement is in principle identical to the unpolarized case. Yet, the geometrical parameters for the target cell have to be altered and, since the polarization information needs to be included, some important steps have to be added. The geometrical cuts are left unchanged as well as the correction for the random subtraction, the cuts for the reaction kinematics, and—as far as not explicitly mentioned in Section 4.5 on page 75—the cuts for particle identification.

The major part of all changes that are applied affect the dimensions of the polarized target that are different from those of the unpolarized target. The physical dimensions of the former are

$$d_{\text{target}}^{\text{real}} = z_{\text{max}}^{\text{phys}} - z_{\text{min}}^{\text{phys}} = -4.6\text{ mm} - (-23.4\text{ mm}) = 18.8\text{ mm}, \tag{5.1}$$

with the radius $r = 21.5$ mm unaltered. These dimensions are used for the effective target length correction according to Subsection 4.2.2 on Page 71. Because of the vertex reconstruction resolution of the wire chambers of 15 mm, a significant portion (approximately 50 percent) of the target cell would have been ignored when applying the physical limits as cuts to the data. One uses the cancelation of the background contributions of the unpolarized material when considering the cross section difference and increases the software cut limits to the unphysical values

$$d_{\text{target}}^{\text{soft}} = z_{\text{max}} - z_{\text{min}} = 20\text{ mm} - (-40\text{ mm}) = 60\text{ mm}. \tag{5.2}$$

The dimensions of the target cell are safely covered by these limits. Nevertheless, any contribution by material outside the target cell is independent of the incoming photon's helicity since

only the deuterated butanol is polarized. So when calculating the spin asymmetry $\sigma_{\mathrm{p}} - \sigma_{\mathrm{a}}$, all contributions from outside the target cell will cancel.

With the change of the target material, the value for N_{target} and hence for the luminosity changes, too (cf. Equation 4.3 on Page 68). The density of deuterated butanol is $\varrho = 1.109$ g/cm^3. In addition, the filling factor of $f_F = 63$ percent and the dilution factor $f_D = 23.8$ percent (cf. Section 2.4 on page 31) have to be taken into account. This gives $f_D \cdot N_{\mathrm{target}} = 4.972 \cdot 10^{22}\mathrm{cm}^{-3}$.

Due to the low statistics of the 1998 pilot measurement the relatively fine binning in energy and ϑ that was used for the unpolarized data cannot be retained. Instead, enlarged bin widths in energy ($\Delta E_\gamma = 40$ MeV) and polar angle ($\Delta\vartheta = 30$ degrees) are used to present the results of the doubly polarized measurement.

Including the polarization transfer as introduced in Equation 2.4 on Page 24 and with P_{target} the absolute target polarization, the total and differential polarized cross sections read

$$(\sigma(E_\gamma))_{\mathrm{p/a}} = \frac{N_{\mathrm{det}}(E_\gamma) \cdot \varepsilon_{\mathrm{pair}}(E_\gamma)}{N_{\mathrm{pair}}(E_\gamma) \cdot \varrho\frac{N_A}{A} \cdot d_{\mathrm{target}} \cdot \varepsilon_{\mathrm{det}}(E_\gamma)} \cdot C_{\mathrm{transfer}} \tag{5.3}$$

and

$$\left(\frac{\mathrm{d}\sigma(E_\gamma)}{\mathrm{d}\vartheta}\right)_{\mathrm{p/a}} = \frac{C_{\mathrm{transfer}}}{2\pi(\cos\vartheta_2 - \cos\vartheta_1)} \cdot \frac{N_{\mathrm{det}}(E_\gamma) \cdot \varepsilon_{\mathrm{pair}}(E_\gamma)}{N_{\mathrm{pair}}(E_\gamma) \cdot \varrho\frac{N_A}{A} \cdot d_{\mathrm{target}} \cdot \varepsilon_{\mathrm{det}}(E_\gamma)}, \tag{5.4}$$

respectively, with

$$C_{\mathrm{transfer}} = \frac{1}{P_{\mathrm{target}} \cdot P_{\mathrm{el}}} \cdot \frac{4E_0^2 - 4E_\gamma E_0 + 3E_\gamma^2}{4E_\gamma E_0 - E_\gamma^2} \tag{5.5}$$

the inverted polarization transfer divided by the target polarization (cf. Equations 4.4 and 4.5 on page 68.) The particular helicity-spin orientation is given by the knowledge of the MAMI spin orientation and the direction of the target polarization.

With these changes, the polarized data were analyzed. Figure 5.1 shows an example for the missing energy distributions for the two helicity-spin orientations. The basic difference to Figure 4.11 on Page 80 is the additional contribution in Figure 5.1 (a) at positive missing energy values below approximately 100 MeV from the carbon and the oxygen nuclei in the butanol. Figure 5.1 (b) presents the difference of the two spectra. It can clearly be seen that all unpolarized contributions cancel. Above $E_{\mathrm{miss}} = 130$ MeV contributions from the neutral pion production are visible, c. f. Section 4.6.

5.2 Results and Error Discussion

Figure 5.2 shows the results obtained for the polarized data for the difference of the differential cross sections $\Delta\left(\frac{\mathrm{d}\sigma}{\mathrm{d}\Omega}\right) \equiv \left(\frac{\mathrm{d}\sigma}{\mathrm{d}\Omega}\right)_p - \left(\frac{\mathrm{d}\sigma}{\mathrm{d}\Omega}\right)_a$ as functions of the proton's polar angle in the center-of-mass system together with calculations using the model by [Schwamb01], c. f. Chapter 1, represented by the full line. The statistical errors are in the order of 50 percent and only these

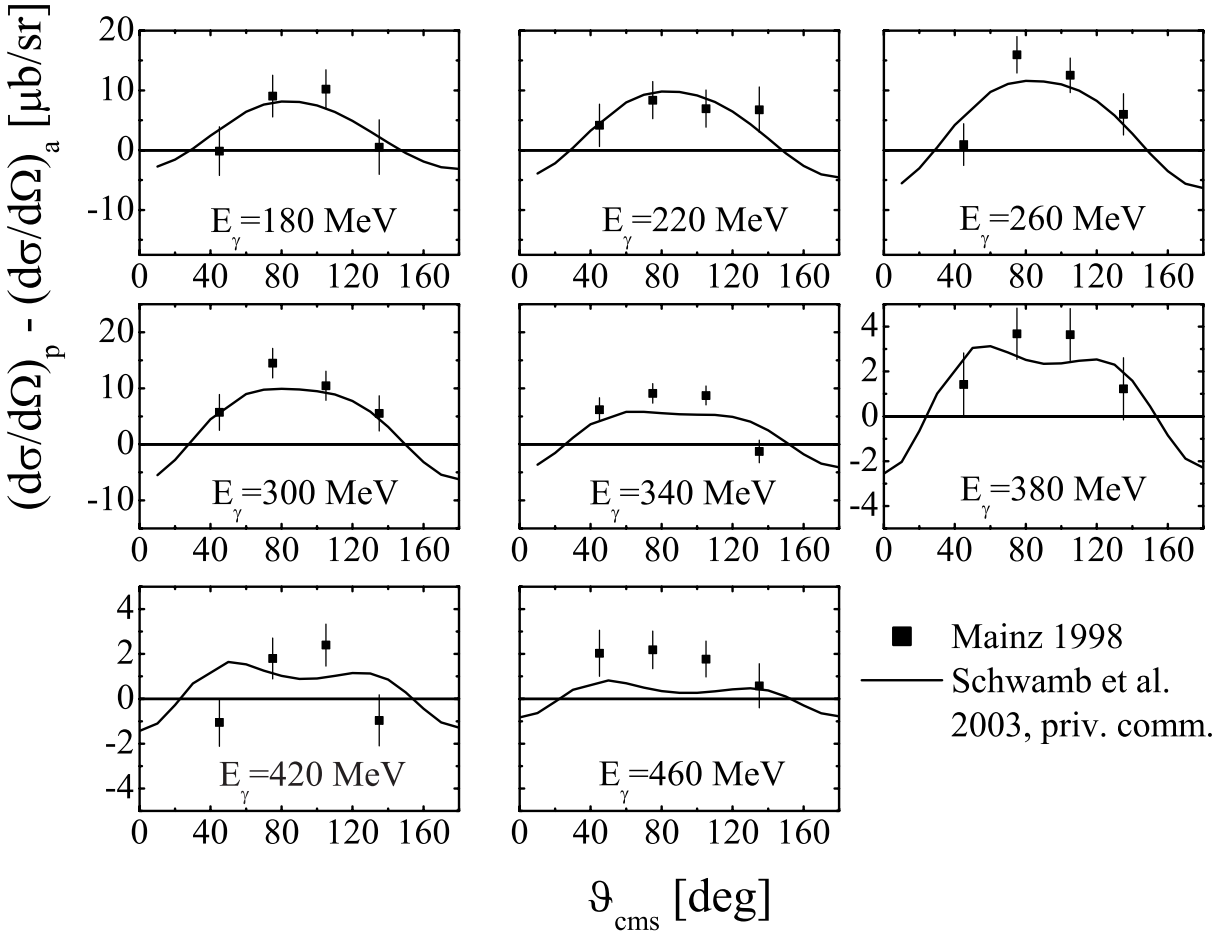

	$E_\gamma = 180$ MeV	$E_\gamma = 220$ MeV	$E_\gamma = 260$ MeV
$\vartheta_{\rm cms}^{\rm prot}$ [deg]	$\Delta\left(\frac{d\sigma}{d\Omega}\right)$ ±(stat.) [μb]	$\Delta\left(\frac{d\sigma}{d\Omega}\right)$ ±(stat.) [μb]	$\Delta\left(\frac{d\sigma}{d\Omega}\right)$ ±(stat.) [μb]
45	-0.16 ± 4.07	4.17 ± 3.54	0.95 ± 3.49
75	9.04 ± 3.50	8.38 ± 3.12	15.97 ± 3.05
105	10.20 ± 3.25	6.94 ± 3.12	12.53 ± 2.88
135	0.52 ± 4.57	6.76 ± 3.80	6.00 ± 3.45

	$E_\gamma = 300$ MeV	$E_\gamma = 340$ MeV	$E_\gamma = 380$ MeV
$\vartheta_{\rm cms}^{\rm prot}$ [deg]	$\Delta\left(\frac{d\sigma}{d\Omega}\right)$ ±(stat.) [μb]	$\Delta\left(\frac{d\sigma}{d\Omega}\right)$ ±(stat.) [μb]	$\Delta\left(\frac{d\sigma}{d\Omega}\right)$ ±(stat.) [μb]
45	5.70 ± 3.21	6.19 ± 2.12	1.43 ± 1.40
75	14.48 ± 2.64	9.08 ± 1.75	3.68 ± 1.15
105	10.46 ± 2.61	8.72 ± 1.70	3.65 ± 1.16
135	5.53 ± 3.13	-1.28 ± 2.02	1.22 ± 1.39

	$E_\gamma = 420$ MeV	$E_\gamma = 460$ MeV	—
$\vartheta_{\rm cms}^{\rm prot}$ [deg]	$\Delta\left(\frac{d\sigma}{d\Omega}\right)$ ±(stat.) [μb]	$\Delta\left(\frac{d\sigma}{d\Omega}\right)$ ±(stat.) [μb]	—
45	-1.06 ± 1.06	2.03 ± 1.03	—
75	1.80 ± 0.91	2.18 ± 0.84	—
105	2.40 ± 0.94	1.77 ± 0.80	—
135	-0.96 ± 1.14	0.58 ± 0.98	—

Figure 5.2. *Page 88, top:* Results for the dependence of the difference of the differential photodisintegration cross sections $\left(\frac{\mathrm{d}\sigma}{\mathrm{d}\Omega}\right)_p - \left(\frac{\mathrm{d}\sigma}{\mathrm{d}\Omega}\right)_a$ from the polar angle ϑ of the proton for several photon energies E_γ. ϑ is given in center-of-mass system; the energy bin width is 40 MeV for each bin. Only statistical errors are shown. The lines represent calculations by M. Schwamb, see Refs. [Schwamb01], [Schwamb03]. Note the change in the vertical scale for $E_\gamma \geq 380$ MeV.

Table 5.1. *Page 88, bottom:* Results for the difference of the polarized differential photodisintegration cross sections of the deuteron.

are plotted. Unlike in the unpolarized case, here the statistical errors decrease with increasing photon energy since their behavior is dominated by the photon polarization that increases with energy, c. f. Equation 2.4 on Page 24. The agreement between the theory and the experiment is surprisingly good although there seems to exist a slight tendency to underestimate the data. This behavior is better visible when plotting the total asymmetry, c. f. below. Certainly, the lack in precision does not allow to draw final conclusions about the validity of details of the theoretical calculation like offshell effects, etc. that give contributions at and below a 5 percent level, but at least the sign of the differential asymmetry and the magnitude of the cross sections can be confirmed for the first time. With only four data points, the saddle-shaped structure at photon energies above 340 MeV can neither be contradicted nor confirmed. One has to wait for the results of the 2003 GDH measurement that will allow for a finer binning in both energy and polar angle to give a reliable statement concerning this issue.

To gain the total cross section difference information $\sigma_p - \sigma_a$ for the photodisintegration reaction, too, the results for the differential cross sections were integrated over the covered ϑ-region for each energy bin. In addition, it is necessary to account for contributions in the angular regions that are not covered by the experimental setup. At this point a theoretical model is required that can calculate these contributions. The agreement between the calculations by [Schwamb01] and the results for the differential cross section difference $\Delta\left(\frac{\mathrm{d}\sigma}{\mathrm{d}\Omega}\right)$ gave confidence in the validity of this model, and hence it was used to obtain the extrapolation corrections. Due to the expected zero crossing of the differential asymmetry in the uncovered angular regions, the corrections are at most 5.3 percent for all energies.

The experimental results for $\sigma_p - \sigma_a$ are presented in Figure 5.3 and listed in Table 5.2 together with the extrapolation corrections. The predictions by Schwamb reproduce quite nicely the shape of the total asymmetry, although—as mentioned above—the cross section is seems to be underestimated in the photon energy region between 260 and 340 MeV. In fact, the dashed line represents the results for calculations using the Bonn r-space potential as published in [Machleidt87] that includes meson exchange currents, isobar configurations and relativistic corrections in addition, one could get the impression that the experiment is slightly better described by the latter model. Unfortunately, the statistical error alone covers most of the difference, so together with the systematic uncertainties that are discussed below it is not possible to decide for one model.

As has been mentioned when discussing the analysis of the unpolarized data in Section 4.8, the incoherent π^0-production gives a non-negligible contribution only at 460 MeV photon energy. This contribution is estimated to stay below 15 percent. A test of a possible intrinsic

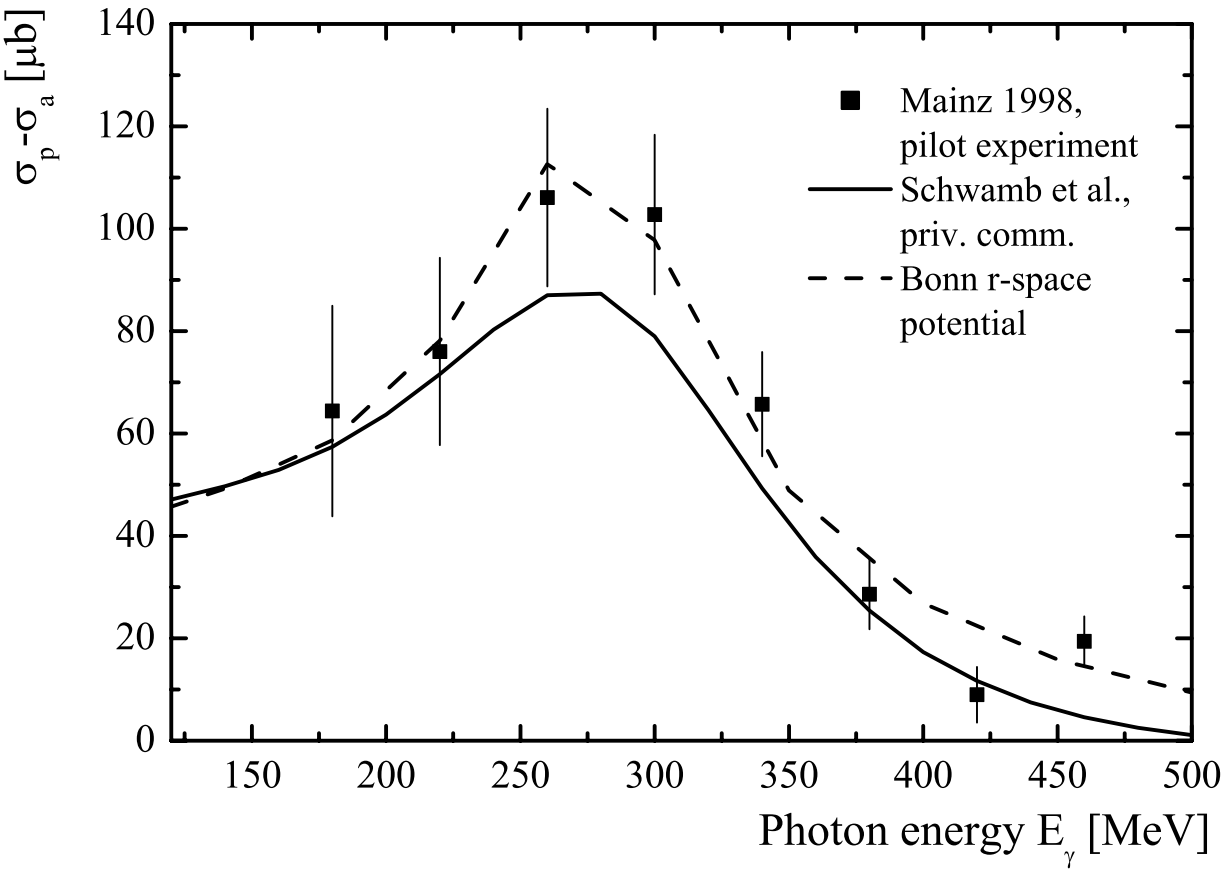

Figure 5.3. Results for the energy dependence of the difference of the total photodisintegration cross sections $\sigma_p - \sigma_a$ in the photon energy range between E_γ = 200 MeV and E_γ = 460 MeV. Only statistical errors are shown. The full line shows calculations by M. Schwamb, see Refs. [Schwamb01], [Schwamb03]. His calculations for the differential cross section difference were used to extrapolate to full solid angle. The dashed line represents calculations using the Bonn r-space potential as described in [Machleidt87] additionally taking meson-exchange currents, isobar configurations and relativistic corrections into account.

E_γ [MeV]	$(\sigma_\mathrm{p} - \sigma_\mathrm{a})\pm$(stat.) [$\mu$b]	Δ_extrapol [μb]
180	64.40 ± 20.57	3.14
220	76.02 ± 18.30	2.72
260	106.10 ± 17.36	0.58
300	102.77 ± 15.58	-1.40
340	65.72 ± 10.19	-1.50
380	28.62 ± 6.84	-0.49
420	8.99 ± 5.44	0.44
460	19.40 ± 4.90	0.97

Table 5.2. Results for the difference of the total photodisintegration cross sections of the deuteron and the extrapolation corrections obtained using the model of Schwamb.

asymmetry of the detector has been carried out in a short beam period with zero target polarization but with a polarized photon beam. All hadronic events with a good time correlation to the tagger have been accepted. The result of this measurement is plotted in Figure 5.4 showing the asymmetry $E_N = (N_p - N_a)/(N_p + N_a)$ as a function of photon energy. The indices a and p refer to the photon polarization settings that were used in the doubly polarized experiment. A weighted mean asymmetry value of (0.07 ± 0.10) percent is found. Taking the contributions from carbon and oxygen nuclei into account which are present for the sum, but not for the difference, this value underestimates the true intrinsic asymmetry by a factor five [Holvoet00] which is still negligible. For the remaining systematical uncertainties several sources are to be considered. These are the photon flux hitting the target with a systematic error of 2 percent, the photon beam polarization degree with an error of 3 percent, and the polarization of the Møller target foil with an error of 2 percent. Another uncertainty arises from a broken connection between a B layer scintillator and one of its light-guides, giving an effect of 3 percent. Adding these contributions quadratically one has a total systematic error of 4.7 percent for the differential asymmetry. In the case of the total asymmetry, the contributions for the extrapolation into the uncovered polar-angle regions have been taken as systematic uncertainties as well, resulting in a total systematic error of 7.1 percent.

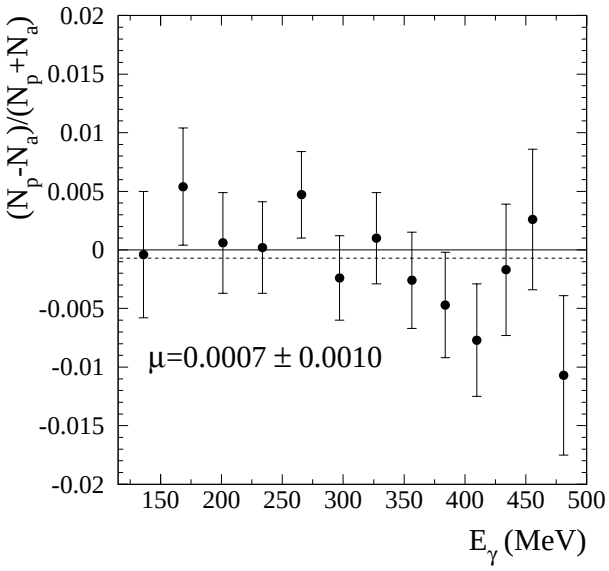

Figure 5.4. Measured apparatus asymmetry in number of events as a function of photon energy in the Δ-region.

Summarizing, one can say that—apart from the above mentioned small deviations—all results confirm the current picture of the NN interaction in the Δ-region. Since the Δ-resonance plays the dominant role it is not possible to gain a more sophisticated understanding of e. g. off-shell effects which make up at most a few percent of the total cross sections. To also achieve this, the analysis of a data set that includes much more statistics than this test measurement is necessary. However, it has been shown that is possible to obtain reasonable results from the apparatus.

Chapter 6

Summary and Outlook

A PILOT experiment was carried out in 1998 to study the helicity dependence of photoreaction cross sections on the deuteron. For this, energy-tagged circularly polarized real photons interacted with longitudinally polarized deuterons in a deuterated butanol target. The knowledge of these cross sections is required to test the validity of the Gerasimov-Drell-Hearn sum rule on the deuteron. The focus of this thesis was on the results for the differential and total cross sections for the photodisintegration reaction for various photon energies in the range from 200 to 450 MeV. The results obtained do not contradict the current theoretical understanding of NN interaction as it is represented by calculations from M. Schwamb. In preparation of the nGDH experiment of 2003, the detector DAPHNE was renewed, i. e. all plastic scintillators were replaced with new material. The according work was presented together with the results of the quality-test measurements of the renewed detector components.

The natural way to continue this work is the analysis of the 2003 data which provide much more statistics. Since the DAPHNE detector was only in a very limited way suitable for the investigation of reaction channels with neutral particles in the final state, a subsequent experiment would make use of the Crystal Ball detector's high efficiency for photon detection. This detector is currently present in Mainz and could be used to investigate these channels. The necessary polarized targets (frozen-spin and polarized He3) are currently being built in Mainz. In addition, measurements to determine the GDH integrand at photon energies between 5 MeV and pion production threshold are planned at the HIγS facility, Durham, North Carolina, for the next years [Weller04].

Appendix A

Photodisintegration—Reaction Kinematics

In this chapter the relations between laboratory and cm frame as well as the reaction kinematics will be given.

As already presented in Chapter 1, the initial and final state of a deuteron photodisintegration reaction are specified by the four-momenta, p_i, and the polarization density matrices, ϱ^i, of the reactants (photon and deuteron) and the reaction products (free proton and free neutron), respectively. As a reminder, Figure 1.2 is re-drawn below to illustrate the situation.

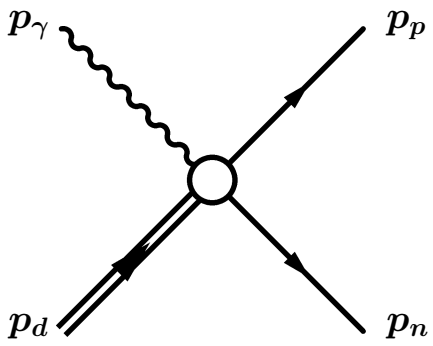

Figure A.1. Diagram for deuteron photodisintegration with the definition of momenta.

The two interesting frames of reference are the laboratory frame and the center-of-mass frame. The latter shall be the frame of preference. All quantities referring to the laboratory frame shall be labeled "L", while the quantities of the cm frame shall not bear such explicit labeling. The kinematical quantities in the laboratory frame are the four-momenta

$$\begin{aligned} p_\gamma^L &= (\omega^L, \vec{\omega}^L), \\ p_d^L &= (M^L, \vec{0}), \end{aligned}$$

and in the cm frame

$$\begin{aligned} p_\gamma &= (\omega, \vec{\omega}), \\ p_d &= (E_d, -\vec{\omega}), \quad E_d = \sqrt{M_d^2 + \vec{\omega}^2} \\ p_p &= (E_p, \vec{k}), \quad E_p = \sqrt{M_p^2 + \vec{k}^2} \\ &= p_1, \\ p_n &= (E_n, -\vec{k}), \quad E_n = \sqrt{M_n^2 + \vec{k}^2} \\ &= p_2 \end{aligned}$$

Introducing the total cm energy W, i. e. the invariant mass,

$$W = E_p + E_n = \omega + E_d,$$

and the asymptotic final-state kinetic energy

$$E_{np} = W - M_p - M_n$$

one yields the following relations between laboratory and cm frame

$$\omega = \omega^L \left(1 + \frac{2\omega^L}{M_d}\right)^{-1/2}, \tag{A.1}$$

$$W = M_d \left(1 + \frac{2\omega^L}{M_d}\right)^{1/2}. \tag{A.2}$$

Using energy conservation one obtains

$$\vec{k}^2 = \frac{1}{4W^2}\left\{W^2 - (M_p + M_n)^2\left[W^2 - (M_p - M_n)^2\right]\right\}, \tag{A.3}$$

which, using $M_p \approx M_n \equiv M$, reduces to

$$\vec{k}^2 = \frac{1}{4}\left(W^2 - 4M^2\right) = \frac{1}{4}E_{np}(E_{np} + 4M). \tag{A.4}$$

Introducing total and relative momentum for the two-particle channels by

$$P = p_1 + p_2, \tag{A.5}$$

$$p = \frac{1}{2}(p_1 - p_2), \tag{A.6}$$

one has for the initial and final states in the cm frame

$$P_i = (W, \vec{0}), \tag{A.7}$$

$$p_i = \left(\frac{1}{2}(\omega - E_d), \vec{\omega}\right), \tag{A.8}$$

$$P_f = P_i, \tag{A.9}$$

$$p_f = \left(\frac{1}{2}(E_p - E_n), \vec{k}\right) \overset{M_p \approx M_n \equiv M}{=} (0, \vec{k}). \tag{A.10}$$

Appendix B

DAPHNE

B.1 Geometrical Specifications

Angular acceptance			
Polar angle	$21^\circ < \vartheta < 159^\circ$		
Azimuthal angle	$0^\circ < \varphi < 360^\circ$		
Charged-particle detection thresholds (1 g/cm^2 target)			
Pions	$T = 12$ MeV	($p = 60$ MeV/c)	
Protons	$T = 23$ MeV	($p = 220$ MeV/c)	
Maximum energy of particles stopped in scintillators A, B and C			
Pions	$\vartheta = 90^\circ$	$T = 12$ MeV	($p = 138$ MeV/c)
	$\vartheta = 21^\circ$	$T = 120$ MeV	($p = 219$ MeV/c)
Protons	$\vartheta = 90^\circ$	$T = 125$ MeV	($p = 500$ MeV/c)
	$\vartheta = 21^\circ$	$T = 225$ MeV	($p = 668$ MeV/c)

Table B.1. Principal characteristics of DAPHNE.

Layer	Material	Length [mm]	Thickness [mm]	Radius [mm]
A	NE-110 (equiv. BC-412)	865	10	156
B	NE-102A (equiv. BC-400)	1420	100	172
C	NE-102A	1475	5	277
Converter	Steel/Pb	—	10	299
D	NE-110	1700	5	309
Converter	Pb	—	5	316
E	NE-110	1708	5	322
Absorber	Al	—	6	328.5
F	NE-110	1720	5	334

Table B.2. Geometrical specifications of the DAPHNE plastic-scintillator and converter layers [Maurier]. *Radius* is the radius of a circle centered on the beam axis and inscribed in the inner surface of the polygon built of the 16 segments of each layer. Also given is today's equivalent product ID of the scintillator material.

B.2 Sub-triggers

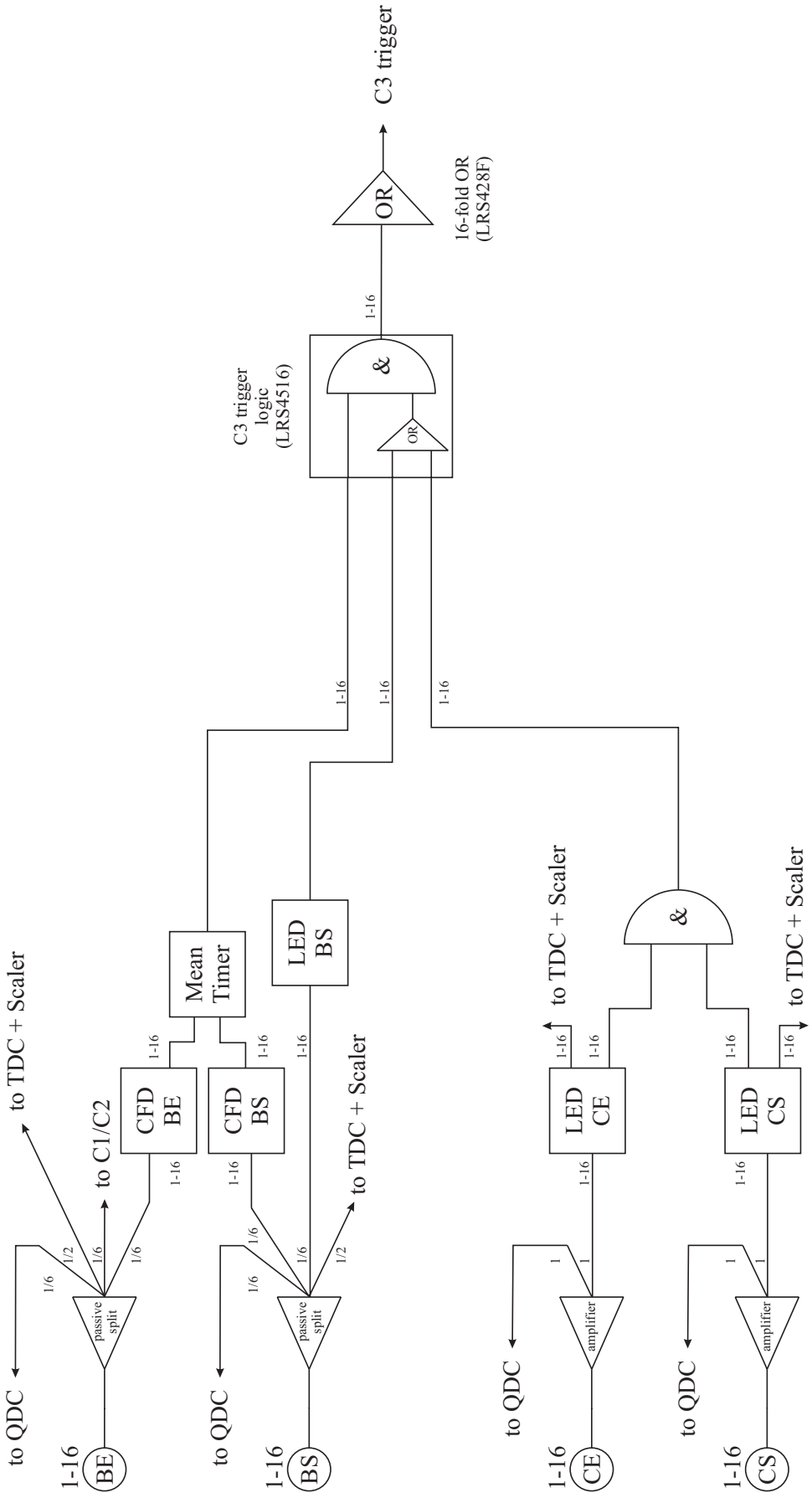

Figure B.1. Schematics showing the DAPHNE sub-trigger C3. The trigger condition is processed for each of the 16 DAPHNE sectors individually before being merged by a 16-fold OR.

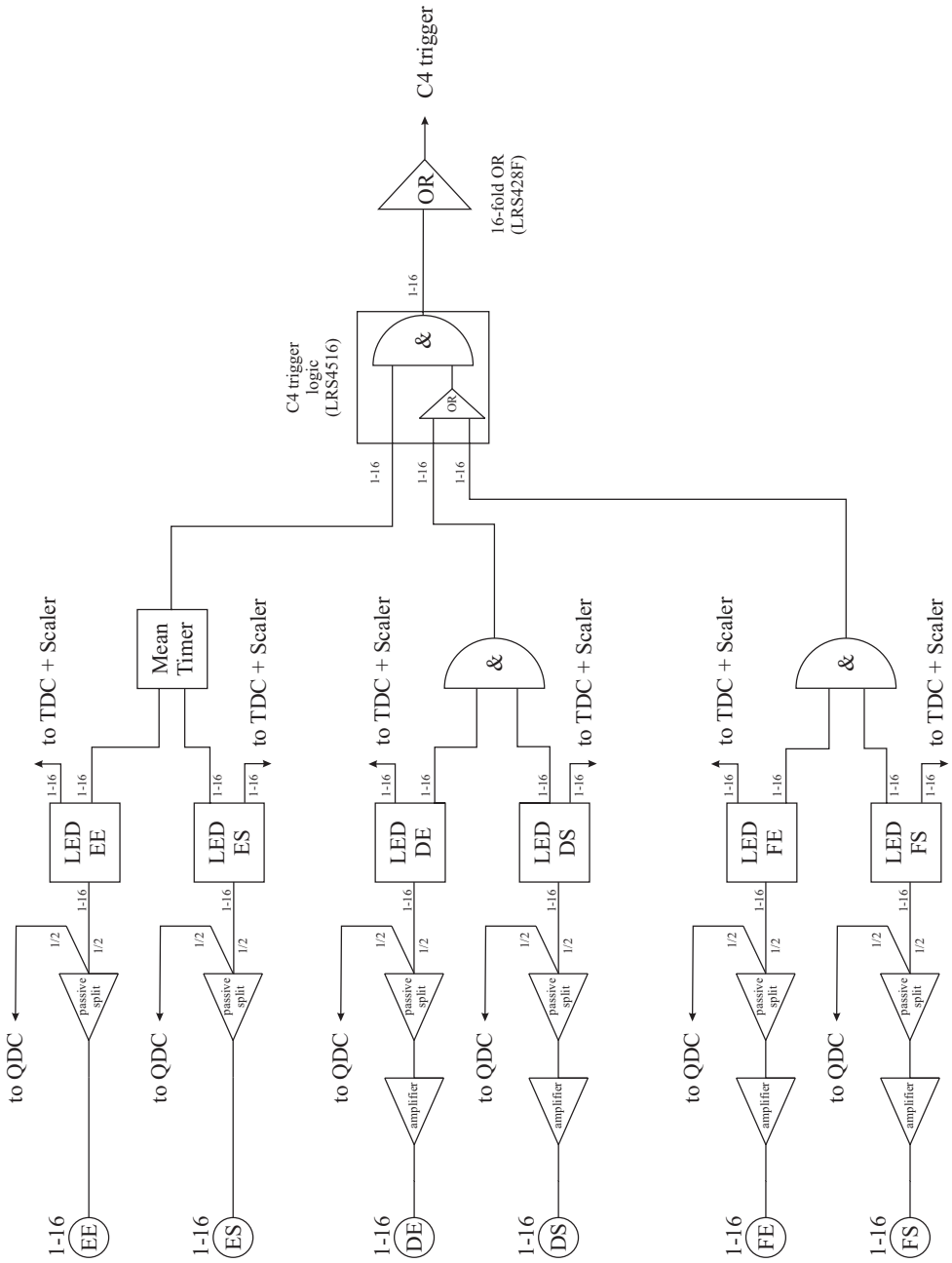

Figure B.2. Schematics showing the DAPHNE sub-trigger C4. The trigger condition is processed for each of the 16 DAPHNE sectors individually before being merged by a 16-fold OR.

List of Figures

List of Tables

Bibliography

[Abragam78] A. Abragam and M. Goldman, *Principles of dynamic nuclear polarisation,* Rep. Prog. Phys. **41** (1978) 395–467.

[Al-Obaidi78] S.J. Al-Obaidi et al., *Energy Transfer in Organic Systems XII. Mixed crystals,* J. Phys. B: Atom. Molec. Phys. **11** 13 (1978) 2301.

[Altieri00] S. Altieri et al., *A compact solid-state detector for small angle particle tracking,* Nucl. Instr. Meth. **A452** (2000) 185–191.

[Alvarez04] L. Alvarez-Gaumé et al. (editors), *Review of Particle Physics,* Phys. Lett. **B592** (2004) 1–1109.

[Anthony91] I. Anthony et al., *Design of a tagged photon spectrometer for use with the Mainz 840 MeV microtron,* Nucl. Instr. Meth. **A301** (1991) 230–240.

[Arends84] H.J. Arends et al., *Experimental investigation of deuteron photodisintegration in the δ-resonance region,* Nucl. Phys. **A412** (1984) 509.

[Arenhövel91] H. Arenhövel and M. Sanzone, *Photodisintegration of the Deuteron—A Review of Theory and Experiment,* Few-Body Systems, Suppl. 3 (1991, Springer-Verlag).

[Arenhövel97] H. Arenhövel et al., *The spin response of the deuteron and its implication for the Gerasimov-Drell-Hearn sum rule,* Phys. Lett. **B407** (1997) 1.

[Arenhövel04] H. Arenhövel et al., *Spin Asymmetry and Gerasimov-Drell-Hearn Sum Rule for the Deuteron,* Phys. Rev. Lett. **93** (2004) 202301.

[Audit91] G. Audit et al., DAPHNE: *a large-acceptance tracking detector for the study of photoreactions at intermediate energies,* Nucl. Instr. Meth. **A301** (1991) 473–481.

[Barkas56] W. Barkas, *Mass-ratio Method Applied to the Measurement of L-Meson Masses and the Energy Balance in Pion Decay,* Phys. Rev. **101** 2 (1956) 778.

[Berger00] M.J. Berger, J.S. Coursey, and M.A. Zucker, *ESTAR, PSTAR, and ASTAR: Computer Programs for Calculating Stopping-Power and Range Tables for Electrons, Protons, and Helium Ions (version 1.2.2),* (2000). Online available: `http://physics.nist.gov/Star`. National Institute

of Standards and Technology, Gaithersburg, MD. Originally published as: Berger, M.J., NISTIR 4999, National Institute of Standards and Technology, Gaithersburg, MD (1993).

[Bichsel88] H. Bichsel, *Straggling in thin silicon detectors*, Rev. Mod. Phys. **60** 3 (1988) 663.

[Bichsel92] H. Bichsel, *Stopping power and ranges of fast ions in heavy elements*, Phys. Rev. **A49** 9 (1992) 5761.

[Birks54] J.B. Birks, *Energy Transfer in Organic Phosphors*, Phys. Rev. **94** 6 (1954).

[Birks58] J.B. Birks and A.J.W. Cameron, *Energy Transfer in Organic Systems I: Photofluorescence of Terphenyl-toluene Solutions*, Proc. Phys. Soc. **72** 1 (1958) 53.

[Birks61] J.B. Birks and K.N. Kuchela, *Energy Transfer in Organic Systems II: Solute-Solute Transfer in Liquid Solutions*, Proc. Phys. Soc. **77** 5 (1961) 1083.

[Birks61a] J.B. Birks, K.N. Kuchela and F.H. Read, *Energy Transfer in Organic Systems III: Spectral Effects in Liquid Solutions*, Proc. Phys. Soc. **77** 5 (1961) 1095.

[Birks64] J.B. Birks, *The Theory and Practice of Scintillation Counting* (1964, Oxford: Pergamon Press).

[Birks68] J.B. Birks, S. Georghiou and I.H. Munro, *Energy Transfer in Organic Systems V. Lifetime studies of anthracene-perylene transfer in benzene solutions*, J. Phys. B: Atom. Molec. Phys. **1** 2 (1968) 266.

[Birks68a] J.B. Birks, *Energy Transfer in Organic Systems VI. Fluorescence response functions and scintillation pulse shapes*, J. Phys. B: Atom. Molec. Phys. **1** 5 (1968) 946.

[Birks68b] J.B. Birks and S. Georghiou, *Energy Transfer in Organic Systems VII. Effect of diffusion on fluorescence decay*, J. Phys. B: Atom. Molec. Phys. **1** 5 (1968) 958.

[Birks70] J.B. Birks and M.S.S.C.P. Leite, *Energy Transfer in Organic Systems VIII. Quenching of naphtalene fluorescence by biacetyl*, J. Phys. B: Atom. Molec. Phys. **3** 3 (1970) 417.

[Birks70a] J.B. Birks and M.S.S.C.P. Leite, *Energy Transfer in Organic Systems IX. Effect of diffusion on transfer efficiency*, J. Phys. B: Atom. Molec. Phys. **3** 4 (1970) 513.

[Birks70b] J.B. Birks, *Energy Transfer in Organic Systems X. Pure and mixed crystals*, J. Phys. B: Atom. Molec. Phys. **3** 12 (1970) 1704.

[Birks71] J.B. Birks, H.Y. Najjar and M.D. Lumb, *Energy Transfer in Organic Systems XI. Temperature dependence of singlet excitation transfer and quenching in toluene solutions,* J. Phys. B: Atom. Molec. Phys. **4** 11 (1971) 1516.

[Bowen49] E.J. Bowen, E. Mikiewicz and F.W. Smith, *Resonance Transfer of Electronic Energy in Organic Crystals,* Proc. Phys. Soc. **A62** 1 (1949) 26.

[Bradtke99] A. Bradtke et al., *A new frozen-spin target for 4π particle detection,* Nucl. Instr. Meth. **A436** (1999) 430–442.

[Braghieri] A. Braghieri and P. Pedroni, *DAPHNE Wire Chambers Data Analysis,* DAPHNE Internal Note, May 1989;

A. Braghieri, V. Isbert and P. Pedroni, *MWPCs Tracks Fitting,* DAPHNE Internal Note, January 1992;

A. Braghieri and P. Pedroni, *MWPCs Tracks Coupling,* DAPHNE Internal Note, April 1992.

[Braghieri94] A. Braghieri et al., *A range telescope technique for particle discrimination and energy reconstruction,* Nucl. Instr. Meth. **A343** (1994) 623–628.

[Crawford96] R. Crawford, *Two-body photodisintegration of the deuteron from 100 to 800 MeV,* Nucl. Phys. **A603** (1996) 303–325.

[Crispin70] A. Crispin, *Density Effect in the Ionization Energy Loss of Fast Charged Particles in Matter,* Rev. Mod. Phys. **42** 3 (1970) 290.

[Darby67] M.I. Darby, *Tables of the Brillouin function and of the related function for the spontaneous magnetization,* Brit. J. Appl. Phys. **18** (1967) 1415–1417.

[Dexter53] D.L. Dexter, *A Theory of Sensitized Luminescence in Solids,* J. Chem. Phys. **21** (1953) 836.

[Domingo00] C. Domingo Pardo, *Neuaufbau und Test der* DAPHNE*-Szintillationszähler für die Messung der* GDH*-Summenregel am Deuteron,* diploma thesis, University of Mainz, 2000 (unpublished).

[Drell66] S.D. Drell and A.C. Hearn, *Exact Sum Rule for Nucleon Magnetic Moments,* Phys. Rev. Lett. **16** (1966) 908.

[Dutz04] H. Dutz et al., *Experimental Check of the Gerasimov-Drell-Hearn Sum Rule for ^1H,* Phys. Rev. Lett. **93** (2004) 032003.

[Dutz05] H. Dutz et al., *Measurement of Helicity-Dependent Photoabsorption Cross Sections on the Neutron from 815 to 1825 MeV,* Phys. Rev. Lett. **94** (2005) 162001.

[Edmonds68] A.R. Edmonds, *Angular Momentum in Quantum Mechanics,* 2nd ed., rev. printing. Princeton, NJ: Princeton University Press, 1968.

[Elster88] Ch. Elster et al., *Extension of the Bonn meson exchange NN potential above pion production threshold: Nucleon renormalization and unitarity,* Phys. Rev. **C37** 4 (1988) 1647.

[Fermi40] E. Fermi, *The Ionization Loss of Energy in Gases and in Condensed Materials,* Phys. Rev. **57** (1940) 485.

[Förster48] Th. Förster, *Zwischenmolekulare Energiewanderung und Fluoreszenz,* Ann. Phys. **2** (1948) 55;

Experimentelle und theoretische Untersuchung des zwischenmolekularen Übergangs von Elektronenanregungsenergie, Z. Naturforsch. **4a** (1949) 321.

[Franck38] J. Franck and E. Teller, *Migration and Photochemical Action of Excitation Energy in Crystals,* J. Chem. Phys. **6** 12 (1938) 861.

[Friar77] J.L. Friar, *Low-energy theorem for Compton scattering and the Drell-Hearn-Gerasimov sum rule: Exchange currents,* Phys. Rev. **C16** (1977) 1504.

[Garwin52] R.L. Garwin, *The Design of Liquid Scintillation Cells,* Rev. Sci. Instr. **23** 12 (1952) 755.

[Garwin60] R.L. Garwin, *The Collection of Light from Scintillation Counters,* Rev. Sci. Instr. **31** 9 (1960) 1010.

[Gerasimov66] S.B. Gerasimov, *Sum Rule for Magnetic Moments and the Damping of the Nucleon Magnetic Moment in Nuclei,* Sov. J. Nucl. Phys. **2** (1966) 430.

[Giménez02] E.N. Giménez Navarro, *Test of the renewed* DAPHNE *Detector with Cosmic Radiation,* diploma thesis, University of Mainz, 2002 (unpublished).

[Goertz02] S. Goertz et al., *Polarized H, D and ^{3}He Targets for Particle Physics Experiments,* Prog. Part. Nucl. Phys. **49** (2002) 403–489.

[Hall96] S.J. Hall et al., *A focal plane system for the 855 MeV tagged photon spectrometer at MAMI-B,* Nucl. Instr. Meth. **A368** (1996) 698–708.

[Hallam78] A. Hallam and J.B. Birks, *Energy Transfer in Organic Systems XIII. Plastic scintillators,* J. Phys. B: Atom. Molec. Phys. **11** 18 (1978) 3273.

[Henry73] T.W. Henry, IEEE Trans. Nucl. Sci. NS-20 5, 56 (1973).

[Holvoet00] H. Holvoet, *Study of the helicity dependence of double pion photoproduction on the proton,* Ph.D. thesis, University of Gent, 2000.

[Hosada66] M. Hosada and K. Yamamoto, *Prog. Theor. Phys.* **36** (1966) 425.

[Isbert93] V. Isbert, *Photodésintégration de l'^{3}He entre 200 et 800 MeV,* Ph.D. thesis, DAPNIA/SPhN 93 51, 1993.

[Jahn98] O. Jahn, *Inbetriebnahme und Anwendung eines großen Natriumjodid-Photonendetektors,* diploma thesis, University of Mainz, 1998 (unpublished).

[Jeffries60] C.D. Jeffries, *Dynamic Orientation of Nuclei by Forbidden Transitions in Paramagnetic Resonance,* Phys. Rev. **117** 4 (1960).

[Kallmann50] H. Kallmann and M. Furst, *Fluorescence of Solutions Bombarded with High Energy Radiation (Energy Transport in Liquids),* Phys. Rev. **79** 5 (1950).

[Karliner60] I. Karliner, *Saturation of the Drell-Hearn-Gerasimov Sum Rule,* Phys. Rev. D **7** 9 (1960) 2717.

[Klempt02] C. Klempt, *Aufbau und Test eines BaF_2 Detektors*, diploma thesis, University of Mainz, 2002 (unpublished).

[Koch59] H.W. Koch and J.W. Motz, *Bremsstrahlung Cross-Section Formulas and Related Data*, Rev. Mod. Phys. **31** 4 (1959) 920.

[Lang96] M.E. Lang, *Einsatz des Datenerfassungssystems* ACQU *für den* DAPHNE*-Detektor,* diploma thesis, University of Mainz, 1996 (unpublished).

[Lang04] M.E. Lang, *Aufbau des* GDH*-Experiments und Messung der Helizitätsabhängigkeit von $\vec{\gamma}\vec{p} \rightarrow p\pi^+\pi^-$ von der Schwelle bis 800 MeV,* Ph.D. thesis, University of Mainz, 2004.

[Lannoy00] B. Lannoy, *Experimental verification of the Gerasimov-Drell-Hearn sum rule,* Ph.D. thesis, University of Gent, 2000.

[Leo87] W.R. Leo, *Techniques for Nuclear and Particle Physics Experiments* (1987, Springer-Verlag Berlin).

[Machleidt87] R. Machleidt, K. Holinde and Ch. Elster, *The bonn meson-exchange model for the nucleon-nucleon interaction,* Phys. Rep. **149** 1 (1987) 1.

[Matthews73] J.L. Matthews and R.O. Owens, *Accurate Formulae for the Calculation of High Energy Electron Bremsstrahlung Spectra,* Nucl. Instr. Meth. **3** (1973) 157–168.

[Matulewicz90] T. Matulewicz et al., *Response of BaF_2 Detectors to Photons of 3–5 MeV Energy,* Nucl. Instr. Meth. **A289** (1990) 194–204.

[Maurier] M. Maurier, engineering drawing no. 23.13.59.09.00, planche 2, *Commissariat a l'Energie Atomique,* 1986 and 1990.

[Murphy93] L. Murphy, *Double Pion Photon Production on Single Nucleons from Threshold up to 780 MeV,* Ph.D. thesis, DAPNIA/SPhN 93 49, 1993.

[Nafisi67] J. Nafisi-Movaghar, J.B. Birks and K. Razi Naqvi, *Energy Transfer in Organic Systems IV. Diffusion, solvent excitation migration and quenching in p-xylene solutions,* Proc. Phys. Soc. **91** 2 (1967) 449.

[Nicoll71] D.R. Nicoll and M.J.C. Ewer, *Organic Scintillators and Liquid Scintillation Counting.* (Horrocks and Peng, New York 1971).

[Olsen59] H. Olsen and L.C. Maximon, *Photon and Electron Polarization in High-Energy Bremsstrahlung and Pair Production with Screening,* Phys. Rev. **114** 3 (1959) 887–904.

[Pedroni88] P. Pedroni, *Simulation of the inelastic hadron collisions below 5 GeV: a modification of the* GEANT *3 package.* INFN/BE-88/3, 1988.

[Pedroni98] P. Pedroni, *Holes in φ and other geometrical corrections,* Internal Note, 1998.

[Powell71] R.C. Powell, *Energy Transfer in Poly(vinyl toluene),* J. Chem. Phys. **55** 4 (1971) 1871.

[Preobrazhensky01] I. Preobrazhensky, *Untersuchung der Helizitätsabhängigkeit der Einpionphotoproduktion am Proton,* Ph.D. thesis, University of Mainz, 2001.

[Rostomyan] T. Rostomyan, Ph.D. thesis, University of Gent, in preparation.

[Saito69] S. Saito, *Low-Energy Theorem for Compton Scattering,* Phys. Rev. **184** (1969) 1894.

[Sauer96] M. Sauer et al., *The ring shaped plastic scintillator detector STAR for forward angle reconstruction,* Nucl. Instr. Meth. **A378** (1996) 143.

[Schwamb99] M. Schwamb, *Retardierungseffekte in der Deuteronphotospaltung im Bereich der Deltaresonanz,* Ph.D. thesis, University of Mainz, 1999.

[Schwamb01] M. Schwamb, H. Arenhövel,

a) *Off-shell effects in electromagnetic reactions on the deuteron,* Nucl. Phys. **A696** (2001) 556–580;

b) *The role of meson retardation in the NN interaction above pion threshold,* Nucl. Phys. **A690** (2001) 647;

c) *The role of meson retardation in deuteron photodisintegration above pion threshold,* Nucl. Phys. **A690** (2001) 682.

[Schwamb03] M. Schwamb, private communication, 2003.

[Smith75] T. Smith, *How Much Light from Rectangular Scintillation Counters?,* Phys. Med. Biol. **20** 2 (1975) 282.

[Wartenberg97] S. Wartenberg, *Die Strahlasymmetrie in der Deuteron-Photospaltung im Bereich von 160 bis 410 MeV,* Ph.D. thesis, University of Mainz, 1997.

[Weller04] H.R. Weller, *Future Plans for Measuring the GDH Integrand on the Deuteron at HIγS,* GDH2004: Proceedings of the Third International Symposium on the Gerasimov-Drell-Hearn Sum Rule and its Extensions, World Scientific Publishing Company, 2005.

[Windisch02] B. Windisch, *Inbetriebnahme und Test des* DAPHNE*-Detektors*, diploma thesis, University of Mainz, 2002 (unpublished).